

Helicopter Dynamics Concerning Retreating Blade Stall on a Coaxial Helicopter

A project presented to
The Faculty of the Department of Aerospace Engineering
San José State University

In partial fulfillment of the requirements for the degree
Master of Science in Aerospace Engineering

by

Aaron Ford

May 2019

approved by

Prof. Jeanine Hunter
Faculty Advisor



© 2019

Aaron Ford

ALL RIGHTS RESERVED

ABSTRACT

Helicopter Dynamics Concerning Retreating Blade Stall on a Coaxial Helicopter

by Aaron Ford

A model of helicopter blade flapping dynamics is created to determine the occurrence of retreating blade stall on a coaxial helicopter with pusher-propeller in straight and level flight. Equations of motion are developed, and blade element theory is utilized to evaluate the appropriate aerodynamics. Modelling of the blade flapping behavior is verified against benchmark data and then used to determine the angle of attack distribution about the rotor disk for standard helicopter configurations utilizing both hinged and hingeless rotor blades. Modelling of the coaxial configuration with the pusher-prop in straight and level flight is then considered. An approach was taken that minimizes the angle of attack and generation of lift on the advancing side while minimizing them on the retreating side of the rotor disk. The resulting asymmetric lift distribution is compensated for by using both counter-rotating rotor disks to maximize lift on their respective advancing sides and reduce drag on their respective retreating sides. The result is an elimination of retreating blade stall in the coaxial and pusher-propeller configuration. Finally, an assessment of the lift capability of the configuration at both sea level and at “high and hot” conditions were made.

ACKNOWLEDGMENTS

I would like to thank Professor Hunter for her willingness to advise me through the course of this project and for pointing me in the right direction when I required it. She is an inspiration to all of her students and has instilled in me a love for dynamics and engineering that few others have achieved. She is a cornerstone of San Jose State's Aerospace Engineering department and treats all of her students with openness and fairness. She has always been there for me academically and personally, and she continues to demonstrate a character and love for her students that serves as a model for all instructors at San Jose State.

Nomenclature

a	= blade section two-dimensional lift-curve slope
a_r	= blade section two-dimensional lift-curve slope at section r
b	= number of blades
c	= chord
c_r	= chord at blade section r
e	= hinge offset percentage
m	= mass (kg)
r	= blade radius
\bar{r}	= non-dimensional blade radius
t	= time (sec)
v_r	= induced velocity
z	= distance in z direction (m)
\ddot{z}	= acceleration in the z direction
D	= drag (N)
D_{pr_r}	= profile drag at station r
F_z	= force in the z direction
I_b	= moment of inertia of blade
L	= lift (N)
L_r	= lift at blade section, r
M_F	= blade moment
P_{pr_r}	= profile power at station r
Q	= torque (N-m)
R	= length of blade
T	= thrust (N)
U	= velocity (m/s)
U_p	= perpendicular velocity component
U_T	= tangential velocity component
V_∞	= freestream velocity
V_c	= climb velocity
V_T	= blade tip velocity
α	= angle of attack
α_{ds}	= critical angle of attack for dynamic stall
α_{ss}	= critical angle of attack for static stall
β	= flap angle
$\dot{\beta}$	= flap velocity
$\ddot{\beta}$	= flap acceleration
β_0	= cone angle
β_{1s}	= flap angle in lateral plane
β_{1c}	= flap angle in longitudinal plane
γ	= Lock number
θ	= blade incidence
θ_r	= blade incidence at section r
θ	= blade incidence

θ_0	= collective input
θ_{1s}	= lateral cyclic input
θ_{1c}	= longitudinal cyclic input
λ	= rotor inflow ratio
μ	= non-dimensional velocity
ν	= flapping frequency
ρ	= air density
ϕ	= inflow angle
ϕ_r	= inflow angle at section, r
ψ	= blade rotation angle
Ω	= rotational velocity
C_L	= coefficient of lift
C_d	= coefficient of drag
C_{d_r}	= coefficient of drag at section, r

Table of Contents

Chapter 1 - Introduction	1
1.1 Motivation	1
1.2 Literature Review	2
1.2.1 Flap Motion of Helicopter Rotors with Novel Dynamic Stall Model	2
1.2.2 Modelling the Aerodynamics of Coaxial Helicopters - from an Isolated Rotor to a Complete Aircraft	3
1.2.3 Helicopter Blade Flapping With and Without Small Angle Assumption in the Presence of Dynamic Stall	3
1.2.4 The Effects of Rotor Blade-Tip Geometry on Helicopter Trim and Control Response	4
1.2.5 Control of Dynamic Stall of Helicopter Rotor Blades	4
1.2.6 A Study of Coaxial Rotor Performance and Flow Field Characteristics	5
1.2.7 Spanwise Differences in Static and Dynamic Stall on a Pitching Rotor	5
1.2.8 Boundary-layer Transition Measurements on Hovering Helicopter Rotors by Infrared Thermography	6
1.2.9 Performance Analysis of a Coaxial Helicopter in Hover and Forward Flight	6
1.2.10 Performance and Vibration Analyses of Lift-Offset Helicopters	6
1.2.11 Design of a Rotor Blade Tip for the Investigation of Dynamic Stall in the Transonic Wind-tunnel Gottingen	7
1.2.12 Unsteady Aerodynamic Analysis and Wake Simulation of Helicopter Rotors using the Time-Domain Panel Method	7
1.2.13 Helicopter Theory	8
1.2.14 Helicopter Flight Dynamics	8
1.3 Project Proposal	8
1.4 Methodology	8
Chapter 2 - Introduction to Helicopter Aerodynamics	9
2.0 Blade Element Theory Introduction	9
2.1 Swashplate	12
2.2 Blade Flapping	12
2.3 Retreating Blade Stall	14
2.4 Structuring a Model	15
Chapter 3 - Blade Element Theory	16

3.1 The Hover Flight Regime	16
3.1.1 Induced Velocity and AOA of blade	17
3.1.2 Lift and Drag of the Element	19
3.1.3 Torque	20
3.1.4 Thrust	21
3.1.5 Power	22
3.2 Interpreting the results	23
3.3 Next Steps	23
Chapter 4 - Rotor Disk Dynamics	24
4.1 Establishing a model	25
4.2 Rotor System Types	25
4.2.1 Rigid Rotor Systems	26
4.2.2 Articulated Rotor System	27
4.2.3 Teetering Rotor System	28
4.3 Static Versus Dynamic Stall	29
Chapter 5 - Blade Flapping	31
5.0 Rotor Disks are not Gyroscopes	31
5.1 Lead-Lag	37
5.2 Modelling the flapping	38
5.3 Results of flapping motion	42
5.4 Benchmarks	43
Chapter 6 Flapping Analysis	45
6.0 Flapping Analysis of the flapping hinge	45
6.0.1 Flapping Analysis of Hinged Rotor Blade	48
6.0.2 Flapping Analysis of Hingeless Blade	48
6.1 Hinged Rotor Flapping Analysis	49
6.2 Flapping Analysis of Hingeless Blade	54
6.2.1 Comparison Against the Benchmark Case	54
6.2.2 Analysis of Hingeless Flapping in Various Conditions	55
6.3 Conclusion	58
Chapter 7 Evaluating Alternate Conditions	59

7.0 Taking Advantage of Having a Coaxial Rotor	59
7.1 Dynamic Response From Straight and Level to Nose Forward	61
Chapter 8 Evaluating The Coaxial-Pusher Configuration	64
8.0 Taking Advantage of Having a Coaxial Rotor	64
8.1 Analysis	68
Chapter 9 Evaluating Lift	70
9.0 Analyzing the lift through rotation	70
9.1 Evaluating the lift distribution about the rotation along the span	74
9.2 Evaluating the lift distribution while hot and high	76
Chapter 10 Conclusion and Future Work	77
10.0 Conclusion	77
10.1 Future Work	78
References:	79
Appendix A - Blade Element Theory Matlab Program	82
Appendix B - Hinged Flapping Matlab Program	85
Appendix C - Hingeless Blade Flapping MatLab Program	90
Appendix D - Hingeless AOA Distribution Matlab Program	94
Appendix E - Hingeless Lift Distribution Matlab Program	98

Chapter 1 - Introduction

1.1 Motivation

The problem to be examined is the occurrence of retreating blade stall on a coaxial helicopter. Retreating blade stall is a phenomenon that occurs as a result for excessive forward velocity and is one of the major contributing restrictions to the forward velocity achievable on a rotary wing aircraft such as a helicopter.

The aerodynamic problem of helicopter flight is the dissymmetry of lift that occurs because one half of the rotor disk is advancing in the direction of of the aircraft's velocity vector, and the other half of the rotor disk is advancing. It can easily be seen that the advancing side has a higher velocity, and thus generates greater lift, than that of the retreating side resulting in the aforementioned lift dissymmetry.

Dissymmetry of lift is largely compensated for through a mechanical means referred to as “blade feathering”. In short, it allows the individual blade to change its angle of attack (AOA) as it rotates about the rotor hub. A typical design feathers the blades so that there is a minimal increase of AOA on the advancing side while increasing the AOA on the retreating side to generate more lift and balance out the lift across the rotor disk.

A secondary effect of lift generation across the rotor disk is the occurrence of blade “flapping”, which is a literal flapping of the blades to help further increase or decrease lift required across the rotor disk in order to balance out the lift distribution. Blade flapping is naturally occurring and is a result of the elastic nature of the rotor blades.

Problems arise when the forward velocity of the aircraft exceeds the ability of the rotor blades to compensate for dissymmetry. The retreating blade of the rotor disk will eventually experience an angle of attack that exceeds the attached flow angle of the airfoil, causing separation and stall. This occurrence is a direct result of the forward air speed, the AOA of the retreating blade, and the severity of the blade flapping, which exacerbates the critical AOA. Initial retreating blade stall symptoms include vibration, nose-up pitching, and a rolling tendency toward the side opposite the advancing side. If the problem is not dealt with as the symptoms appear, the result can be a catastrophic loss of controlled flight.

Retreating blade stall can be delayed or lessened in case of coaxial helicopter configurations. Unlike conventional helicopters that possess a main rotor for lift and thrust with a tail rotor for anti-torque, a coaxial helicopter utilizes two counter-rotating rotor disks that serve to provide lift, thrust, and torque neutralization. This configuration is not immune to the retreating blade stall, however. It merely delays its onset. The question is: what is the dynamic response of coaxial helicopter experiencing retreating blade stall? Is it as catastrophic as a conventional helicopter?

To answer such questions, an analysis of rotor blade aerodynamics, blade flapping dynamics, and overall aircraft dynamic responses must be conducted. This examination is particularly interesting because of the direction that rotary wing design is taking. The next generation of helicopter being developed for the U.S. military is the S-79 Raider, designed and built by Sikorsky. The S-79 is a coaxial helicopter with a pusher propeller, which allows it to operate in all the flight regimes normally expected out of a helicopter while giving it the added capability of straight and level flight and pusher prop-only thrust. Flight testing is currently on going, however, the maximum velocity achievable by the S-79 is approximately 250 MPH. To put that into perspective, the fastest non-experimental helicopter in the world, the Boeing CH-47, can only achieve a maximum speed of 196 MPH.

It is clear that the coaxial/pusher configuration is an innovative design that will propel helicopter design into the future. However, with so few such aircraft in existence, there is great importance in examining the physical response of retreating blade stall, creating plausible models to analyse, and fully understanding the dynamic responses associated with pushing such an aircraft to the edge of its performance capabilities.

1.2 Literature Review

1.2.1 Flap Motion of Helicopter Rotors with Novel Dynamic Stall Model

One of the facets regarding retreating blade stall is the influence of rotor blade flap motion. Wei Han, Jie Lie, Chun Liu, Lei Chen, Xichao Su, and Peng Zhao explore blade flapping in their research article entitled “Flap motion of helicopter rotors with novel, dynamic stall model.” The primary focus of the research was to provide a mathematical equation that accurately reflects and approximates the movement of blade flapping. Researchers before them have approached the same problem utilizing linear approximation methods, based primarily on the assumptions of small inflow and flapping angles. These assumptions are convenient in the engineering application, however, they are limited to only the small angle assumptions and do not adequately address large angles. The task taken on by the researchers was to analyze the aerodynamics of the blade element, then establish a non-linear equation that could be generally applied to both small and large angles. To effectively do this, the coefficient of lift must be calculated in a way that accounts for the dynamic stall of a helicopter blade. Dynamic stall conditions make calculating the load of a helicopter blade extremely difficult, and it is a task that is normally overcome with the use of vortex theory and the Navier-Stokes equations. These equations, however, are complex and require time to properly model and simulate. To overcome this, the Snel stall model was used to provide a method that was relatively simple and yet did not compromise the accuracy of the analysis. The efforts of this research resulted in a validation of the Snel stall model and provided an successful analysis of flap response for rotor blades at

varying angles of attack and conditions. The result is a model that provides accurate and effective results for determining flap motion of helicopter rotors[1].

1.2.2 Modelling the Aerodynamics of Coaxial Helicopters - from an Isolated Rotor to a Complete Aircraft

The purpose of this paper by Hyo Won Kim and Richard E. Brown was to demonstrate a level of computational modelling that accurately captures the aerodynamic flow field associated with coaxial rotor systems. The method utilized in this analysis involve the vorticity-velocity form of the Navier-Stokes equation which allows vorticity to be conserved. Fuselage aerodynamics was modelled using a vortex panel method while fuselage lift generation was modelled using the Kutta condition along the surface. Numerical differentiation of a pre-specified non-linear Lagrangian helped to derive equations of motion for the blades as driven by aerodynamic loading along their span. Farassat-1A formulations of the Ffowcs Williams-Hawkings equations were used to account for acoustics as it was applicable. The analysis compared the aerodynamics of a hinged coaxial rotor system to the aerodynamics of a stiffened hingeless coaxial rotor. Finally a coaxial helicopter with a pusher-propeller for thrust was also examined and compared with the aforementioned configurations. The conclusion of the comparisons demonstrated that there was no real appreciable difference in the localized interactions of the blades and and the wakes that are produced by conventional and coaxial configurations. The study suggests that state of the art computational fluid dynamics are more that adequate in providing advanced simulation details across a wide array of models and configurations[2].

1.2.3 Helicopter Blade Flapping With and Without Small Angle Assumption in the Presence of Dynamic Stall

In their paper Helicopter Blade Flapping With and Without Small Angle Assumption in the Presence of Dynamic Stall, Jyoti Ranjan Majhi and Ranjan Ganguli develop an equation for non-linear aerodynamics pertaining to blade stall. Typically, flapping motion is simplified by making the assumptions that the flap angle is small, the induced angle is also small, and that the aerodynamics manifest themselves in a linear way. Dynamic stall, however, makes the linear results come into question. By utilizing a semi-empirical dynamic stall aerodynamics model, Majhi and Ganguli are able to derive a general equation that describes helicopter blade flapping. In order to solve the steady state conditions and validate the small angle approximation, numerical solutions were performed. The result of the study demonstrate that while small flapping and induced angle approximations are acceptable in the realm of linear aerodynamics, these assumptions yield inaccuracies when applied to nonlinear aerodynamics[3].

1.2.4 The Effects of Rotor Blade-Tip Geometry on Helicopter Trim and Control Response

Kumar and Vekatesan explore the effect the geometry of a helicopter rotor-blade tip has on the trim and control response. Advanced geometry tips, which include the anhedral tip as well as tip sweep, are designed to reduce noise and increase performance. However, while there are positive attributes to the advanced geometric tips, the higher cost is demonstrated to be in the added weight and the complex structural design. The study involved a comprehensive study of helicopter aeroelastics and rotor-fuselage coupling. It also conducted a comparative analysis of straight tip, swept tip, and tip anhedral rotor blades. The helicopter that is being modelled in this analysis is a conventional single tail and single rotor with hingeless rotors. Tip pretwist, precone, predrift, tip sweep, torque offset, and root offset are included in the model and the blade experiences flap, torsion, lag, and axial deformations. In order to model dynamic wake and dynamic stall as they pertain to airload calculations, the Peters-He dynamic wake theory and the ONERA dynamic stall theory were both utilized. The non-equilibrium equations for six degrees of freedom were solved for any general flight condition. Integrating the full set of nonlinear equations of motion determines the pilot response to pilot control inputs. The results of the study demonstrated that blades with tip dihedral/anhedral and tip sweep saw the 1 per revolution harmonics of the root reduce in load. However, the 4 per revolution harmonics of the hub increased in magnitude. Finally, rotor tip dihedral resulted in a yaw rate reversal for cyclic inputs in both the lateral and longitudinal directions[4].

1.2.5 Control of Dynamic Stall of Helicopter Rotor Blades

In the study, Control of dynamic stall of helicopter rotor blades, Rong and PinQi investigate the viability of trailing edge flaps on rotor blades in order to delay the onset of retreating blade stall. In order to calculate the aerodynamic loads of a blade section, the Leishman-Beddoes unsteady two-dimensional dynamic stall model was utilized. The trailing edge flap section loads were calculated using the Harihara-Leishman unsteady two-dimensional subsonic model. The aerolastic responses of the rotor system in high-speed and high-loading in forward flight are solved by adopting the Galerkin method and the aeroelastic analytical method while combined with numerical integration. The results of the analysis demonstrate that the flaps are effective in delaying retreating blade stall. This is achieved by the subsequent redistribution of load to an improved state and the increase of efficiency of rotor and blades. An area the study did not investigate was the increase requirement of structural support in order for flaps to be utilized in such a high speed and oscillatory regime[5].

1.2.6 A Study of Coaxial Rotor Performance and Flow Field Characteristics

Barbely, Komerath, and Novak established a study in the flow field and aerodynamics of a coaxial rotor system as a precursor to studying the acoustics of the associated system as well as to better understand the interaction between the two rotors. An unsteady Navier-Stokes solver, known as RotUNS, was utilized to predict the hover and forward flight performances of a coaxial rotor system. RotUNS uses a simplified blade aerodynamics model. However, RotUNS demonstrated an improved performance in hover calculations when compared to element momentum theory. The study first simulated a simplified model involving two airfoils traveling in opposite directions with a coaxial equivalent separation in order to better understand the results of a more complex simulation. Next, a three-dimensional coaxial flow field was examined. The pressure fields in all sections of the coaxial system were observed for various azimuth position in the rotor cycle. The work was compared with and validated against experimental data and helped to lay the footwork for understanding the acoustics associated with the coaxial rotor system[6].

1.2.7 Spanwise Differences in Static and Dynamic Stall on a Pitching Rotor

Merz, Wolf, Richter, Kaufmann, Mielke, and Raffel investigate the spanwise differences in static and dynamic stall for a pitching rotor. The investigation was conducted on a rotor blade tip model at a Reynolds number of 900,000 and Mach 0.16. It should be noted that the chosen Mach number is quite low with respect to typical full scale helicopter designs, which results in isolating the stall to being induced purely by angle of attack. Another important feature of note is that the blades possessed an aspect ratio of 6.2. By using a high-speed particle image velocimetry and unsteady surface pressure measurements, the behavior of the flow separation was observed and analyzed. The geometric shape of the rotor blade, which featured increasing twist from root to tip, allowed for a shifting of the effective angle of attack roughly two thirds of the span outboard on the blade. Flow separation was identified for static angles of attack. When observing dynamic stall conditions, it was found that leading edge vortex formations started at or near the location, along the span, where there was seen to be static stall onset. Tip vortex was seen to have influence in two distinct ways. The first was that lift was reduced and pressure drag was increased. This is a predictable outcome as shown from inviscid theory. These conditions hold as long as the flow is attached. The second way the tip vortex shows influence is during the dynamic stall regime. What occurs is an increase in lift which results in a streamwise vorticity and thus a pinning of the dynamic stall vortex. Ultimately, the aerodynamic loads of the outboard section are smaller than the inboard sections, or those outside of the dynamic stall regions[7].

1.2.8 Boundary-layer Transition Measurements on Hovering Helicopter Rotors by Infrared Thermography

Richter and Shulein explore the boundary-layer transition on the upper side of helicopter rotor blades by utilizing high-speed infrared thermography. A single image of the blade, as produced by the infrared equipment allows for the detection of the transition region in both its onset and ending positions. Measurements were taken on a Mach-scaled BO105 for varying rotation frequencies and compared with numerical solutions. Additional measurements were taken on full scale BO105 and EC135 helicopters. It was found that the transition point shifted upstream as the rotor rotation frequency was increased. However, in the various cases that were studied, the transition region remained nearly constant. In the case of the EC135, specifically, it was found that the transition position moved up stream in the radial direction, but is nearly constant up through roughly eighty percent of the radial. However, as was with the BO105, the transition location is shifted further upstream with the increase in rotational frequency[8].

1.2.9 Performance Analysis of a Coaxial Helicopter in Hover and Forward Flight

In the paper “Performance Analysis of a Coaxial Helicopter in Hover and Forward Flight”, Fernandes presents a comparison between conventional and coaxial rotor systems for helicopter flight. In order to better understand the complex aerodynamic interactions associated with helicopter flight, the free-vortex methodology (FVM), which is a Lagrangian-based wake convection methodology, is utilized in order to produce solutions for the wake produced by the rotor blades. It is known, and was confirmed in the analysis, that the wake interaction between the two rotors was highly dependant on the spacing of the two rotor systems. This dependance on spacing provides a variable in which to employ a parametric study on the effect of that distance and how the wake interaction changes as the spacing changes. During the comparison phase, an equivalent single rotor system was compared to its coaxial counterpart. The results demonstrate the while the conventional system demonstrated better performance response in forward flight, the coaxial was superior in hover conditions. It was also found that higher power requirements were needed with a lower inter-rotor spacing. It was expected that the upper rotor would be influenced by the lower rotor in low advance ratio conditions as well as hover. A response that was not anticipated was that the upper rotor was affected with a higher advanced ratio as well[9].

1.2.10 Performance and Vibration Analyses of Lift-Offset Helicopters

Go, Kim, and Park establish a study to validate the analyses of lift-offset compound helicopters in the areas of performance and vibration. The aircraft of focus is the Sikorsky XH-59A, which was a precursor to the S-69 coaxial helicopter with a pusher propeller. To perform the analyses

for the performance, vibration, and loads, the Comprehensive Analytical Method of Rotorcraft Aerodynamics and Dynamics II (CAMRAD II) analysis code was utilized. In order to complete the analysis, a general free wake model was also used. The SH-59A was analyzed in various flight conditions in both standard helicopter utilization and while using an auxiliary propulsion system, such a pusher propeller. The vibrational response in forward flight was also examined. The results of the analysis demonstrated a close agreement with flight test data and with previous analyses proving that the techniques used are reliable and appropriately established[10].

1.2.11 Design of a Rotor Blade Tip for the Investigation of Dynamic Stall in the Transonic Wind-tunnel Gottingen

Lutke, Huhn, Govers, and Schmidt present the aerodynamic and structural design of a double-spect planform pitching blade-tip. The successful utilization of high-fidelity finite element (FE) and computational fluid dynamic (CFD) simulations were used to aid in the design process. A three-dimensional FE model was used to analyse the stress distributions, deformations, as well as eigenfrequencies. CFD was used to simulate a light dynamic stall case by employing Unsteady Reynolds-Averaged Navier-Stokes (RANS) equations. When compared to experimental data, the results of the CFD demonstrated good agreement only during attached flow. Once separation occurs, experimental and numerical data start to diverge. Regarding the structural analysis, under the same conditions, it was found that a factor of safety of 2.0 was sufficient[11].

1.2.12 Unsteady Aerodynamic Analysis and Wake Simulation of Helicopter Rotors using the Time-Domain Panel Method

Lee, L. Cho, and J. Cho present their study of helicopter rotor aerodynamics. Specifically, unsteady aerodynamics. Based on potential flow theory, an unsteady panel method was utilized for the analysis. The solution for the panel method involves doublet singularities and a piecewise constant source. This panel method is a combination of the Dirichelt Boundary condition and a time-stepping method. The unsteady behavior of helicopter rotors are simulated by using a time-stepping loop. In order to simulate the wake associated with the helicopter rotor, a free wake model was used. The study used the panel methods with an assumption of incompressible flow and found that the results were comparable to the experimental data for both forward flight and hovering conditions. The study validates the use of the time-domain panel method for practical applications such as rotor system configuration analysis and aerodynamic design[12].

1.2.13 Helicopter Theory

Helicopter Theory by Wayne Johnson is a comprehensive look at helicopter theory that can be used as a reference to anyone wishing to be involved in helicopter design. The textbook examines all facets of helicopter design, examining areas such as vertical flight, forward flight, design features, performance requirements, rotary wing dynamics, rotary wing aerodynamics, noise considerations and design, stability and control, and stall characteristics. The text will be used as a cornerstone to this analysis and will provide a high degree of completeness in an analysis of this nature[13].

1.2.14 Helicopter Flight Dynamics

Helicopter Flight Dynamics by Dr. Gareth D. Padfield is a text that covers the theory and application of flying qualities and simulation modelling for helicopters, and is the AIAA textbook of choice for covering helicopter flight dynamics. The scope of the text covers the dynamic responses of helicopter flight in all flight regimes that is involved in helicopter flight. It is a thorough and comprehensive look at flight dynamic modelling for rotary wing aircraft[14].

1.3 Project Proposal

The purpose of this project is to develop a model that can be used to approximate the dynamic response of a coaxial helicopter after the induction of retreating blade stall has occurred. The configuration and mechanics of a coaxial helicopter has been explored to a far lesser degree than its conventional counterpart. As a result, the focus of this project will center around the dynamic responses of a coaxial helicopter, specifically, in both the conventional flight regime as well as a pusher propeller configuration. The project will require an analytical development of the equations of motion of the airframe, as well as an analysis of individual responses such as blade flapping.

1.4 Methodology

The method used to study this presented problem will use an approach that analyses the individual components to be added together in order to determine the final response.

The first step will be modeling the motion of the blade flapping. Blade flapping occurs as a function of the asymmetric loading of rotor disk throughout the rotation during forward flight. The flapping will have an influence on the forces that the rotor shaft experience, which directly affect the fuselage and the dynamic response of the aircraft.

Next, an aerodynamic model of the rotor blades will need to be established. This will prove a complex area due to the fact that the rotor disk experiences a different velocity on each spanwise section, interacts to a degree with its own wake, and experiences various flow conditions, such as reverse flow and stall on different section of the rotor disk.

Finally, the effects of the flapping and the aerodynamics of the disk will provide the moments and forces that are induced upon the rotor shaft. These forces and moments that the shaft experiences will directly influence the behavior of the fuselage and, subsequently, the entire body of the airframe. It is the intent of this project to model the dynamic responses as a result of these forces and moments and offer a prediction to aircraft behavior as a result.

This analysis will primarily be quantitative in nature and will rely heavily on helicopter theory that has been outlined and, in many cases, approximated using physical theories or models that can offer accurate representations of real world responses provided appropriate assumptions.

Chapter 2 - Introduction to Helicopter Aerodynamics

2.0 Blade Element Theory Introduction

The need for a quantitative method to determine the lift forces over a rotor disk brings rise to the need for Blade Element Theory. This method of solving lift distributions with this method are not terribly dissimilar to that of solving two-dimensional airflow theory. However, as the name implies, the computed solution only applies for a specific element of the rotor blade. There many aspects to the aerodynamics of rotary-wing aircraft that differ greatly from their fixed wing counterparts. As is commonly known in the aerospace community, there are theories for determining aerodynamic forces of a fixed wing that can be solved with relative ease due to the fixed nature of wings on a standard airplane. Given the airfoil shape and a specific flight condition, the lift characteristics are easily found. Nothing changes with respect to time. However, this is not the case in rotary-wing flight. Let us first examine the airflow differences of fixed versus rotary wings. For a given flight condition, fixed wings experience the same freestream velocity and lift on all sections of the wing. This, of course, implies no aerodynamic or geometric twist and is somewhat simplified, however, the point is easily seen. The helicopter, however, has a rotary wing. Due to the rotational nature of this wing, the freestream velocity experienced by this wing varies along its span. This adds several layers of complexity to the determination of the lift distribution along a rotor blade and is the reason why blade element theory is necessary. The procedure for this theory involves solving for a small element, the smaller the better, at a specific location along the span and then adding all of the elements together to get the total lift distribution.

There are two distinct flight regimes within rotary-wing flight that must be examined separately. Those include flight in hover and forward flight. For the reader that is unfamiliar with helicopter flight, hover is the flight condition where the rotary-wing generates lift vertically and suspends the aircraft in question in the air at a pilot commanded altitude without inducing translational flight. It is this flight condition that gives the helicopter a strong advantage over fixed wing aircraft in the accomplishment of certain missions. Forward flight, like its fixed wing counterpart, is simply translational movement. In discussing this analysis, forward flight will be used to refer to, literally, translation flight toward the front of the vehicle. However, in reality, due to the unique nature of helicopter design, the so-called forward flight condition might also simply refer to translational flight in general as much of the rotor blade aerodynamics remain the same regardless of translational direction. That distinction must be defined by the speaker or writer in his or her analysis.

In the discussion of hover versus forward flight, the hover condition is easily the more simple of the two. Assuming a zero-crosswind condition, the only freestream velocity that the rotor blade experiences is that which it creates through its rotational movement. In essence,

$$V = \omega r \quad (2.1)$$

Where V is the freestream velocity at location r along the span of the blade. By common convention, ω represents the angular velocity of the rotor system about the hub. Figure 2.1 provides a visualization of the velocity profile about the rotor disk in hover flight.

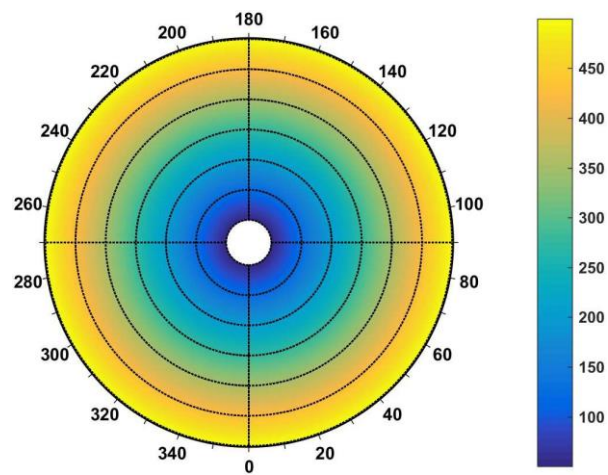


Figure 2.1- Generic velocity profile of rotor disk in hover.

Figure 2.1 does not represent a specific aircraft. Variables were chosen to ensure that the differences in the velocity about the disk were obvious to the reader.

The visualization provided reinforces the thought that computing the force distribution along a disk is as simple as determining the solutions for a single blade and applying it to all blades. However, it is prudent to remind the reader that this is a gross simplification of the analysis. Recall that the lifter surfaces of the helicopter rotate. In order to truly capture the effects of the lift distribution, these forces will need to be examined with respect to time as the rotor system rotates about the hub of the helicopter. This will be explored in more detail in subsequent sections of this study.

The complexity of the analysis grows with severity as forward flight is introduced to the examination. Intuitively, one can conclude that as the helicopter translate in a given direction, the advancing side of the rotor system will experience a freestream velocity than the retreating side. This phenomenon is determined by the following:

$$V = V_{\infty} + \omega r \sin(\alpha) \quad (2.2)$$

Where V_{∞} is the freestream velocity of the aircraft and α is the angle of the blade about the hub.

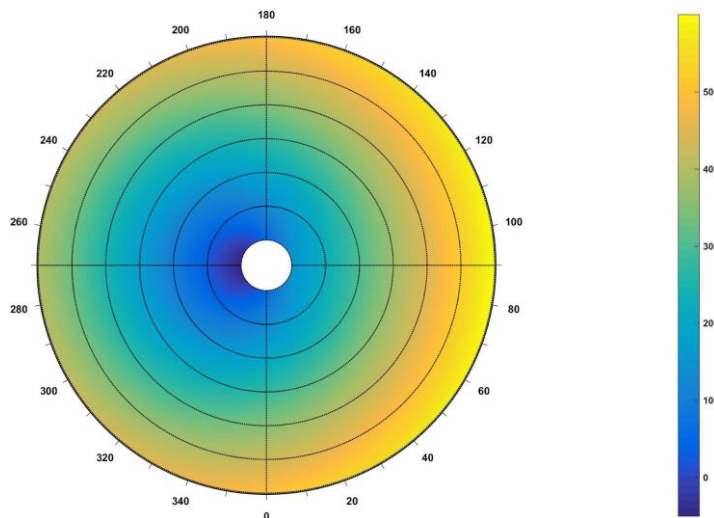


Figure 2.2 - The velocity profile the rotor disk in forward flight.

Figure 2.2 provides a visualization for how the velocity profile varies about the disk in a forward flight condition. The coordinate system of the rotor, by convention, is that 0 degrees represents the direction toward the aft of the helicopter, while 180 degrees is the front. U.S. made helicopters utilize a counter-clockwise rotation, when viewed from above, and thus angles 0-180 degrees represent the advancing side of the disk, while 180-360 represent the retreating side of the disk. Again, the velocity profile and initial conditions do not represent a specific airframe, but rather were chosen to best exemplify the phenomenon being demonstrated here.

Close inspection of the figure shows that velocities on the advancing side of the disk experience a greater velocity than that of the retreating side. This is not unexpected. However, the section of

the retreating side between 260 and 280 degrees adjacent to the hub reveals something that might defy intuition. It shows that there is reverse flow on the disk. That is, when the rotary wing is in a forward flight condition, this section does not travel fast enough in its rotation to overcome the forward speed and has air that travels in the reverse direction relative to that blade.

Clearly, this occurrence of adverse velocity profiles across the disk will result in a net force that creates a moment and a left rolling tendency of the helicopter. Uncorrected, this is an uncontrollable flight regime. This is compensated for by utilizing a swashplate, which helps to correct the problem as well as provides the means for translational movement.

2.1 Swashplate

The swashplate of a helicopter, for all its complexities, is a simple and elegant solution to the problem of inducing translational lift and helping to equalize the lift distribution from side to side. The swashplate is made up of two parts. The first part, or the lower section, has the ability to tilt in any direction that the control inputs dictate. It can shift up and down and/or tilt, but does not spin. The second part, or the upper section rests on top of the lower piece so that it shifts and tilts with the lower piece. It is attached to each of the rotor blades and rotates with the rotor system so that so that the pitching angle of the swashplate can control the individual pitch of the blade as it rotates about the rotor hub and shaft. It is in this way that the pitch is held constant for a specific section of the disk.

If the control input for the pitching of the swashplate, referred to as the cyclic, is pressed forward so that the aircraft will nose down and pitch forward, then the swashplate will also tilt forward. In a hover position, this will increase the angle of attack, and thus the lift, of the retreating side of the rotor disk and create a moment. Due to gyroscopic precession, the moment, which is induced at 270 degrees, will take effect at 0 degrees, causing the helicopter to pitch forward. The orientation of the swashplate will also maintain that the angle of attack retreating side is increased and the advancing side is decreased to help generate similar levels of lift. This is only part of the story, however, and the rest of the compensation will take place through a phenomenon known as blade flapping.

2.2 Blade Flapping

Blade flapping is, literally, the up and down flapping of the rotor blades as they rotate about the rotor hub while in forward flight. It is a direct response to having an uneven lift distribution and does not occur in the state of hover.

As the blades rotate from 0 degrees to 180, they experience the greatest amount of lift for an otherwise unaltered system. Rotor blades, whether through hinges or pure elasticity, respond to

this increase of lift with a moment along the entire span of the blade resulting in an upward flapping velocity. As shown in figure 2.3, the velocity of the flapping (v_f), plus the induced velocity (v_i) resolve into velocity direction that ultimately reduces the angle of attack (AOA). This decrease in AOA results in a reduced lift.

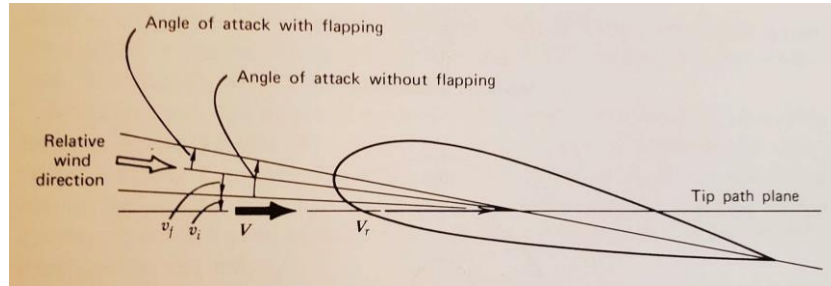


Figure 2.3 - Decreased angle of attack due to up flap [15]

Conversely, on the retreating side, the blade experiences less lift resulting in a downward flapping and thus a downward velocity. Figure 2.4 shows that this downward flapping produces a resolved velocity vector that increases the angle of attack and increases lift on the retreating side.

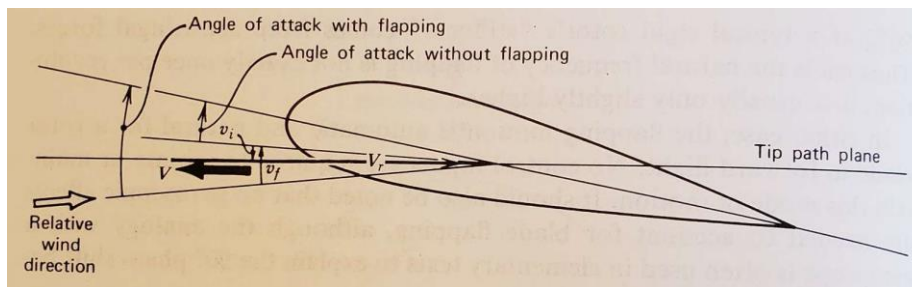


Figure 2.4 - Increase angle of attack on retreating side due to down flap [15]

It is through the means of flapping that the rotor system is able to compensate for the uneven lift distribution. The blades will flap up and down in a periodic fashion as they rotate about the rotor shaft so that they are flapping constantly on an individual basis. Because the flapping occurs in the same way in the same place about the disk for a given flight condition, the place that the blade occupies as it makes up the so called rotor disk remains the same. As previously discussed, the cycle is of up and down travel of each blade occurs once per revolution and can be modelled as simple harmonic motion. In order to create an aerodynamic model with the highest possible accuracy, blade flapping will need to be considered and taken into account.

2.3 Retreating Blade Stall

The focus of this study revolves around the occurrence of retreating blade stall. As the name implies, this occurs when the blade rotating through the retreating side of the rotor disk stalls and no longer produces enough lift to maintain controlled flight. Retreating blade stall, if not corrected soon enough, results in catastrophic dynamic responses. It is universally accepted that pilots should avoid conditions that will result in retreating blade stall. In previous sections, it was seen that the velocity profile across the disk in forward flight varies due to the rotational nature of the rotor blades. The swashplate and blade flapping was also discussed. The profound effect that the swashplate and the flapping have on stable flight together must not be overlooked. The swashplate provides much of the pitch adjustment for effecting the AOA as the blades rotate, while blade flapping finishes the job. As the pilot provides a greater input, it results in a greater swashplate pitching angle. This increase in pitching will result in a greater AOA potential, and greater lift generation, and a greater degree of flapping. All of this in conjunction provides the lift that is required for flight on a helicopter. There are, however, limitations. Because lift is a function of the square of the velocity, increasing the forward velocity on the aircraft will cause an increase in lift on the advancing side. This will also decrease the lift on the retreating side. As shown in figure 2.4, the decreasing lift results in a downward flapping which increases the angle of attack. It is commonly understood amongst aerodynamicists that airfoils have a maximum angle of attack that can be achieved before stalling regardless of the freestream velocity. It should be fairly apparent by now that if the forward velocity of the helicopter is high enough, then the pitching of the swashplate and the increased angle of attack due to blade flapping will increase past the point of stall. Recall the fact that the velocity changes, or increases as a function of radial distance from the hub. With that in mind, it stands to reason that the stall will occur first at the tip of the rotor blade at the 270 degree position. As the problem is exacerbated, then the affected section of the blade along its radius as well as various points of the disk will increase. Figure 2.5 demonstrates this in a way that is easier to visualize.

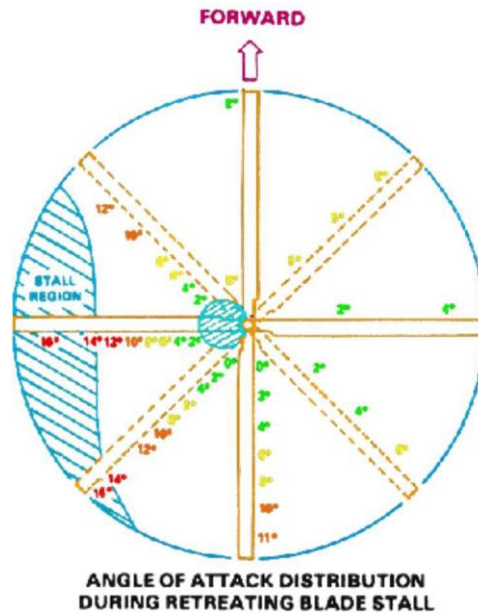


Figure 2.5 - Stall region on a rotor disk[16]

For a given flight condition, figure 2.5 demonstrates the potential distribution of the stall region. This region could be smaller or larger depending on the severity of the problem and whether or not the pilot takes proper corrective action.

It should be noted that for the purposes of this analysis, the blades are to be assumed to be both rectangular and of a uniform airfoil type and shape. It is not uncommon for higher performance helicopters to be designed with swept wing tips, geometric twist, aerodynamic twist, or any combination of them. The purpose for this is to delay the onset of retreating blade stall and increase the bandwidth of the performance limitations of the aircraft. However, because these design measures merely delay rather than eliminate completely blade stall, it is reasonable that an appropriately accurate assessment can be made with the aforementioned simplifications.

2.4 Structuring a Model

The purpose of this study, ultimately, will be to create a model of the vehicle dynamics of a coaxial helicopter in the condition of retreating blade stall. Due to the high dependence of the dynamic response on the rotor blade forces, it is paramount that the aerodynamic model possesses a fidelity that is reasonably high. This means that a thorough examination of the aerodynamics must be undertaken. This study will employ a “crawl, walk, run” methodology. The introduction of new complexities to the explored quantitative model development will only occur if it provides a meaningful addition or accuracy to the problem at hand.

The examination will begin by conducting a study on the lift distribution of the rotor disk using blade element theory. This includes not only lift and drag, but power, thrust, torque, and

efficiencies. Two distinct flight conditions will be pursued: hover and forward flight. An accurate, stable model of both conditions will be developed. Hovering brings with it the need for adequate power and for axial-translational flight. Forward flight brings with the drag profiles and downwash distributions that increase the level of complexity significantly. The modelling will provide the basis for which a time transient dynamic response can be created. Only then, after stable models have been successfully created, can a retreating blade stall condition be explored.

The last stage of the development will be to explore the differences in the application of a coaxial configuration. There will be advantages and disadvantages, as well as expansions to the performance limitations. The end state goal for the project is to have a viable prediction of coaxial rotor aerodynamics as well as retreating blade stall dynamic responses.

Chapter 3 - Blade Element Theory

3.1 The Hover Flight Regime

As discussed in previous section, blade element theory will examine the aerodynamic characteristics of an element of the rotor blade by utilizing methods that closely mimic airfoil theory. In some cases, it is helpful to marry it with momentum theory in order to reach the necessary equations. The process of determining the aerodynamic qualities is fairly straightforward when constrained to the single element. However, the complexities being to introduce themselves when one considers the all of the parts to create the whole. This is further exacerbated by the dynamic nature of even the most static of flight conditions of rotary-wing flight. It was previously mentioned that hover flight dealt with a lesser degree of complexity than forward flight, so that is where this analysis will begin.

The analysis will be performed primarily with Matlab. This will provide several advantages. The obvious one is that it will greatly reduce workload and allow for a solution that possess a greater degree of accuracy. It will also provide a means of creating a model that can be improved over time as necessary. The Blade Element Theory (BET) model created in Matlab will provide a generic model architecture that can be applied to a wide variety of rotary-wing platforms.

It should be noted that this analysis will rely heavily on the hard work that others have completed in the past and will not provide extensive derivations to the equations utilized. The reader will have to take the provided equations on faith, or seek out the reference material to satisfy the need for proofs.

The following section will provide a generic demonstration of the areas that are important to hover flight. It will be helpful to determine the angle of attack(AOA) of the rotor blade along its

span as it rotates through its periodic cycle. First, however, the velocity of the rotor blade must be found as the AOA is directly affected by the velocity.

It should be noted that this is in the preliminary stages of development and does not take into account blade flapping or blade stall. These phenomena will be explored in greater detail later in the analysis.

3.1.1 Induced Velocity and AOA of blade

Induced velocity, or downwash, is the velocity of the flow that is a direct result of the rotor system. It is the downward flow of air that is felt under the disk and directly affects the flow of the freestream velocity, which affects the angle of attack and all AOA dependant factors.

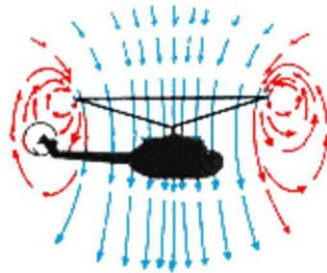


Figure 3.1 An illustration of induced velocity and tip vortices[16]

Induced velocity of the rotor blade along its own span(v_i) can be found with the following relationship:

$$v_i = v_{\infty} \left(-\frac{C_L}{4\pi b} \right) + \left(\frac{C_L}{2\pi b} \right) + 1 \left(\frac{C_L}{4\pi b} + \frac{v_{\infty}}{V_{tip}} \right)^2 + \frac{C_L}{4\pi b} \frac{V_{tip}}{V_{\infty}} \quad (3.1)$$

v_{tip} is the rotor tip velocity.

C_L is the the coefficient lift slope for the particular blade element. In the case of a uniform blades, and while ignoring stall effects, it is a reasonable assumption to treat each element as though having the same lift slope.

b is the number of blades the rotor system has, while c_r is the chord of the blade at station r .

v_{z7} is the climb velocity, which assumes vertical climb along the aircraft's z-component. $v_{z7} = 0$ during hover, but is a critical factor in vertical translational movement.

R is the length of the whole rotor blade. The BET model architecture allows for a user defined level of accuracy. The user simply inputs the desired number of steps, and the invoked level of accuracy will be provided.

Figure 3.2 Shows the induced velocity along the span of the blade

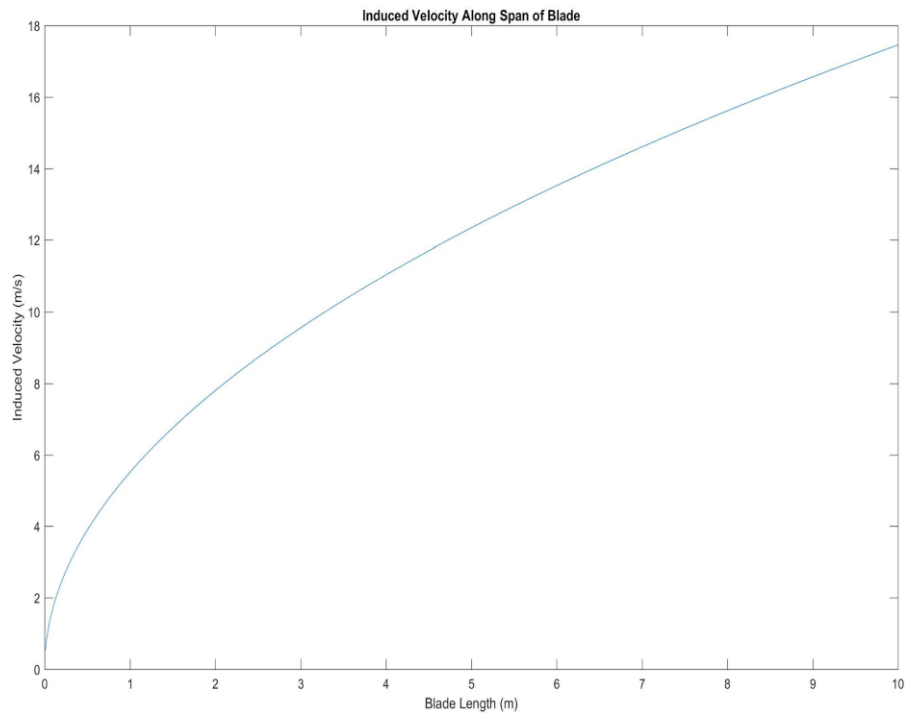


Figure 3.2 Induced velocity along span of blade

Now that the velocity at station r has been determined, the angle of attack (α) for each station can be found.

$$\alpha = \alpha_0 - \frac{v_{z7}}{v_{t7}} \quad (3.2)$$

Where theta is the radial about the axis of rotation, and Omega is rotational velocity of the rotor system. Figure 3.3 demonstrates the distribution of the AOA along the span of the blade while at the 90 degree radial. The data for the following plots reflects the dimensions and characteristics of the Robinson R22.

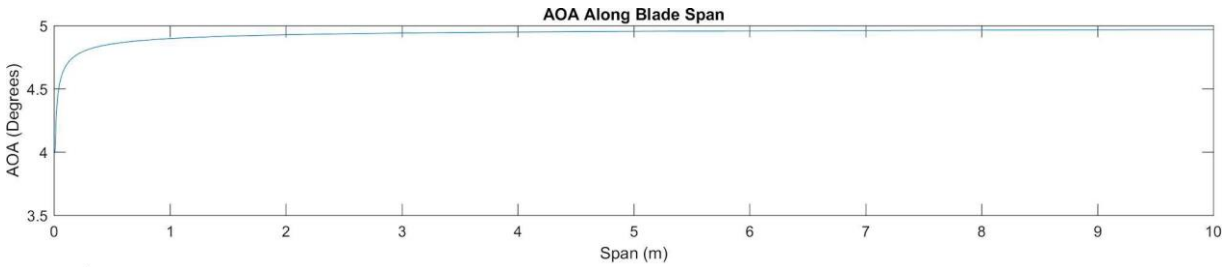


Figure 3.3 AOA along blade span

Figure 3.3 shows a distinct climb in AOA close to the root of the blade with an initially extreme climb to a nearly asymptotic end as it reaches the tip. While it appears that there is a discernible increase in AOA, it would be a reasonable assumption to say that the AOA is uniform across the blade.

3.1.2 Lift and Drag of the Element

Lift for the rotor blade is found with the following:

$$L = \frac{1}{2} \rho (V - \frac{7177}{2})^2 C_L \quad (3.3)$$

ρ , in this case, is the density of the air.

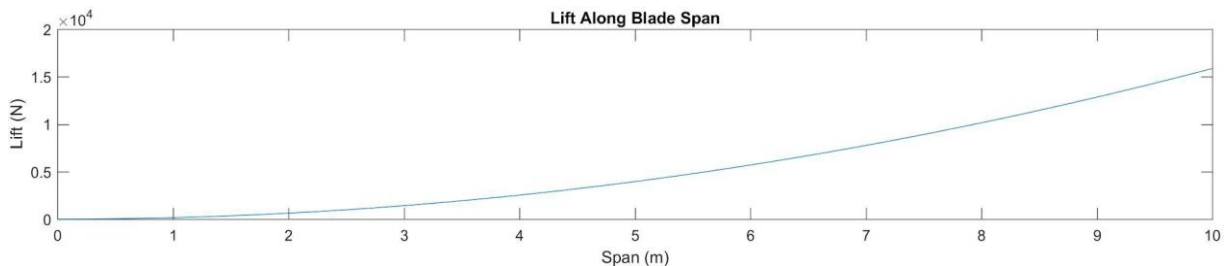


Figure 3.4 Lift along blade span

Lift, as always, is influenced by the square of the velocity and figure 3.4 aptly demonstrates the rapid increase in lift along the span. While it does not provide any specific details, it does show the trend and provides a visualization of how there might be a great potential for a blade to flap based on the higher lift forces out toward the tip of the blade.

Drag is very similar in the sense that it is a function of the square of the velocity:

$$C_d = \frac{1}{2} \rho V^2 C_{d0} \quad (3.4)$$

C_d is the coefficient of drag as it relates to skin friction drag. Induced drag, or drag as a result of lift, is also a major contributing factor that should be taken into consideration,

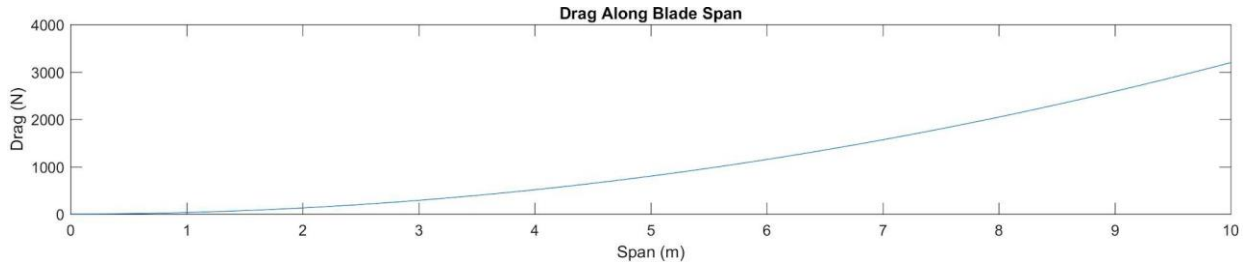


Figure 3.5 Drag along the blade span

Although there are subtle differences, the drag and lift diagrams demonstrate similar profiles.

3.1.3 Torque

Determining the torque produced by the main rotor is of great concern to those who design and fly helicopters. The main rotor and the tail rotor are some of a helicopters physical attributes that truly help to make it a unique aircraft class. The amount of torque that is developed by the main rotor must be counteracted by the tail rotor, which is controlled by the anti torque pedals.

$$Q = \frac{1}{2} \rho V^2 C_{T0} \quad (3.5)$$

Where α is the inflow angle of the airflow

$$C_{T0} = (C_{T0} \cos(\alpha)) + C_{T0} \sin(\alpha) \quad (3.6)$$

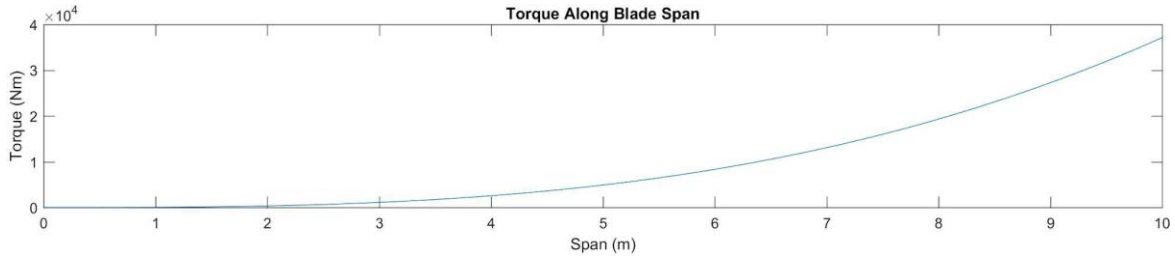


Figure 3.6 Torque along blade span

Predictably, the amount of torque increases further out from the blade root.

3.1.4 Thrust

A cursory examination of the following equation shows the relationship between thrust, lift, and drag. To those that are familiar to aerodynamics in general, it should come as no surprise that the thrust is a function of lift with the drag subtracted out.

The following equation, like those previously mentioned, applies to a single element, and requires that the thrust be integrating along the span of the blade.

$$T = L - D \left(\frac{1}{\cos \alpha} \right) \tag{3.7}$$

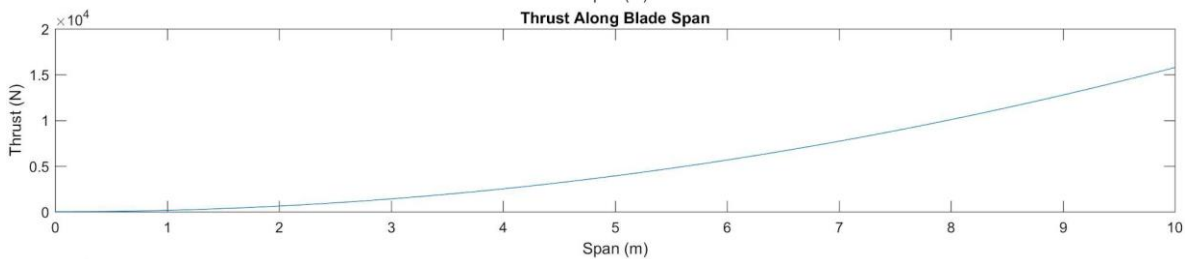


Figure 3.7 Thrust along blade span

Figure 3.7 shows a similar trend to the previous graphs and it comes as no surprise to see an increase slope as more distance to the tip is reached.

3.1.5 Power

It logically follows that in order to achieve specific performance benchmarks, an adequate amount of power needs to be made available in order to reach said benchmarks. In reality, the rotating blades will produce drag in several forms: skin-friction, induced drag, wake drag, and pressure drag to name a few. The two that concern the engineer and the pilot the most, for all intents and purposes, will be the skin friction drag and the induced drag. The design intent behind a rotor system to maintain the rotational velocity of the rotor system to remain constant. This is so that lift, and thus translational lift, can be controlled directly with angle of attack changes throughout the disk. If a constant angular velocity is maintained, then the skin friction drag should remain fairly constant in a hover. However, introducing AOA to climb or induce translational flight results in a greater level of induced drag. That is not to say that the rotor blades will no produce a greater skin friction drag during translational flight. Drag is still a function of the square of the velocity. The induced drag, however, is going to produce the greatest change in drag in the least amount of time. This drag needs to be overcome in order maintain the required RPM.

Figure 3.8 Shows the trend of power required along the span of the blade. While it does maintain a trend that is remarkably similar to the previous data plots, it should be noted that the power toward the tip increases at a greater rate than the drag plot.

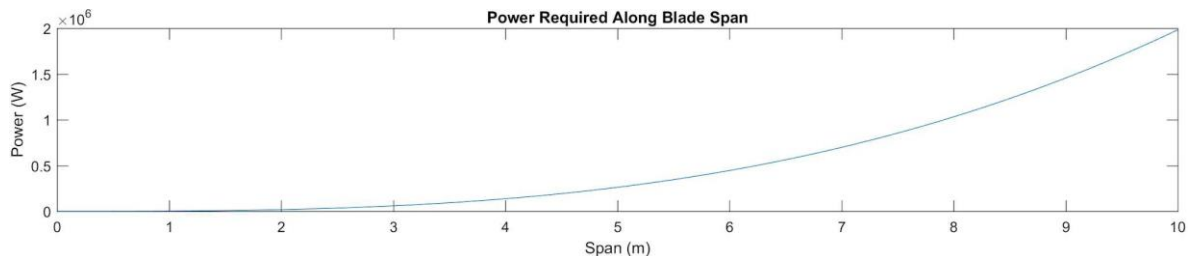


Figure 3.8 Power required along blade span

The performance of the engine or engines is of great importance to the overall design of the aircraft and should not be understated. In certain cases, it might be possible to bottleneck the performance of the helicopter due to a lack of power. This could result in an inability to control the aircraft or perhaps even stall the aircraft prematurely. Engine power is important in any aircraft, but it is especially important when designing a rotary wing aircraft.

Engine related to torque, and is found with the following relationship:

3.2 Interpreting the results

A quick examination of the graphs above demonstrate a consistent and obvious trend: each force or reaction increases its prominence the further away from the hub along the blade it is. While this has been an elementary examination at best, the results are very telling. Each of the forces are ultimately affected in the way that they are due to the increase of velocity along the span. This means that the greatest level of lift, drag, power, torque, etc occurs toward the tip. Because such a large dependence on the aircraft's performance will ultimately rely on the outer sections of the disk more heavily, any change on the outer section will have greater influence on the behavior.

It is understood that retreating blade stall will occur beginning at the blade tip and work its way inward as the problem becomes exacerbated. This could result in tragedy because the airframe may rely heavily on the available lift on that rotor section, which will disappear during a stall.

Even without examining the extreme conditions that lead to blade stall, one can consider what might occur if blade tip losses are factored in. Blade tip losses have not yet been explored in the analysis, but will be closely examine later in this analysis. All that needs to be understood and this juncture is that the blade tips lose efficiency, and thus their ability to generate lift compared to the ideal case. Suddenly, the lift, power, etc., requirements have completely changed.

In order to mitigate the problems associated with this phenomenon, a great effort must be made to ensure that distribution of the aerodynamic qualities are as evenly distributed across the blade as possible. This might be achieved by blade washout, also known as geometric twisting, or aerodynamic twisting. Not only is this important due to efficiency and controllability in all regimes of flight, but also in structural integrity and longevity of the rotor blades.

3.3 Next Steps

Moving forward, the next step will be to examine the above qualities with a more thorough understanding and a higher level of fidelity. The above, while applied in an elemental structure, relied heavily on momentum theory. Blade element theory in its entirety will provide a solution with a higher degree of fidelity.

Increases the fidelity of the analysis will include integrating concepts such as blade tip losses, slipstream conditions, power losses due to slipstream, rotor thrust and power in climb and

hovering conditions, as well as maximum thrust performances. After that is concluded, examining the performance due to overlapping blade systems will be necessary to determine the qualities of a coaxial platform.

Once the hover is complete, the framework for transitioning to forward flight will be established and the analysis of forward flight can begin. These two flight regimes will provide the basis for which the dynamic model can be built and examined and a transient time domain.

Chapter 4 - Rotor Disk Dynamics

Chapter 3 discussed in some detail the application of Blade Element Theory in the hovering regime. While it was certainly less than all encompassing, it was sufficient for providing an understanding of how to calculate the lift in certain conditions with an acceptable level of fidelity. What would remain is an in depth analysis of the aerodynamics as it pertains to the forward flight regime. The aerodynamics of this condition is fairly complex, as is rotorcraft aerodynamics in general. A full appreciation of the aerodynamics concerning helicopters would take a great deal more scrutiny than what is needed for this study. However, the model can be simplified without compromising on accuracy beyond an acceptable limit for the purposes of this analysis.

If major aerodynamic phenomena, such as vorticity, side slip, and other such occurrences are assumed to be negligible, then the Blade Element Theory will provide a straightforward means of determining the forward flight condition. The lift of any given element within a rotor blade is a function of the relative velocity of the wind over and under that blade element. This relative velocity must change as the blades rotate due to the forward component of travel. The relationship that describes this change in velocity is as follows:

$$U_t = \Omega R + V_\infty \cos(\alpha) \sin(\psi) \quad (4.1a)$$

Or in non-dimensional terms:

$$U_t = r + \mu \sin(\psi) \quad (4.1b)$$

Figure 4.1 illustrates how the velocity, in conjunction with the angular velocity, creates a situation where the velocity profile over the disk changes. This changing velocity profile motivates the final goal of the analysis.

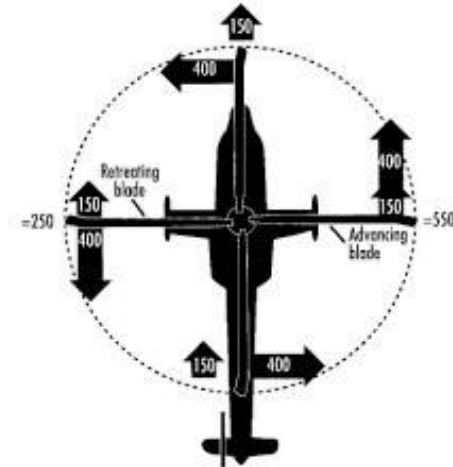


Figure 4.1 A demonstration of dissymmetry of lift

4.1 Establishing a model

In order to establish the foundation of a dynamic model, a low fidelity analysis that can be enhanced in the future will be built. There are important aspects to consider when constructing a model. These include:

- Aerodynamics
- Rotor system types
- Blade flapping

The aerodynamics have been addressed in previous sections and will not be elaborated upon further until a higher fidelity analysis is required. It is important to note that the exploration of the aerodynamics is not all encompassing and should be taken as a baseline in which to determine behavioral trends.

The most critical piece in this analysis is the rotor flapping. In reality, rotary wing flight is possible only because of blade flapping, and cannot be neglected. The importance of flapping will be covered in a later section when a detailed account of blade flapping is made and implemented into the modelling.

4.2 Rotor System Types

Determining the various rotor system types is an important detail to examine because it will directly affect how the lift of the disk influences the whole body. This fact might appear obvious

on the surface, but a bit of scrutiny will show that the issue is a bit more complex. The real differences will become apparent in the flap analysis.

Rotor systems can be reduced into three main categories: Rigid rotor systems, articulated rotor systems, and teetering rotor systems.

4.2.1 Rigid Rotor Systems

A rigid rotor system, as the name implies is a system that is primarily rigid, but relies on the flexibility of the rotor blades to absorb the stresses of the blade flapping and the torsion produced by the lead-lag effect.

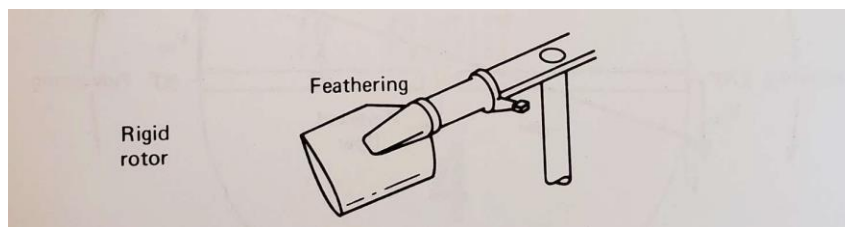


Figure 4.2 Rigid Rotor System[15]



Figure 4.3. A Bo105 which utilizes a hingeless rotor system, photo courtesy of RedBull.com

The advantage to this type of system is that there is a higher response to control inputs. This is due to the moments that are created by the blades which are directly translated to the fuselage of the helicopter. Handling responses are described as being sensitive with little latency. The disadvantage to this type of system is that the rotor blades need to be much stronger and are thus

heavier. Also, the rigid rotor system translates any perturbations due to turbulence to the helicopter which can cause for a bumpier ride in choppy air.

4.2.2 Articulated Rotor System

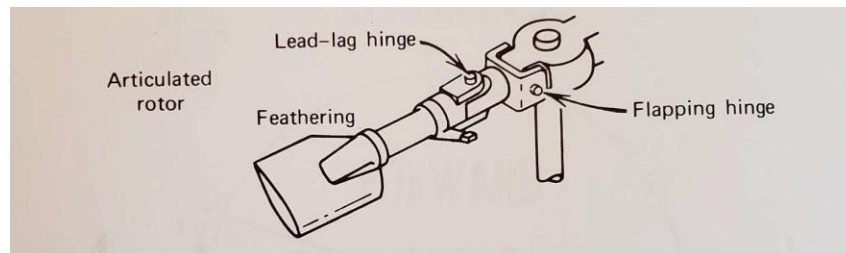


Figure 4.4 Articulated System [15]



Figure 4.5. SH-60R, utilizing an articulated rotor system. Photo courtesy of LockheedMartin.com

Articulated Rotor Systems are such that the individual blades are mounted to the swashplate hub via a hinge that allows the blade to freely flap up and down. Fully articulated systems allows flapping hinging as well as a hinge that provides the blade the freedom of movement to swing fore and aft through the rotation. These hinges are often offset from the axis of rotation so that even with the freely flapping blades, a moment may still be imparted upon the fuselage

4.2.3 Teetering Rotor System

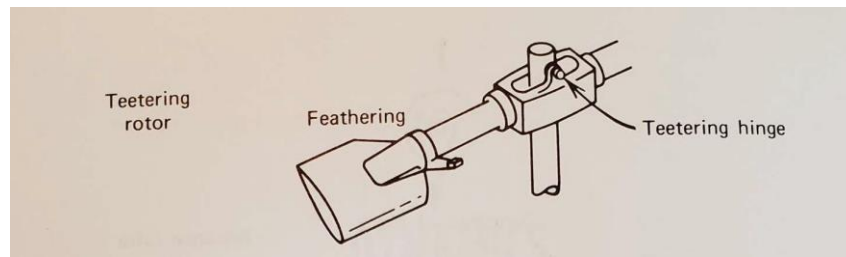


Figure 4.6 Teetering Rotor System [15]

The teetering rotor blades teeter much like a seesaw found on a playground (figure 4.6). This allows the blades to flap together in synchronized motion. This system is the lightest of the three. However, it imparts zero moment to the helicopter directly as a result of its flapping. This type is limited to only two bladed systems.



Figure 4.7 UH-1 Iroquois, photo courtesy of wikipedia.com

Choosing a specific rotor system will have profound effects on the simplicity of the model, as well as contribute to the layers of complexity involved with its construction. For the purposes of the analysis, the teetering rotor system will be chosen. This provides the advantage of limiting the lifting bodies to only two rotor blades. It also allows for the dynamics of the rotor disk to be observed independently of the rotor hub and then apply those findings at a later time. With regards to the phasing of the blade flapping, the two bladed teetering system will possess phases at 90 degrees which will simplify the analysis.

4.3 Static Versus Dynamic Stall

An area of aerodynamics that is of particular importance is the occurrence of stalls. While stalls can be classified in several different categories that manifest themselves in specific ways, there are two types that are of particular interest here.

The first type of stall to be discussed is the static stall. Static stall occurs in the context of steady aerodynamics when the angle of attack of the lifting surface in question exceeds its critical angle of attack. Angles of attack in excess of the static critical angle of attack result in a loss of lift. The recovery from a stall condition is achieved by reducing the angle of attack of the aircraft below the critical angle of attack. For dynamically stable aircraft, the physical manifestation of this is a natural nose-down tendency of the airplane so that the recovery can be achieved. An emphasis should be placed on this being a stable aerodynamic occurrence. Figure 4.8, from NASA, provides a visual representation of effects that stall has on airflow.

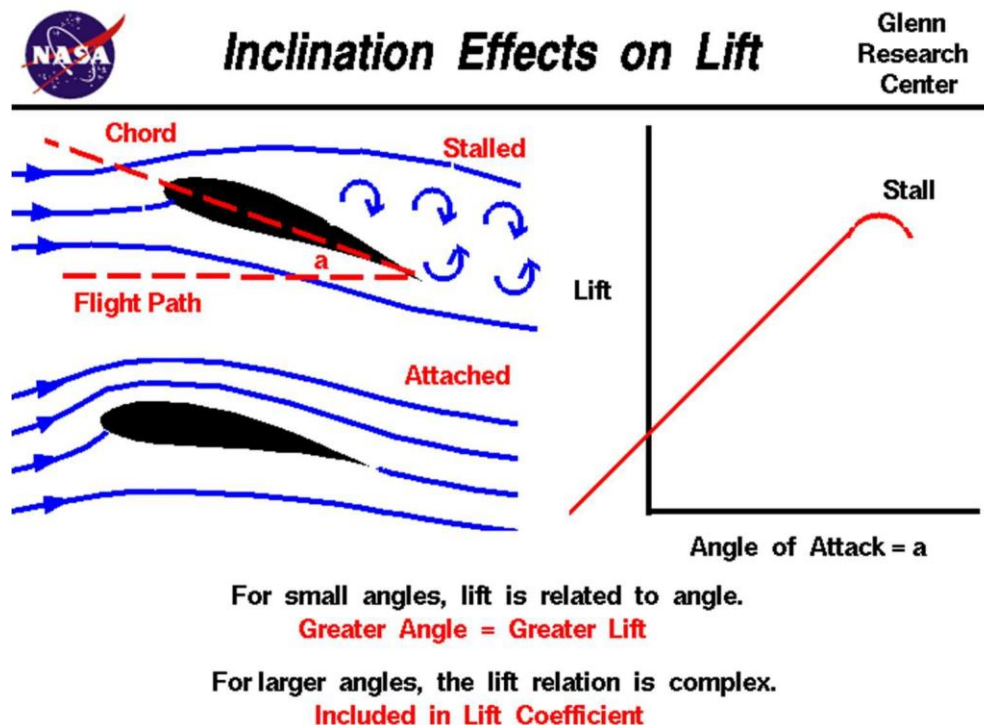


Figure 4.8 NASA illustration demonstrating the change in flow after the airfoil has reached critical angle of attack[17]

Dynamic stalls occur in an unstable environment, such as the constantly changing state of a rotary-wing. In the next section, a discussion about blade flapping will expose the idea that the angle of attack experienced by the rotor blade constantly changes periodically through the rotation about the rotor shaft. This dynamic state means that the way that stall is evaluated must be examined differently than in static situations. There are two elements of dynamic stall that

separate it from static stall. The first is that the critical angle of attack for a dynamic stall is often higher than that of the static stall. In practical terms, this means that a greater coefficient of lift is achievable. The second element is that there is a delay in the onset of a dynamic stall. Rotor blades are spinning about their axis at such a high angular rate that often the blade can be pushed beyond critical AOA and recover below a “safe” AOA before stall can onset. Eqn. 4.2 shows an empirical relationship between static and dynamic critical angles of attack that can be utilized to approximate dynamic stall relative to static stall [13].

$$\alpha_{ds} = \alpha_{ss} + C_1 \left(\frac{\dot{\alpha}c}{V_\infty} \right)^{1/2} \quad (4.2)$$

Where C_1 is a function of Mach number and is obtained from airfoil data.

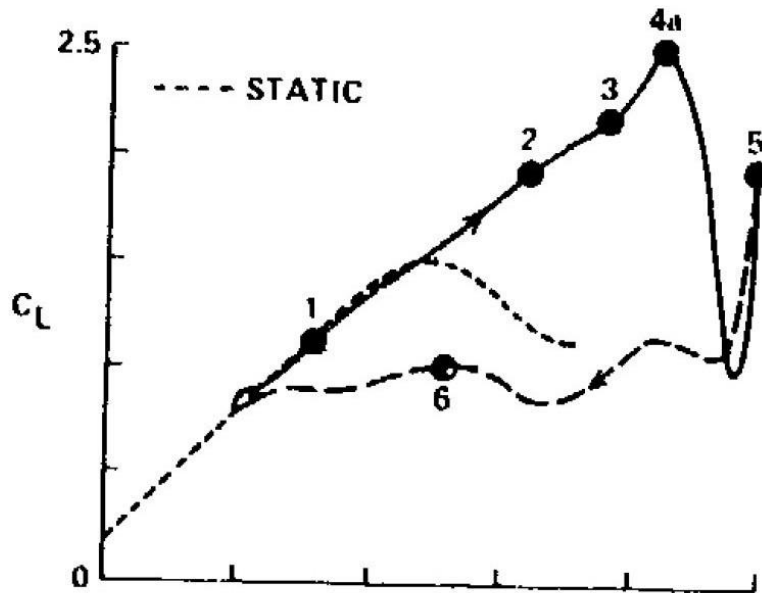


Figure 4.9 Dynamic vs static stall, C_L vs AOA [18]

The severity of the dynamic stall is dependent on the severity of the flow separation. Dynamic stall responses, due to the aforementioned lag or delay, do not recover in the same way that static stalls do. Rather than simply reducing the AOA below the critical angle to restore attached flow and lift, the angle of attack must be reduced significantly. Figure 4.10 Shows how the deeper the stall, the further the AOA must be reduced in order to recover.

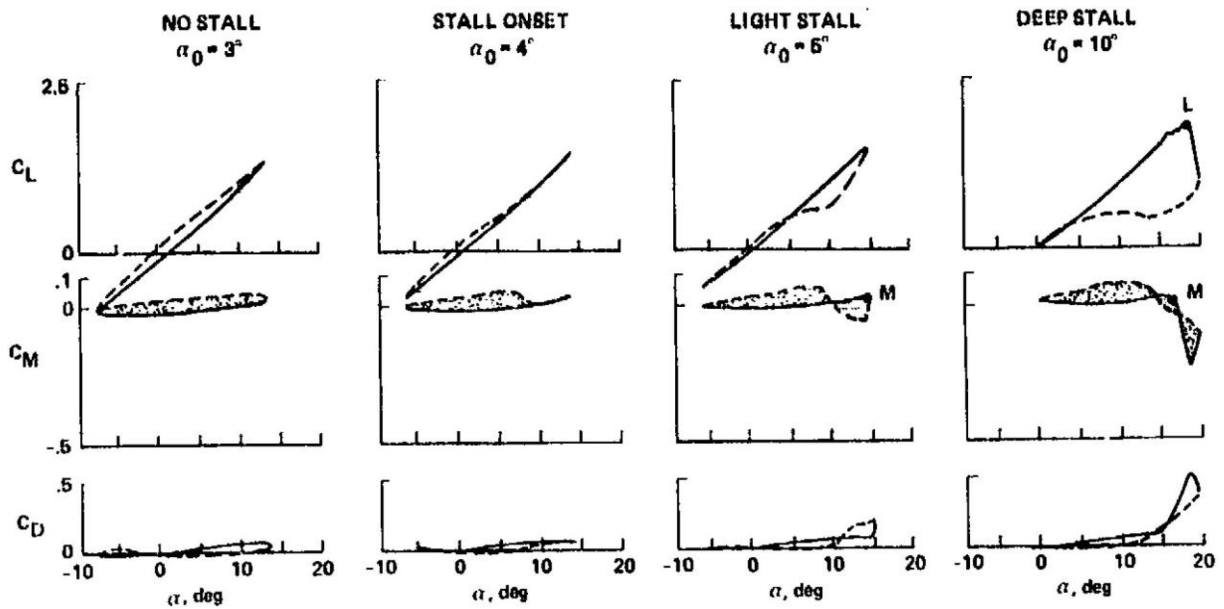


Figure 4.10 The dynamic stall C_L as the AOA is decreased after inducing stall. Solid lines denote increasing, dashed lines denote decreasing [18].

The subject of dynamic stall and unsteady flow is an area of study that is highly complex and worthy of an in depth study on its own. Needless to say, it is beyond the scope of this study, but would be an area to explore if the subject of this study were to be expanded upon in an effort to create a model with higher fidelity. It is important to understand the physical occurrences to aid in analyzing and understanding the angle of attack results later in the study.

Chapter 5 - Blade Flapping

5.0 Rotor Disks are not Gyroscopes

It is not uncommon for the motion of helicopter disks to be compared with and evaluated as gyroscopes. The apparent precession that occurs 90 degrees out of phase on a rotor disk that has an applied force looks and behaves just like a gyroscope. However, it is helpful to realize that it is not actually gyroscopic precession that occurs in a rotor disk whose blades are allowed to flap independently. While it is, strictly speaking, outside of the scope of this analysis to dissect the differences between a gyroscope and what a rotor disk is, it may provide some insight to the flapping motion that occurs.

Recall that a gyroscope is a rigid body that spins with angular momentum. A moment applied to the gyroscope causes the angular momentum vector to change and triggers the precession. The key in this instance is that the rigid body, by its very nature of being rigid, is directly influenced

by be an applied force which causes a moment to the body. In this context, that force would be the lifting force, or net lifting force seen by the disk.

Now consider what is considered the most basic and fundamental rotor system that can be analyzed: the articulated rotor blade with a hinge located at the center of rotation. The purpose of the hinge is two-fold. First, the blades must be allowed to bend and flex in order to naturally compensate for the dissymmetry of lift that the disk generates. This is the flapping that will be examined with a higher degree of scrutiny later. Without flapping, rotorcraft flight would not be possible. Early helicopter design prototypes were engineered with rigid rotor blades that were not allowed to flap, which led to disastrous consequences. It was realized that flapping was, indeed, necessary. Helicopter blades are going to flap whether or not they are attached to a hinge. However, there are extreme loads that the blade must endure. If the blade is hingeless, then the blades root must be strong enough to take the stress. Some helicopters are designed this way, however, it is fairly common for helicopters to have either a teetering or articulating rotor system to eliminate any stresses and moments on the rotor hub, thus allowing the blade to be much lighter.

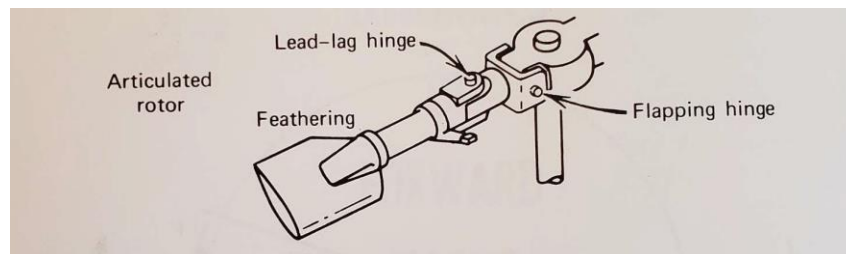


Figure 5.1. A fully articulated blade with a flapping and lead-lag hinge [15]

It is important to emphasize that a hinged rotor blade imparts zero moment to the hub. Effectively, the flapping motion is completely independent of the rest of the airframe. Helicopter blades that are spinning in motion have three forces acting upon them: The weight of the blade, the lifting force, and the centrifugal force due to the spinning. Drag is also present, however, since $L \gg D$, drag will be neglected for the time being.

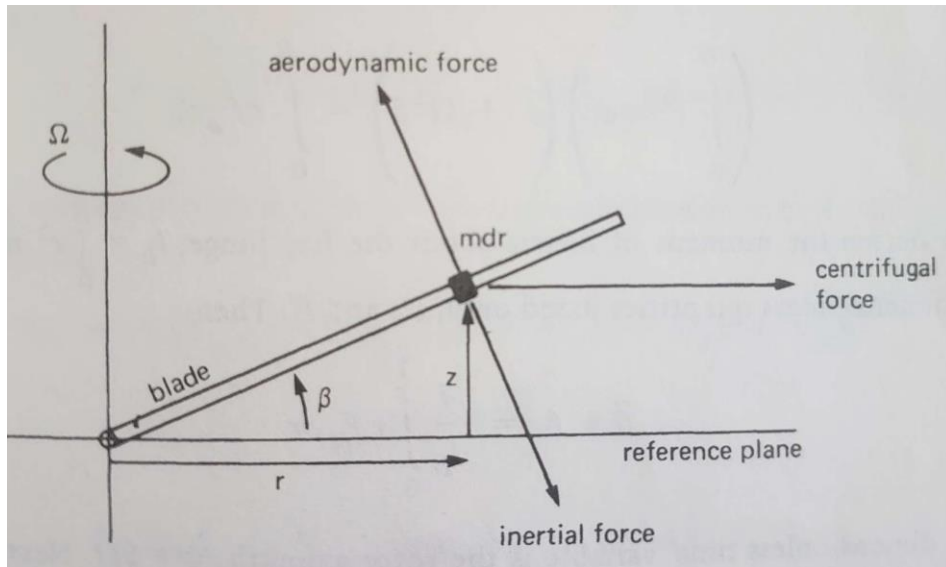


Figure 5.2. Forces acting upon the rotor blade [13]

The centrifugal force plays the largest role in preventing a rotorblade from flapping upward and coning to high degrees. It behaves and is often modeled as a spring force counteracting the lift force.

This lift force varies as the blade rotates about the axis of rotation while the other forces remains the same. The blade will flap up or down until equilibrium between the three forces are achieved and constantly flaps throughout the rotation to achieve and maintain said equilibrium. The flapping has the benefit of adjusting the effective angle of attack seen by the blade to help balance and maintain a symmetric lift distribution. More on that later, but for the moment, consider the physical implications of an articulated blade. If there is zero moment being imparted upon the hinge, then the blade is free to move within its degrees of freedom and there will be no real influence to the rest of the system. This allows us to analyze each of the blades separately and individually, but it is also the first step in disconnecting the concept of helicopter control from gyroscopic precession.

The next question is: how is the helicopter then controlled if not through gyroscopic precession? Let us look at the physical process of the rotorcraft in forward flight. For the sake of simplicity, we shall make the assumption a helicopter in hover is in an ideal environment with no perturbations or disturbances. Therefore, a helicopter in the hover flight regime does not flap but simply cones. Upon taking off, the lift generated by the blades causes the blades to flap up until it reaches a state of equilibrium with the centrifugal and weight forces. There is a constant cone angle formed by the blades through the rotation as a result (Figure 5.3). In order to induce forward flight, and control input is required to change the state of equilibrium.

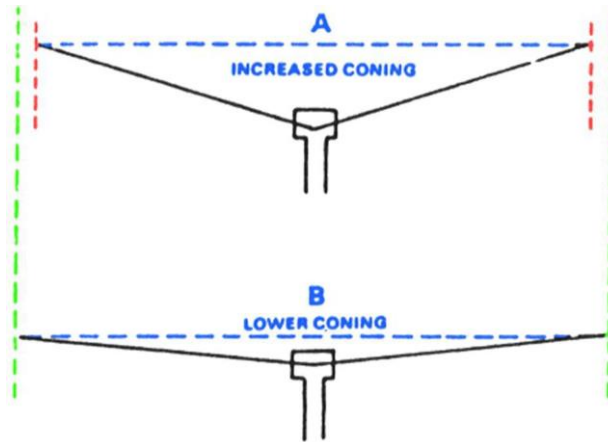


Figure 5.3. The change in coning angle with an increased loading [19]

Per convention, let us assume that the reference frame of the helicopter disk starts at zero degrees with zero pointing toward the aft of the helicopter, toward the tail, 90 degrees points to the starboard (right) side, 180 degrees points forward, and 270 degrees points to the port (left) side of the helicopter, as depicted in figure 5.4.

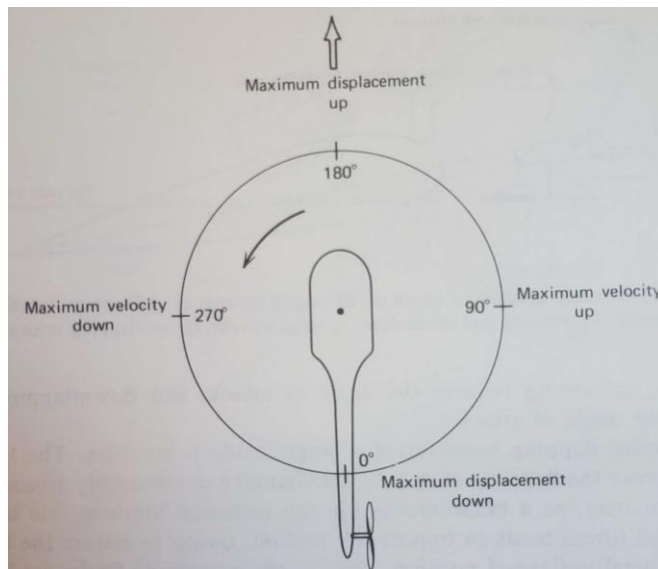


Figure 5.4.. The helicopter reference frame with a control input inducing forward flight [15]

Forward flight is achieved by a control input which induces a change in the incidence of the blade as it rotates so that more lift is generated at 270 degrees. The aircraft will exhibit a response 90 degrees later when it pitches forward just as one might expect in gyroscopic precession. What is actually happening is that more lift is being generated on the retreating side around 270 degrees which is causing the blade to flap up, which carries with it momentum. The rotor disk will rotate (precess), or pitch, forward until forward velocity is built up. Once this occurs, the advancing side of the blade start generating more lift which induces a flap up motion.

This flap up motion decreases the angle of attack. Flapping down increases the angle of attack. The steady state flapping motion throughout the rotation is achieved when the forces are in equilibrium for the given control input. In essence, the control inputs are effecting a change in the equilibrium location of the rotor disk.

The change in angle of attack due to flapping as caused by the vertical velocity component that is introduced as a by-product of the flapping. It is through this specific mechanic that the rotor disk naturally accounts and compensates for what would ordinarily be a dissymmetry of lift situation. Figures 5.5 and 6.5 demonstrate how the angle of attack changes with respect to the direction of the flapping.

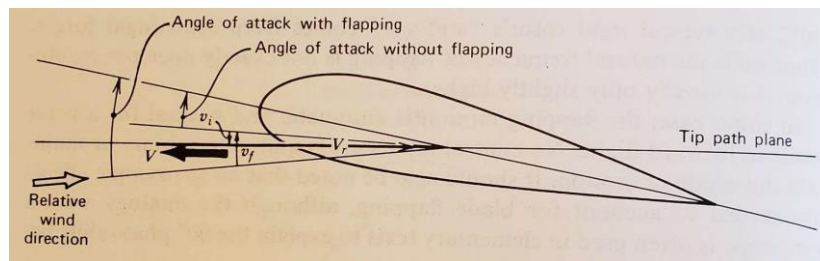


Figure 5.5. flapping up increasing angle of attack[15]

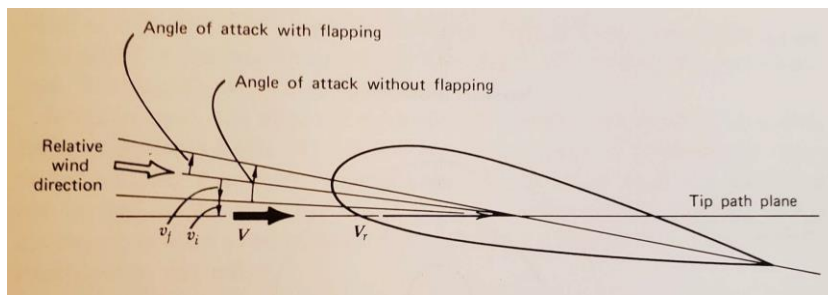


Figure 5.6. flapping down decreasing angle of attack[15]

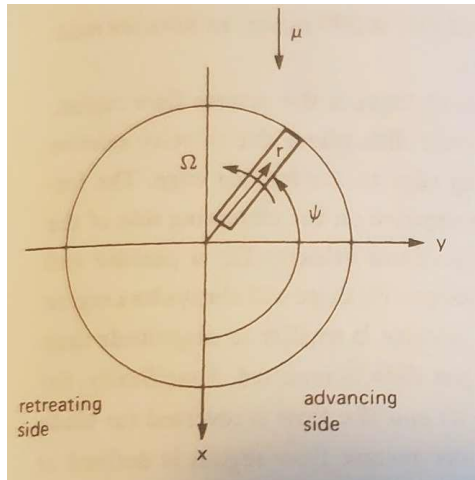


Figure 5.7. Non-Rotating frame helicopter viewed from above[13]

Standard convention for American made helicopters is that the rotor rotates counter clockwise as viewed from above.

Some European helicopters companies, such as the French company Airbus, design their helicopters to rotate clockwise when viewed above.

As is the case when evaluating lift over fixed wings, the most important part of the velocity that affects the blade is the perpendicular component. The equation representing this in non-dimensional terms is:

$$U_{\perp \bar{r}} = \Omega \bar{r} + \mu \sin(\psi) \quad (5.1)$$

Where Ω is the angular velocity at the rotor tip, μ is the advance ratio $(\frac{V}{\Omega R})$, which is the ratio of forward velocity to rotor rotational velocity, ψ is the angle of rotation, and \bar{r} is the non-dimensional radius.

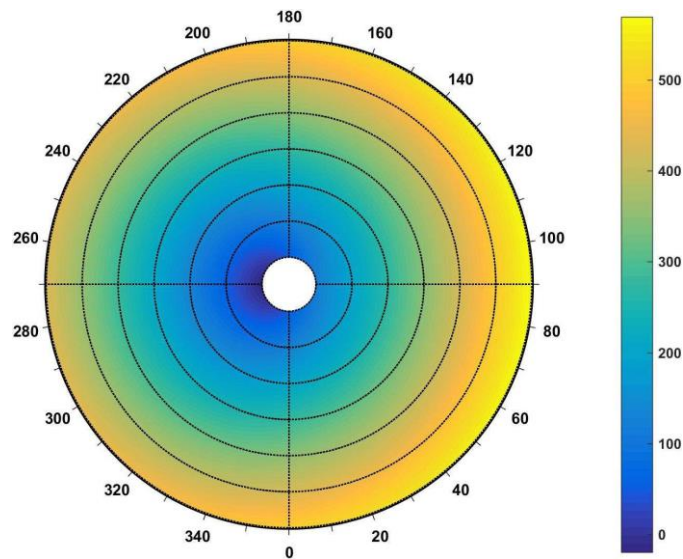


Figure 5.8. Velocity profile about rotation in forward flight

In figure 5.8, it can be seen that the advancing side of the rotation will have a greater velocity than the retreating side. A simple association to the lift equation reveals that there would be an asymmetric distribution of the lift over the disk. A physical manifestation of this would be an uncontrollable rolling moment. Blade flapping is the key to countering this.

5.1 Lead-Lag

Despite being beyond the scope of this study, briefly exploring the mechanics behind the lead-lag phenomenon of the blade will be helpful in dissociating rotor disks from gyroscopes.

As previously discussed, lift generated by the blade as it rotates about the shaft induces flapping motion. Figure 5.3 shows that as the flapping angle of the blade increases, then the effective radius becomes shorter. Recall that due to conservation of angular momentum, when the moment of inertia of an object is reduced, the angular velocity must increase in order to conserve angular momentum. The quintessential example of this is the ice skater example with which all engineers should be familiar. This same phenomenon occurs on each individual rotor blade as it rotates through a revolution. As the flap angle increases, the radius within the plane of rotation is reduced and the rotational velocity increases. The effect is that blade bends as it speeds up or slows down. The stresses of this are great and add to the stress experienced by the root. On strong, hingeless systems, the rotor blade is designed to be strong enough. For an articulated blade, an additional hinge is added to allow for freedom of movement within the plane. See figure 5.1. Centrifugal force is, again, responsible for maintaining a rigid-like appearance and

behavior to the blade. The lead-lag hinge allows the blade to swift for and aft as physically necessary to maintain angular momentum.

One final discrepancy between gyroscopes and rotor disks is found in the implementation of hingeless and hinged blades with an offset. Articulated and teetering blades have a 1/revolution natural frequency that provides the 90 degree offset that we recognize in gyroscopes. Hingeless and offset hinges, however, produce a natural frequency of greater than 1/rev. Effectively what this means is that rather than having a 90 degree phase lag between force induction and dynamic response, it is found that the phase lag is in the 70-80 degree range.

5.2 Modelling the flapping

In order to appropriately determine the rotorcrafts stability and, later on, its behavior, a modelling of the blade flapping must be conducted. This evaluation is critical in that it determines the mechanics behind the angle of attack changes that occur as a result of the flapping that allows the rotorcraft to maintain a symmetric, and thus stable, lift distribution along the rotor disk.

There are two methods that can be used to determine the flapping motion, both of which will be explored here. The first to be examined is the differential equation of motion of blade flapping that is solved as a numerical solution utilizing RK45. To facilitate this, Matlab ODE45 function is used.

The second method is a Fourier series solution. As a reminder, the Fourier series is as follows:

$$\beta(\psi) = \beta_0 + \sum_{n=1}^{\infty} (\beta_{nc}\cos(n\psi) + \beta_{ns}\sin(n\psi)) \quad (5.2a)$$

For the purposes of this analysis, only the first harmonics are necessary to accurately depict the flapping motion of a rotor blade, and thus the series can be truncated. β_0 represents the coning angle of the blades as they rotate through the reference frame. β_{1s} and β_{1c} are the coefficients for the series that represent the flapping angles through the longitudinal and lateral sections of the rotation. Thus:

$$\beta(\psi) = \beta_0 + \beta_{1c}\cos(\psi) + \beta_{1s}\sin(\psi) \quad (5.2b)$$

Wayne Johnson [13] provides a development for the Fourier coefficients to be utilized in the evaluation which come from the development of the EOM's. The equations of motion will be developed first so as to move on to the two solutions.

The EOM's that were evaluated for flapping stability in the previous section will be reexamined with the lift of the blade, as a forcing function, in mind.

Figure 5.2 shows the free body diagram of a freely articulating blade and the examination of a particular particle.

As figure 5.2 shows, there are three forces acting on the mass element.

1) The inertial force that opposes the flap motion, given by: $m\ddot{z}t = mr\ddot{\beta}$

Where r is the radial distance from the hinge

2) the force referred to as centrifugal force $m\Omega^2r$, which is directed outward, radially, and possesses a moment arm $z = r\beta$.

3) The force normal to the blade. For small angle approximation, this is simply the lift force, L .

The reader should realize that centrifugal force always acts radially outward and opposes the flapping motion. As a result, it can be evaluated as a spring-like force. The reader should also be reminded that centrifugal force is not an actual force, but rather a reaction to centripetal acceleration. It is simply being explained as a force in order to model the dynamics.

There is no hinge-flap spring in this system, therefore the sum of the moments must equal zero. This leaves us with:

$$\int_0^R mr\ddot{\beta}dr + \int_0^R m\Omega^2r(r\beta)dr - \int_0^R F_z r dr = 0$$

Collecting terms:

$$\left(\int_0^R r^2 m dr \right) + \left(\ddot{\beta} + \Omega^2 \beta \right) = \int_0^R r F_z dr$$

Recall that the moment of inertia can be defined as:

$$I_b = \int_0^R r^2 m dr$$

Utilizing dimensionless quantities the EOM's become:

$$\ddot{\beta} + \beta = \frac{1}{I_b} \int_0^R r F_z dr \quad (5.3)$$

The Lock number is the dimensionless parameter that represents the ratio of aerodynamic to inertial forces, and it contains the only influence of rho in the dimensionless analysis.

$$\gamma = \frac{\rho a c R^4}{I_b} \quad (5.4)$$

The equations of motion become:

$$\ddot{\beta} + \beta = \gamma \int_0^R r F_z dr \quad (5.5)$$

The dimensionless lift force is:

$$\frac{F_z}{ac} = \frac{L}{ac} = \frac{1}{2} u_T^2 \alpha = \frac{1}{2} (u_T^2 \theta - u_p u_T) \quad (5.6)$$

u_T and u_p are defined as:

$$u_t = r + \mu \sin(\psi) \quad (5.7)$$

$$u_p = \lambda + r \dot{\beta} + \beta \mu \cos(\psi) \quad (5.8)$$

Not that u_p term contains both β and $\dot{\beta}$ which will play a critical role in correctly evaluating the flapping angle and response of the blade.

Also,

$$\theta = \theta_0 + \theta_{1c} \cos(\psi) + \theta_{1s} \sin(\psi) \quad (5.9)$$

- θ_0 is collective input
- θ_{1c} is pitch cyclic input
- θ_{1s} is roll cyclic input

The aerodynamic flap moment is thus:
$$M_F = \int_0^1 r \frac{F_z}{ac} dr \quad (5.10)$$

At this point, the utilization of differential equation and the Fourier series differ somewhat. With the differential equation, the above development suffices. It can be evaluated utilizing RK45 or similar numerical solver solutions. The Fourier Coefficients require more development. The development is lengthy and complex, and will not be developed here. The inquisitive reader is invited to explore the derivation made by Wayne Johnson[13].

The result is a set of algebraic expressions that can be solved for the individual harmonics:

$$\beta_0 = \gamma \left(\frac{\theta_0}{8} \right) (1 + \mu^2) + \frac{\theta_{TW}}{10} \left(1 + \frac{5}{6} \mu^2 \right) + \frac{\mu}{6} \theta_{1s} - \frac{\lambda}{6} \quad (5.11)$$

$$\beta_{1s} = \left(\frac{1}{8} \theta_{1c} \left(1 + \frac{1}{2} \mu^2 \right) - \frac{\mu}{6} \beta_0 \right) / \left(\frac{1}{8} + \frac{\mu^2}{16} \right) \quad (5.12)$$

$$\beta_{1c} = \left(\frac{1}{8} \theta_{1s} \left(1 + \frac{3}{2} \mu^2 \right) + \frac{\mu}{3} \theta_0 + \frac{\mu}{4} \theta_{TW} - \frac{\mu}{4} \lambda \right) / \left(\frac{\mu^2}{16} - \frac{1}{8} \right) \quad (5.13)$$

These are then substituted back into the Fourier Series (eqn 5.2b) and evaluated for $\psi = 0 - 2\pi i$.

The actual execution of the Fourier series is straight forward, as it all it requires is an evaluation of the series with respect to ψ . It must be noted that the Fourier Series solution is that of the steady state and that a single revolution is sufficient.

Once either solution is evaluated the inflow angle and the effective angle of attack can be found. The inflow angle ϕ is the angle as a result of the velocity components tangential and perpendicular to the velocity.

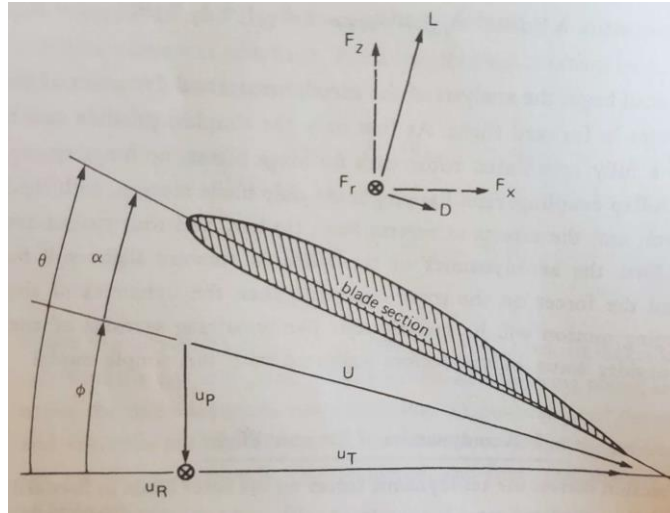


Figure 5.9 Relationship between pitch angle, inflow angle, and angle of attack[13].

As shown in figure 5.9, the effective angle of attack is found with $\alpha = \theta - \phi$, where

$$\phi = \tan^{-1} \frac{u_p}{u_T} \quad (5.14a)$$

With small angle approximations,

$$\phi \approx \frac{u_p}{u_T}. \quad (5.14b)$$

5.3 Results of flapping motion

Now, with the appropriate physics worked out, an evaluation can be executed. A Matlab script was written to evaluate the both the Fourier series solution as well as the differential solution. For the purposes of this analysis, the primary method for manipulating solutions will be the differential solution.

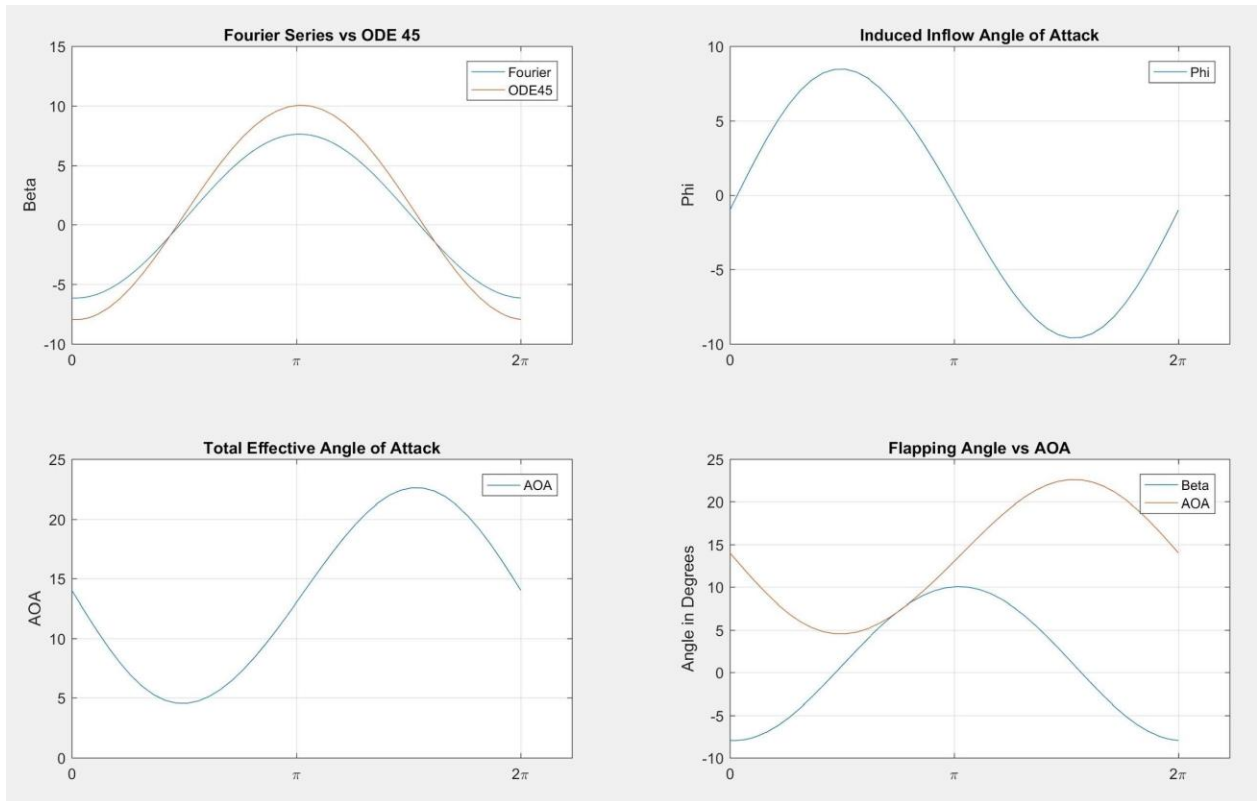


Figure 5.10 a) Fourier vs ODE45, b) Induced inflow Angle of Attack, c) Effective Angle of Attack, d) Flapping Angle vs Effective AOA

5.4 Benchmarks

In order to evaluate the accuracy of the results, it is necessary to compare them against other published works so as to validate the findings of the analysis. Majhi and Ganguli[20] perform an analysis that includes evaluating the flapping response as well as the induced inflow angle and the effective angle of attack under dynamic stall conditions.

The conditions for the benchmark include:

$$\mu \approx 0.3$$

$$\theta_0 = 13^\circ$$

$$\theta_{1c} = 0^\circ$$

$$\theta_{1s} = 0^\circ$$

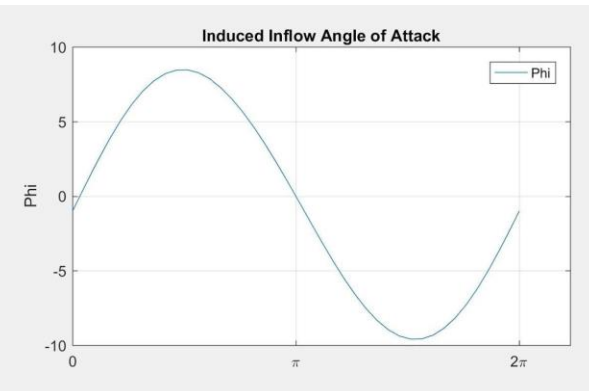
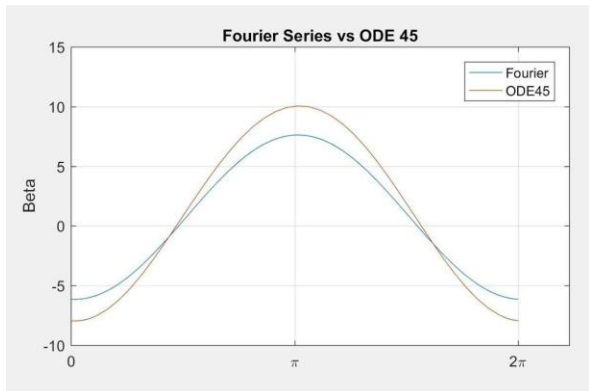
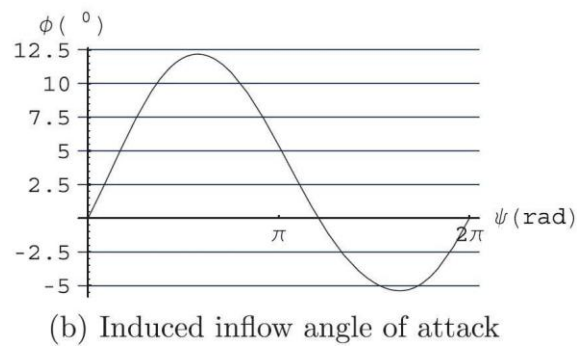
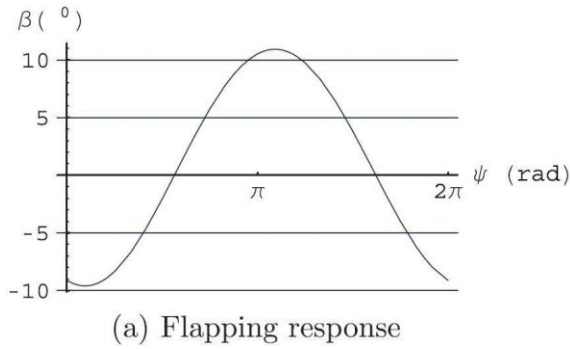


Figure 5.11 Benchmark response [20] vs calculated response

It can be observed that the results are fairly similar in their manifestations with a difference in several degrees of flap. This is believed to be largely due to the dynamic stall modelling that is utilized by Majhi and Ganguli which manipulates the coefficient of lift for sections of the rotation that achieve a higher than critical AOA.

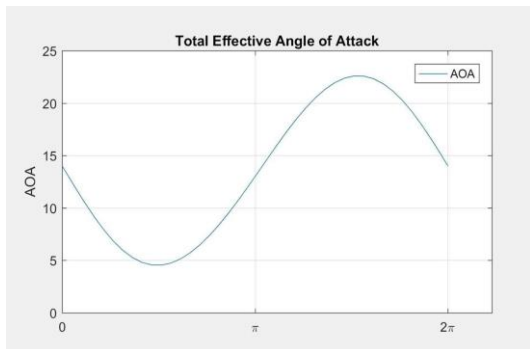
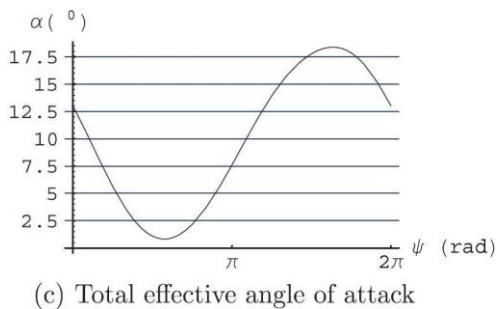


Figure 5.12 Comparing benchmark Effective AOA [20] with calculated AOA

Dynamic stalling can occur in the rotation, however, unlike a static stall, dynamic stall occurs quickly enough that the stall does not have time to physically affect the system to a high degree.

For practical purposes, a dynamic stall will result in a lowering of the coefficient of lift to a small degree and is not an issue as long it is not allowed to develop too far. Figure 5.11 and 5.12 show good agreement between published works and the calculated analysis. This confirms the validity of the methodology and it will be used to continue the analysis in the next section.

Chapter 6 Flapping Analysis

6.0 Flapping Analysis of the flapping hinge

In the previous chapters, the theory and derivations were developed in order to provide the foundation for an effective analysis. A Matlab script was written so that an initial analysis could be performed and compared against benchmark data to serve as a validation of the methods and models used. With a successful validation of the methodology, it is now possible to perform simulations of varying parameters for predictive behaviors of the rotor dynamics.

In order to stay relevant with the current development of real world aircraft, a comparison will be made utilizing parameters that represent specific airframe and mission requirements. Boeing and Sikorsky (Lockheed) have partnered to develop a suitable replacement for the UH-60 Blackhawk. The aircraft that has been prototyped as a technology demonstrator for such a task is currently known as the SB>1 (figure 6.1). The technology utilized by the SB>1 is based and derived from the development of the S-97 Raider (figure 6.2), which has been mentioned several times throughout the course of this study.

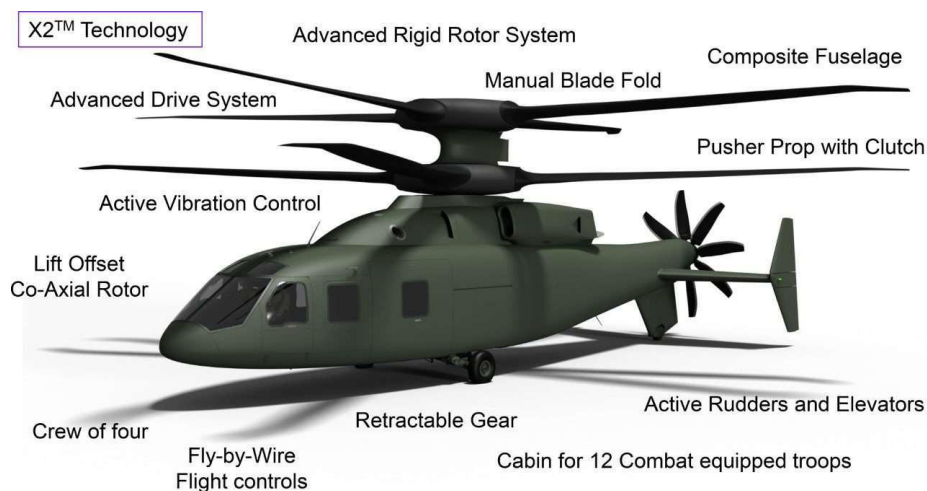


Figure 6.1 SB>1 Defiant Technology Demonstrator. Photo courtesy of LockheedMartin.com[21].

The S-97 Raider is also a technology demonstrator whose design intent is to provide the same capabilities as the SB>1 on a smaller scale to fulfill mission requirements previously performed by the US Army's OH-58 Kiowa.

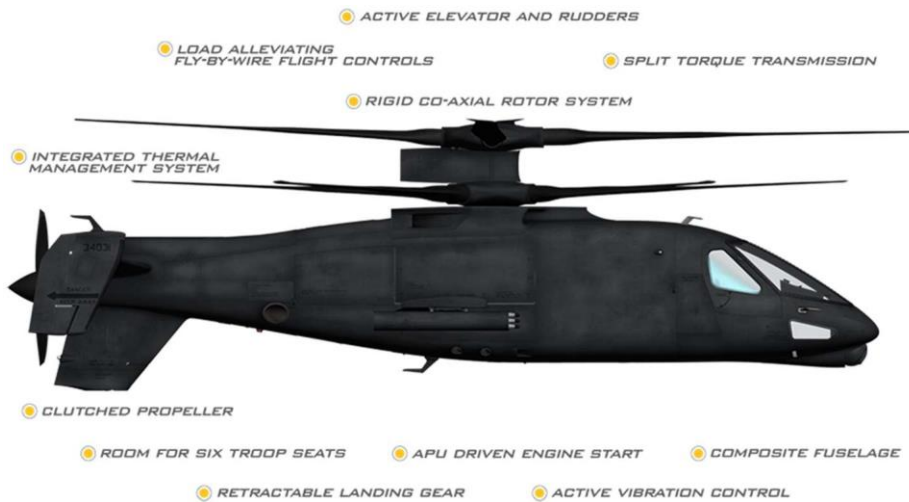


Figure 6.2 S-97 Raider Demonstrator. Courtesy of LockheedMartin.com [22]

Both aircraft are still in their proof-of-concept testing phase. Presumably, the details on both projects are largely classified. However, some parameters can be extrapolated based on what little information has been released to the public and on what aircraft they are intended to replace. This analysis will focus primarily on the SB>1, which is designed to replace the UH-60. Any unknown parameters will be filled by taking the UH-60 equivalent.

Table 6.1. Provides the relevant parameters and flight conditions for the analysis. All data contained in the table comes from the UH-60, with the exception of the maximum speed. A speed of 126 m/s (244 kt) far exceeds the capabilities of any helicopter in the world currently flying. That particular velocity is the target speed of the SB>1 and will be made possible by the innovative design characteristics of the airframe. As of the writing of this report, the SB>1 was still in testing and had not yet established a maximum speed. The S-97 is further along in the testing process and, as of this writing, had reached a speed of 102.8 m/s (199 kt) with greater speeds anticipated as testing progresses.

Table 6.1

Parameters						
V_{Cruise}	V_{Max}	Blade Span	Chord	Flapping Inertia, I_b	Airfoil	Coefficient of lift slope
78 m/s	126 m/s	8.18 m	0.527 m	20726 kg m^2	SC1094R8	0.1 1/deg

The analysis is greatly simplified if a singular distance along the span is evaluated and the flapping angle β is utilized for the whole span. Figure 6.3 shows the plot of the resulting angle of attack, per the benchmark conditions, along the span. The span was divided into 30 sections, ranging from 30 - 90 percent of the span. The low end of the range of 30 percent was chosen to avoid the reverse flow regions of the rotor disk. The upper range, 90 percent, was chosen because there are lift loss at the tip of the rotor blades, and evaluating the flapping based on the rotor tip would not yield results with an accurate enough degree.

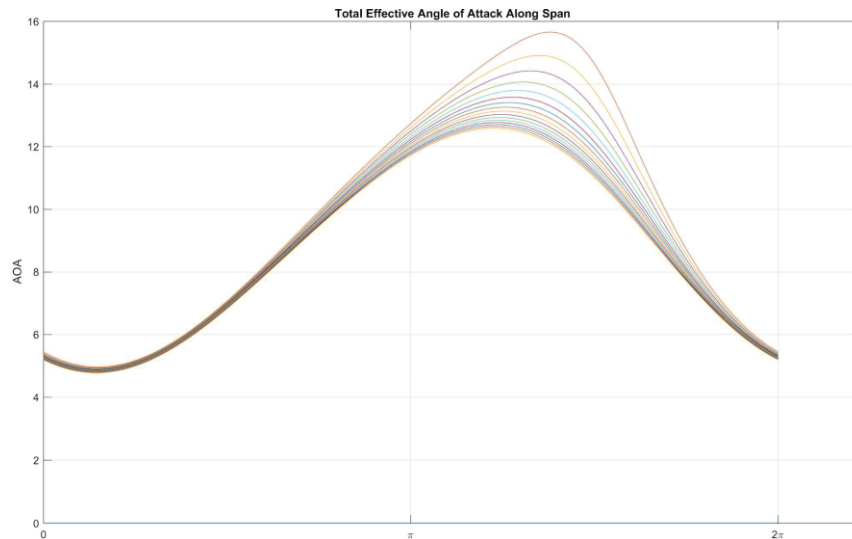


Figure 6.3 A plot of the angle of attack distribution along span from 30-90 percent of span

It can be observed from figure 6.3 that, with the exception of the sections that are closer to the root of the blade, depicted by the less consistent plots on the top side of the wave, the angle of attack at each span section is fairly consistent. There can be seen the variation in AOA is only a couple of degrees along the span. Following this observation, the distance of 75 percent of the span was chosen, and the corresponding flapping angles were utilized for the evaluation of the flapping.

6.0.1 Flapping Analysis of Hinged Rotor Blade

The first several analyses will be conducted within the context of the hinged flapping blade. It will be assumed that the flapping hinge is located at the shaft, which will mean that there is zero moment generated by the flapping. Figure 6.4 illustrates the nature of the flapping hinge. Note that where the figure states “flapping hinge” is where the shaft is assumed to be. The advantages to the hinged rotor blade is the simplicity in design and its light weight. From the standpoint of flying qualities, the hinged blades are able to absorb most perturbations with little dynamic response at the cost of sensitivity.

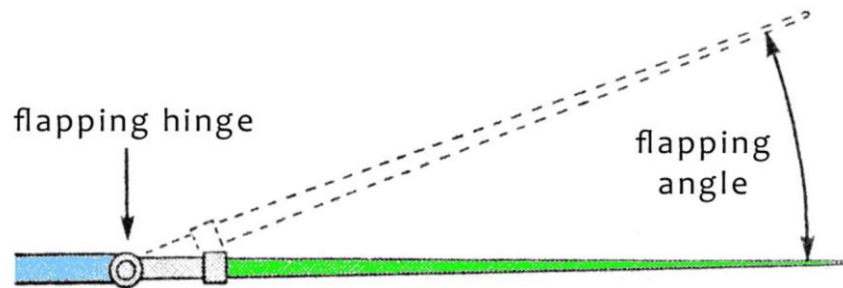


Figure 6.4 Illustration of a hinged flapping blade [23]

6.0.2 Flapping Analysis of Hingeless Blade

Hingeless rotor blades, shown in figure 6.5, manifest their flapping in physical bending of the rotor blade. This results in a moment being imparted onto the rotor hub. The flying characteristics are manifested in higher sensitivity and greater amounts of control. It also reduces the degree to which flapping can occur, which means a hingeless system can be pushed further than its hinged counterpart. Disadvantages include a lesser ability to absorb perturbation, such as turbulence, and added weight due to the needed strength. The S-97 and SB>1 both are touted to have rotor systems with rigid blades. It is probable that the rigidity of those airframes far exceed that of typical hingeless blade helicopters. However, for the time being, a hingeless system will be evaluated as though it is standard in nature.

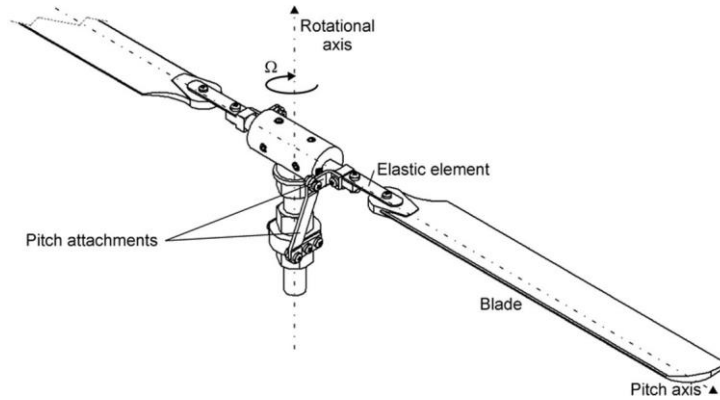


Figure 6.5. Illustration of hingeless rotor system. Image courtesy of researchgate.com

In order to evaluate the hingeless dynamics, the equations of motion that have already been developed must be altered slightly. It is possible to evaluate hingeless rotors as articulated blades with a hinge-offset as long as the flapping frequency found in the EOM's are adequately high enough. The EOM's are as follows:

$$\ddot{\beta} + \nu^2 \beta = \gamma \int_0^1 \eta \frac{F_z}{C_{l\alpha}} dr \quad (6.1)$$

Where,

$$\eta = \frac{r - e}{1 - e} \quad (6.2)$$

The variable 'e' is simply the percent offset of the rotor hinge from the rotor shaft. Typically, that percentage is about 10% or $e = 0.1$.

For the flapping frequency, η , typical values are $\eta = 1.10-1.15$ [13].

6.1 Hinged Rotor Flapping Analysis

The flight conditions for the first analysis will take place in a straight and level flight regime so as to simulate the pusher prop abilities of the S-97 and SB>1.

Figure 6.6 provides insight that has been previously discussed, as well as indications as to the severity of the asymmetric lift distribution. There can be no doubt that at any condition other than hover with no wind, an asymmetric distribution will develop due to the rotational nature of the rotor blade. This case, with 1 degree of collective input at cruising velocity is certainly no different. However, the severity, or magnitude of the responses are quite small. With less than a 2 degree total blade deflection, the effective angle of attack that results is also less than two

degrees. In this instance, there appears to be a possible correlation between blade deflection and effective angle of attack.

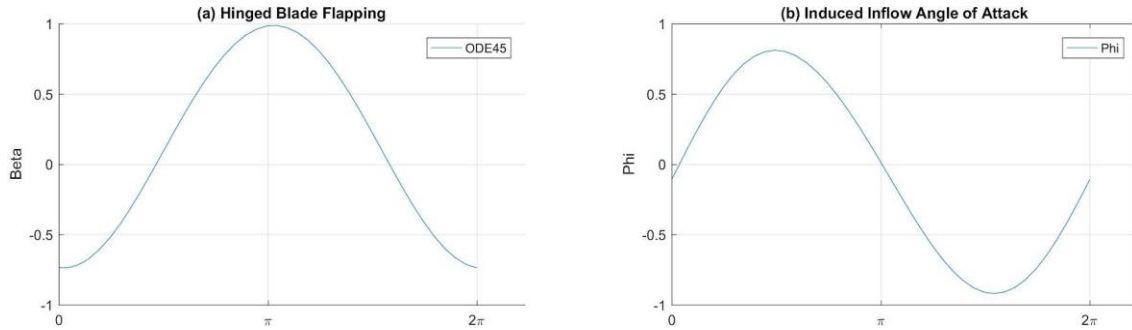


Figure 6.6 (a-b) Hinged rotor with 6 degrees of collective at 78 m/s

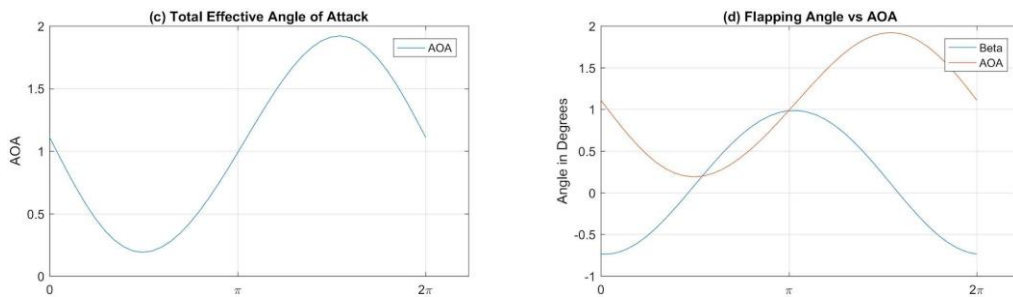


Figure 6.6 (c-d) Hinged rotor with 6 degrees of collective at 78 m/s

Figure 6.7 continues the trend of blade flapping appearing to be proportional to the effective angle of attack. Again, at cruise velocity but with 8 degrees of collective input, these conditions generate a response that takes the airfoil to the limits of its lift generating angles of attack. Other than detecting what appears to be the maximum control input for this particular flight regime, there is little detail of significance that is not already suspected. The sinusoidal nature that is typical is found here, as well as the 90 degree phase lag that is expected with respect to the flapping angle and AOA.

However, what is noteworthy is the small range of collective inputs that provide an AOA that stays both above zero and below the critical AOA.

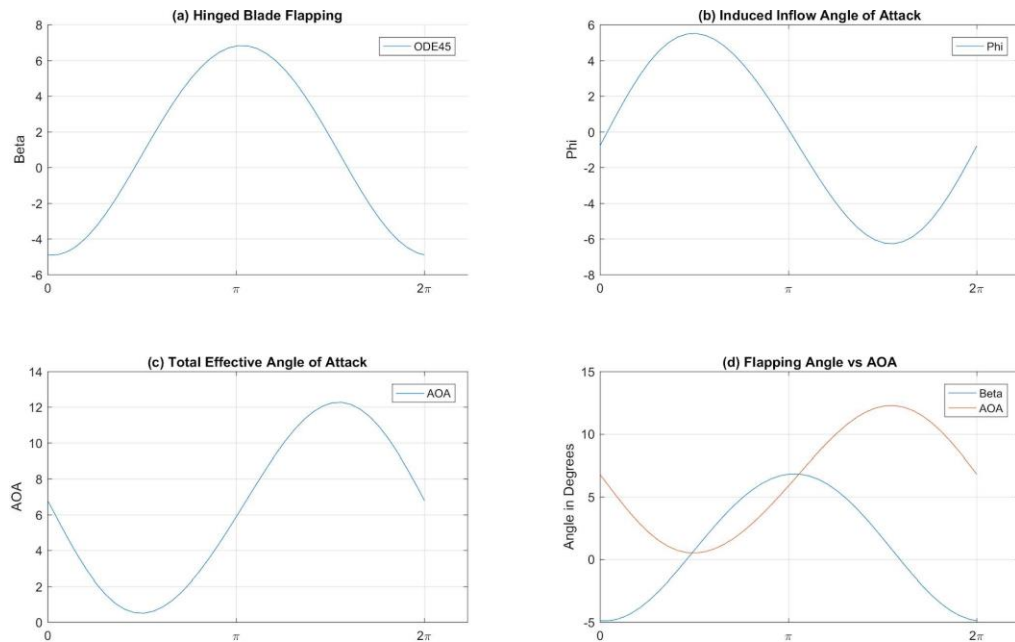


Figure 6.7 Hinged rotor with 8 degrees of collective, at 78 m/s

Figure 6.8, maintains the same parameters, however, the cyclic input has been set at -4 degrees, which results in a nose down attitude. This flight condition is approximated to simulate the rotorcraft flying as a standard helicopter would, so a 4-degree tilt in the rotor disk, to correspond with the -4 degree control input, has been implemented into the model.

Implementing a 4-degree tilt in the disk dramatically changes the dynamics response of the blade, particularly when evaluated with the flapping/AOA proportionality. Approximately 4 degrees of flapping result in an AOA range of 12 degrees.

This is also the first graph where the flapping angles and the induced AOA angles do not intersect at any time. While that is not necessarily significant physically, it does show that a cyclic input has the effect of shifting up, or transforming, the angle of attack distribution to achieve greater angles.

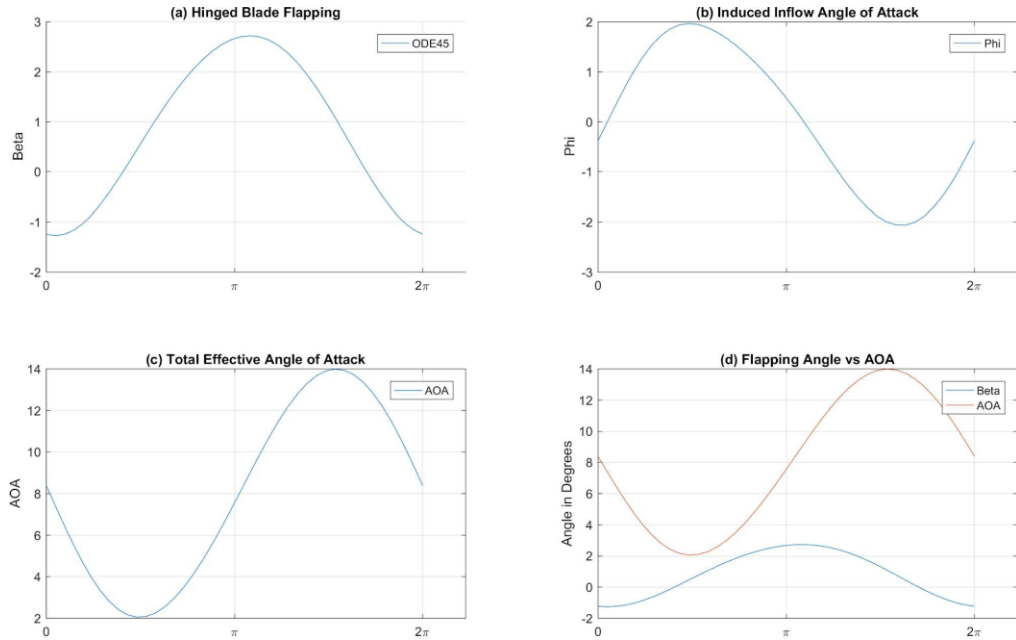


Figure 6.8 Hinged rotor with 8 degrees collective, -4 degrees pitch cyclic (nose down), at 78 m/s

The following evaluations for the hinged rotor blade will be taken with a velocity of 128.6 m/s, which corresponds to the intended maximum forward velocity of the SB>1.

Figure 6.9 shows that the minimum controllable collective input is 1 degree. Aside from that now determined boundary layer, dynamic response is as expected, with a proportional flapping/AOA angles.

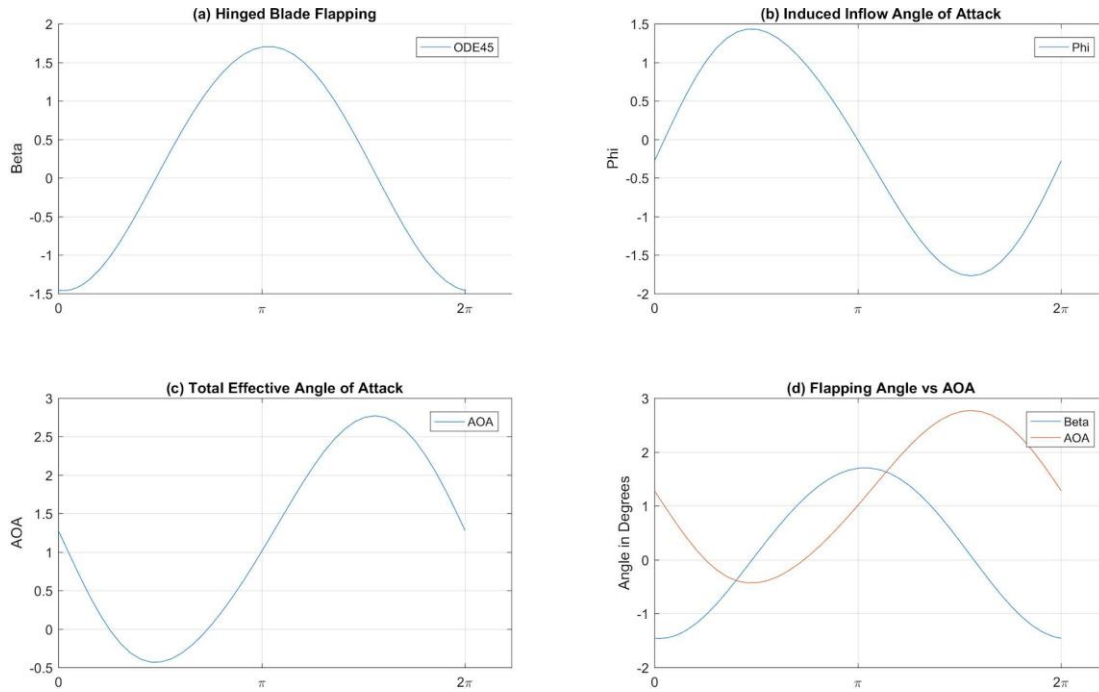


Figure 6.9 Hinged rotor with 1 degrees of collective at 128.6 m/s

Figure 6.10 shows a significantly higher set of angles for a collective input of 5 degrees, which is expected for this flight regime. It would be expected that for forward velocities of this magnitude that a lower angle of attack would be desirable in order to reduce drag.

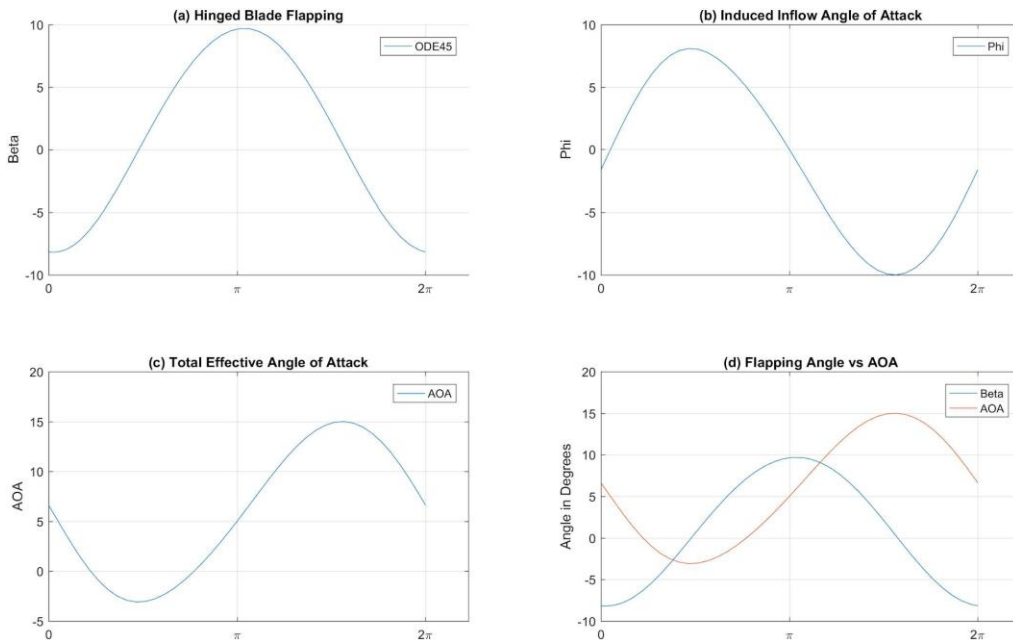


Figure 6.10 Hinged rotor with 5 degrees of collective at 128.6 m/s

6.2 Flapping Analysis of Hingeless Blade

6.2.1 Comparison Against the Benchmark Case

In the previous chapter, the method of analysis for hinged flapping was compared against benchmark evaluations and found to be in good agreement. By way of a comparison between hinged and hingeless flapping, figure 6.11 demonstrates the discrepancy between the flapping types.

Careful scrutiny of figure 6.11 shows, qualitatively, the difference in the phase lag related to the application of force on the disk and the response of the aircraft. As it is commonly understood amongst helicopter pilots, engineers, and helicopter enthusiasts alike, the hinged model demonstrates a 90-degree offset. The peak of the hinged AOA occurs at the 270-degree position. The peak of the flapping occurs at the 180-degree mark because it is that physical occurrence that prevents the rotor disk from continuing to precess in a forward pitching motion. These motions occur 90 degrees out of phase from each other.

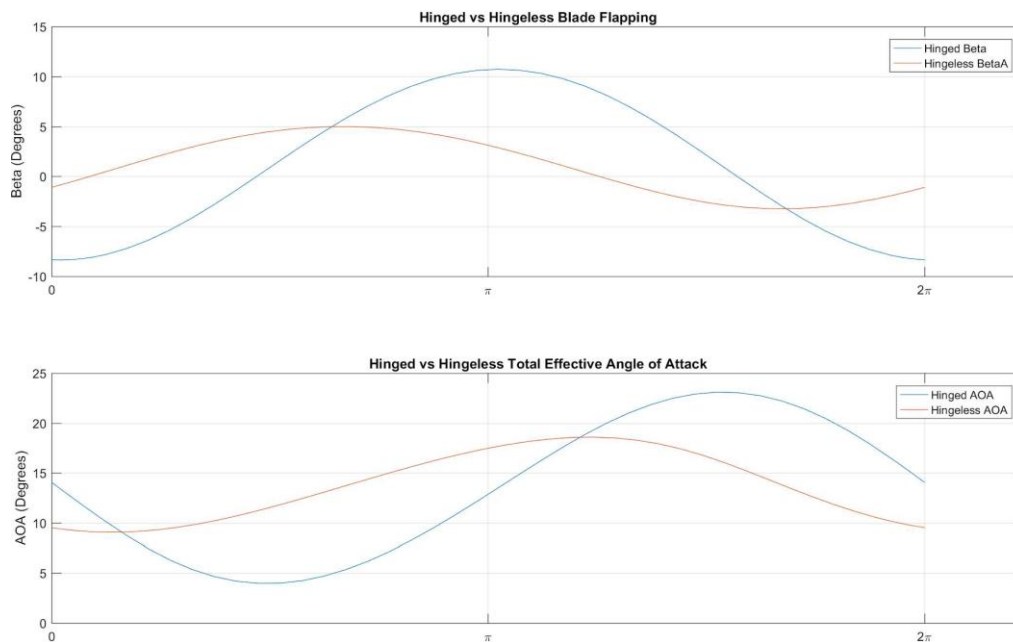


Figure 6.11 Comparison of Hinged vs. Hingeless under the benchmark conditions

By contrast, these same reactions on the hingeless blade occurs in a similar fashion, however, if the data points are examined closely, which was done for this analysis but not shown, then the phase shift is found to be 72 degrees. This is a characteristic of articulated blades with a hinge offset and hingeless blades which can be simulated as such. This is due to the flapping frequency being greater than 1/revolution for these types of rotors. The reason for this behavior is the lift

variation during blade transit, with increasing lift causing the blade to flap up. In a subsequent chapter, the analysis of the aircraft transitioning from hover to propelled straight and level flight will be examined to help further the understanding of the physical manifestations that occur in blade flapping.

6.2.2 Analysis of Hingeless Flapping in Various Conditions

The following figures demonstrate the flapping dynamics of hingeless blades. As in previous sections within this chapter, the models will be examined in multiple control-input states, while maintaining straight and level flight, for both cruise and maximum velocities.

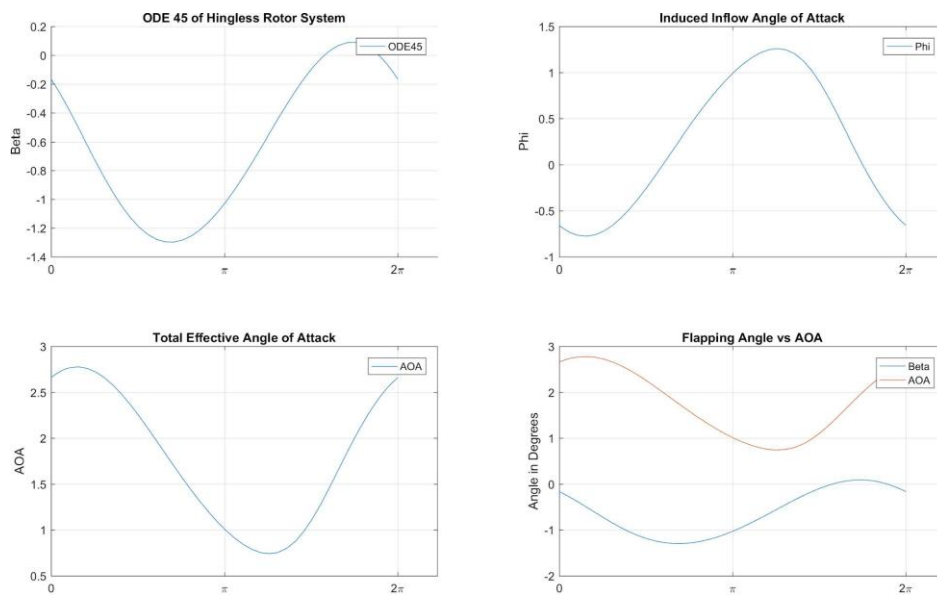


Figure 6.12 Hingeless rotor with 1-degree of collective at 78 m/s

Figure 6.12 shows the response with a collective input of 1 degree at a forward velocity of 78 m/s. At this velocity, this is the lowest collective value that can be held while maintaining a positive angle of attack. As previously mentioned, while the airfoil in question will still generate positive lift at -1 degrees AOA, for the sake of this analysis, only control inputs that result in positive angles of attack will be considered.

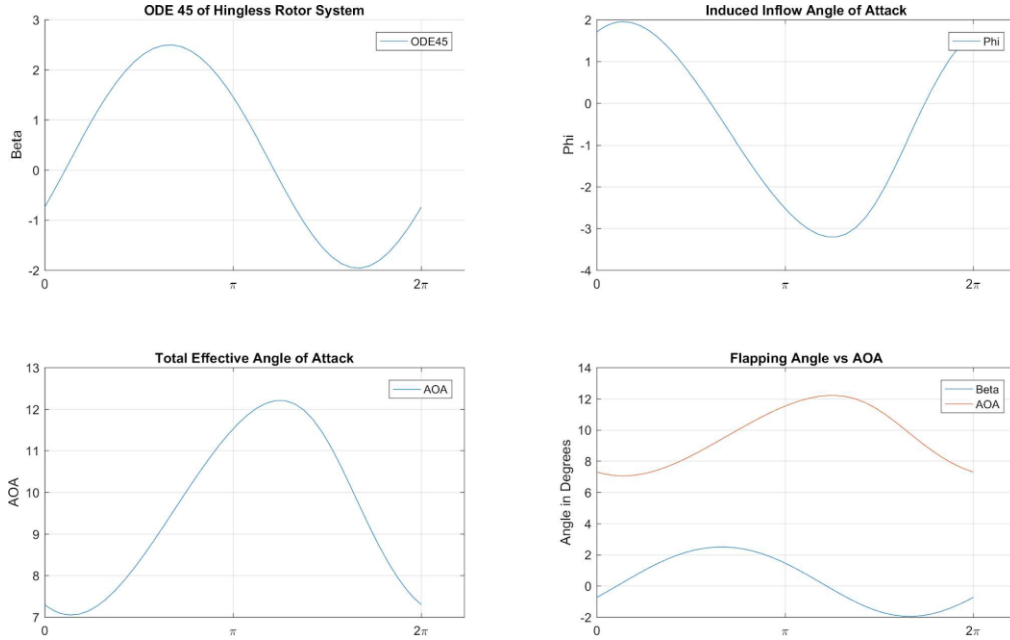


Figure 6.13 Hingeless rotor with 9 degrees of collective at 78 m/s

Figure 6.13 Shows a 9-degree collective input at cruise velocity. This value is the largest control input for this velocity that does not induce an AOA that exceeds the critical angle of attack. One of the characteristics that is most evident when in contrast to hinged blade are the flapping angles. Similar conditions for the hinged blades result in a flapping angle difference of 12 degrees from top flap to bottom flap. While this in this case, the flap difference is 4 degrees.

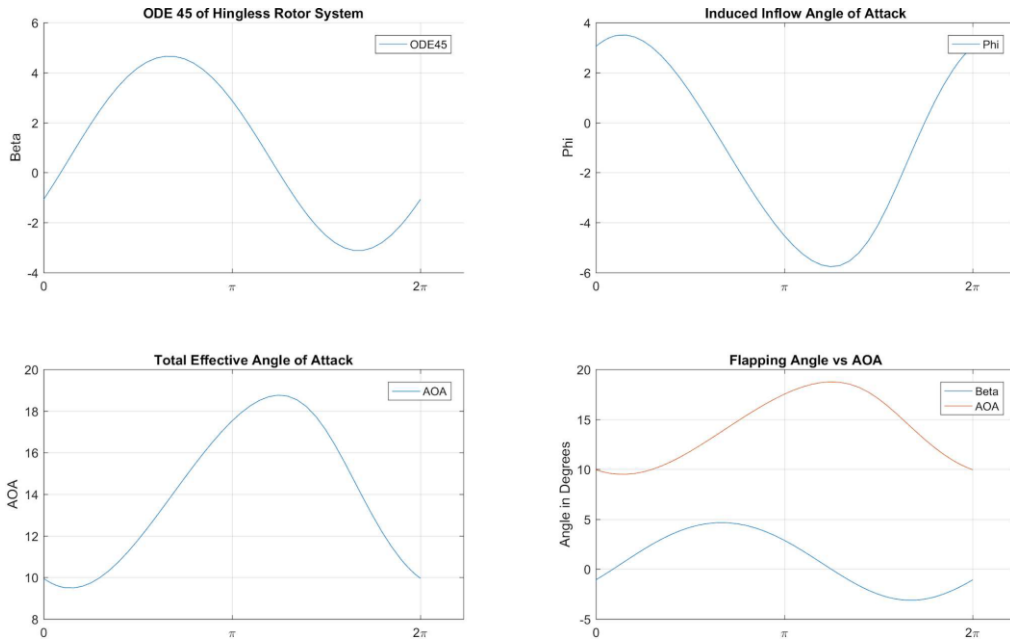


Figure 6.14 Hingeless rotor with 13 degrees of collective at 78 m/s

Figure 6.14. Shows the response for 13 degrees of collective. The induced angle of attack at its peak is between 18 and 19 degrees. The flapping angle β achieves negative values that correspond to the peak AOA. As with other hingeless examples, the angle at which the maxima and minima occur offset of the 90-degree increments.

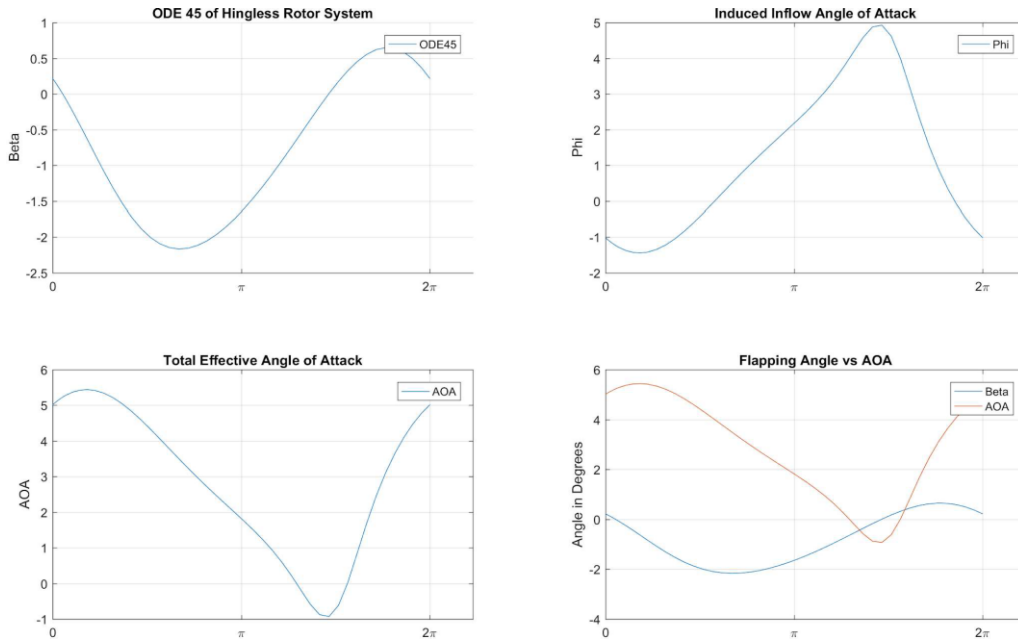


Figure 6.15 Hingeless rotor with 4 degrees of collective at 126 m/s

Figure 6.15 shows a 4-degree collective input at the maximum anticipated velocity of 126 m/s. This is the first case of hingeless flapping at this velocity that has been examined thus far. As demonstrated in figure 6.15, the response at this velocity is much more asymmetric and departs from the usual sinusoidal pattern that is common in slower flight regimes. This particular case is also inverted from other typical examples, where the flapping sees its highest positive value on the retreating side rather than the advancing side. Conversely, the AOA shows its highest positive value on the advancing side and lowest value on the retreating side. This is a very interesting response, because a vast majority of the lift is generated toward the rear of the disk. It's possible that this is an unstable manifestation.

Figure 6.16 Shows a higher collective input for the same maximum velocity. Unlike the previous figure, this response shows peaks in the typical regions of the rotation. The steep slope of the angle of attack indicates that the rate of change of the angle of attack with respect to the rotation is quite high. The prominent peak would indicate that that particular region of the disk requires a high degree of lift in order to balance out the forces and maintain the rotational frequency of the rotor blades.

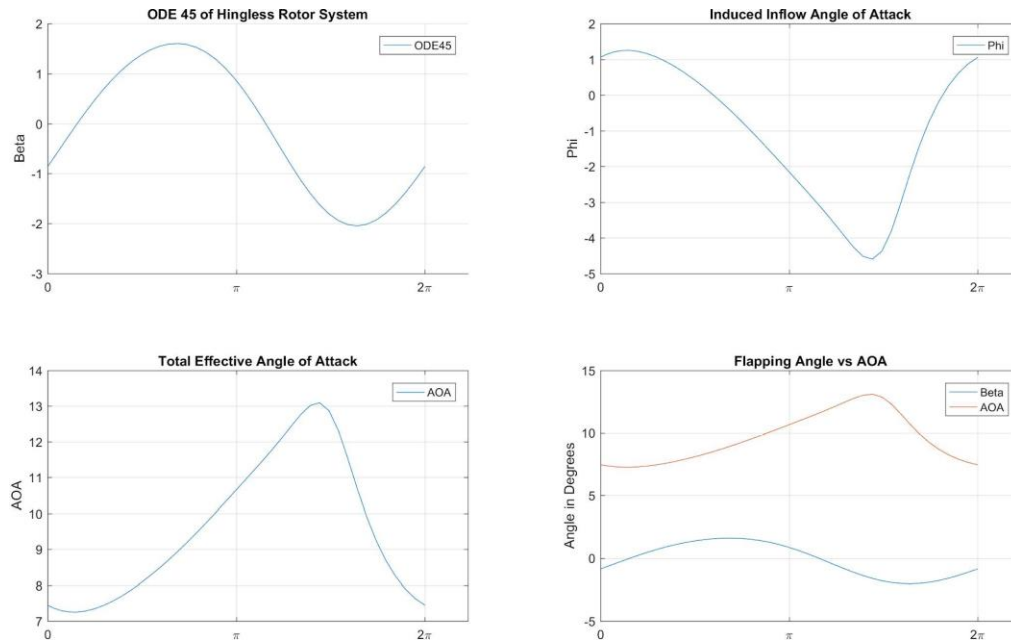


Figure 6.16 Hingeless rotor with 8.5 degrees of collective at 126 m/s

6.3 Conclusion

The goal of this analysis was to establish clearly defined limits of rotary wing controllability in a straight and level flight regime. The analysis provided a glimpse into the minimum and maximum limits of control input that result in minimum and maximum dynamic responses. The analysis is far from all encompassing, as it neglects several key aerodynamic occurrences that should not be ignored in the event that a true to life response is to be evaluated. However, it does provide a reasonable baseline from which to make predictions.

Common trends include the predictable sinusoidal motion of blade flapping and its corresponding angle of attack. Additionally, it was observed that there appears to be a direct proportionality in flap angle and angle of attack for hinged blades. The same cannot be said about hingeless as there is a clear distinction between the proportionality of hinged versus hingeless. In the case of the hingeless blades, the flapping angle range was dramatically less than that of the subsequent angle of attack.

Another distinction between the two systems are the phase lag of the flapping to the AOA, which directly corresponds to how the rotor disk is controlled. Hinged disks show a 90-degree phase lag, while hingeless show approximately 72 degrees.

Chapter 7 Evaluating Alternate Conditions

7.0 Taking Advantage of Having a Coaxial Rotor

The following assessment is completed by modelling the acceleration of the helicopter with respect to the revolutions of the blade. The purpose of this is to evaluate the dynamics from one velocity state to another. For example, from hover, a zero velocity condition, to cruise velocities. A crude approximation of velocity can be made, assuming an arbitrarily defined acceleration, with the following relationship:

$$V = at \tag{7.1}$$

Where,

V is the velocity of the aircraft, 'a' is its acceleration, and t is the elapsed time in seconds. The passage of time can be related to rotation rate as such:

$$\psi = \Omega t \tag{7.2a}$$

Solving for t,

$$t = \frac{\psi}{\Omega} \tag{7.2b}$$

This is easily substituted for time in order to approximate the velocity of the rotorcraft with respect to rotation angle for user defined parameters within the MATLAB script written for this analysis.

$$V = a \frac{\psi}{\Omega} \tag{7.3}$$

For the following transient analyses, the rotorcraft will be assigned to a flight regime. The initial conditions are always set to zero, so the transient behavior will require time to stabilize before it can be considered the baseline for the flight regime. Once that has been achieved, the input parameters will be changed and the response will be plotted to a substantial enough degree so that it gives some insight to the behavior of the system.

Figure 7.1 shows the response of a helicopter in a hover state. This initial transient response that makes up the first 10 revolutions is simply the model damping out to steady state from the initial conditions of zero. Beginning at revolution 16, the system began accelerating forward at 2 m/s so

that the target velocity of 20 m/s would be achieved in 10 seconds. The control input for this simulation is 7 degrees of collect with zero cyclic input. Figure 7.1 continues for an additional 30 revolutions and is truncated prior to demonstrating steady state.

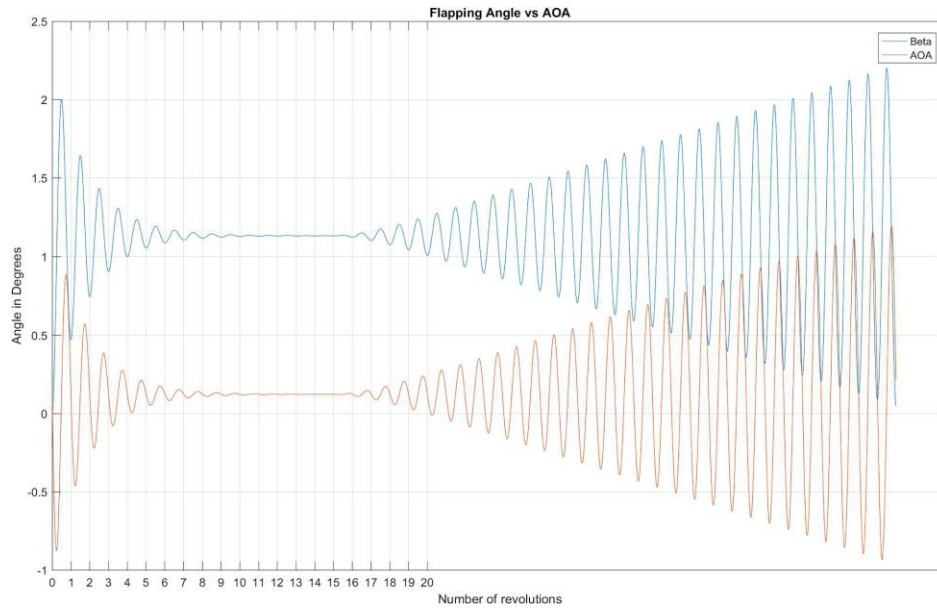


Figure 7.1 Transition from hover to 20 m/s at 7 degrees collective for 45 total revolutions

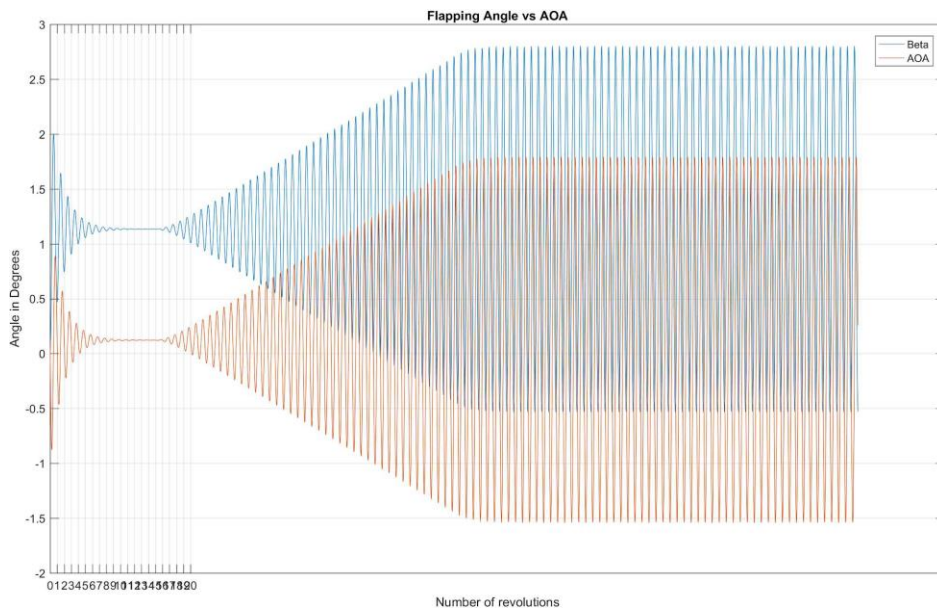


Figure 7.2. Same flight conditions as figure 7.1 with additional revolutions to include steady state

Figure 7.2 shows the same flight condition as figure 7.1, but it extends to steady state and includes 115 total revolutions. It can be seen that when the hover condition steadies out, the flapping angle and angle of attack remain constant until the acceleration begins. As the velocity increases, both the flapping angle and the AOA become more pronounced and effective. The adjustment of collective as velocity increases, as would occur in the real world, is not included.

7.1 Dynamic Response From Straight and Level to Nose Forward

Figure 7.3 demonstrates conditions that represent the transition from straight and level flight into nose forward flight. The practical application would be starting in a condition that is driven by the pusher prop and making a change where the rotor disk is pitched forward to simulate the standard flight characteristics of helicopter flight.

As with all of the cruise flight condition representations, figure 7.3 represents a flight regime of 73 meters per second. The initial conditions have been assigned to represent straight and level flight which includes no pitch to the rotor disk. The beginning of the figure assumes an instantaneous -4 degree cyclic pitch input and an instantaneous 4 degree nose down pitch of the rotor disk.

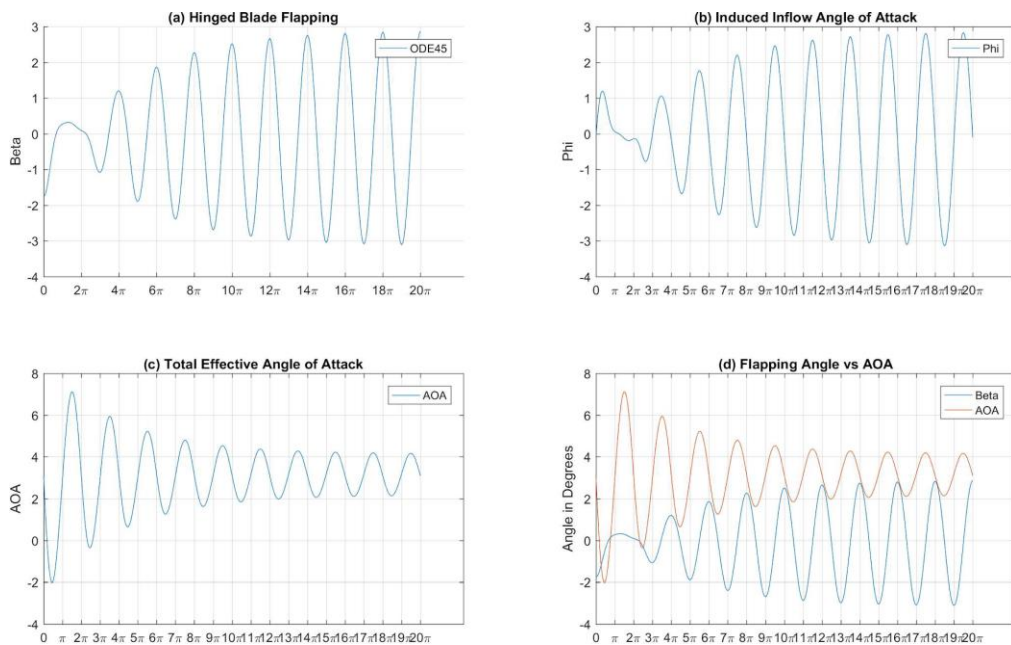


Figure 7.3 Cruise 78 m/s instant change to -4 degrees cyclic and 4 degrees nose down, collective 3 degrees

Figures 7.3 and 7.4 show how the transient state of the system differs from previous analyses. The transient state takes 6 full revolutions to reach steady-state. Close inspection of the flapping angle graph demonstrates the strong influence that the lift force has in forcing the flap motion.

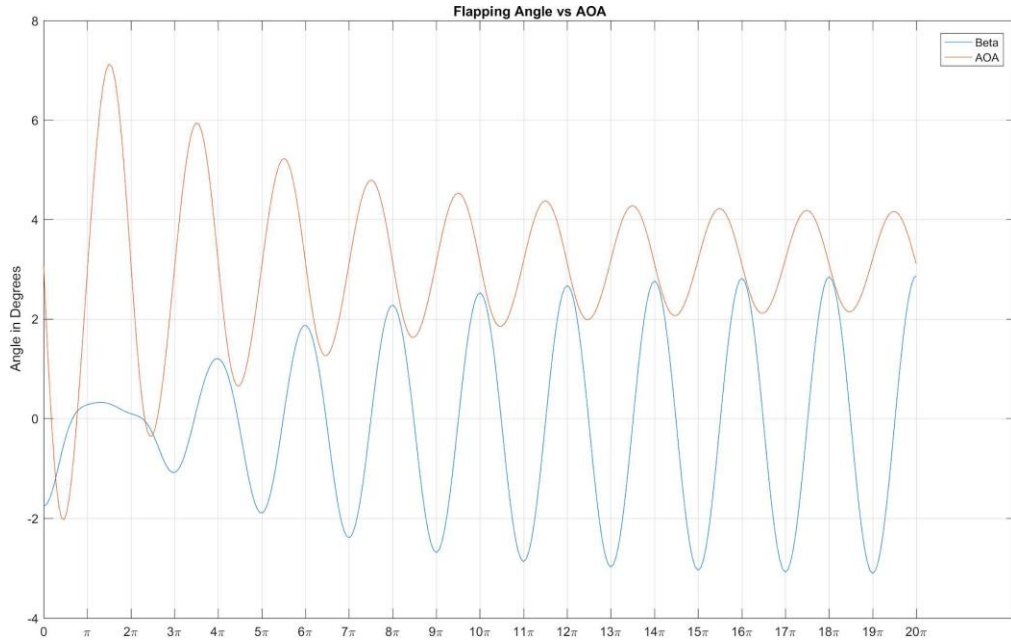


Figure 7.4 A close look at the angle of attack and flapping angle graph from figure 7.3

Figure 7.5 represents a flight condition that begins at 78 m/s forward velocity with an 8-degree nose down attitude, 10 degrees of collective input and 8 degrees forward cyclic. The first four revolutions represent the transient state from initial conditions of zero and should be neglected. After the 1st regime has reached steady state, and condition change is induced. The second condition is an instantaneous change to a straight and level attitude, 12 degrees collective input, and zero degrees of cyclic. The point of interest is the response which takes place after the 10th revolution.

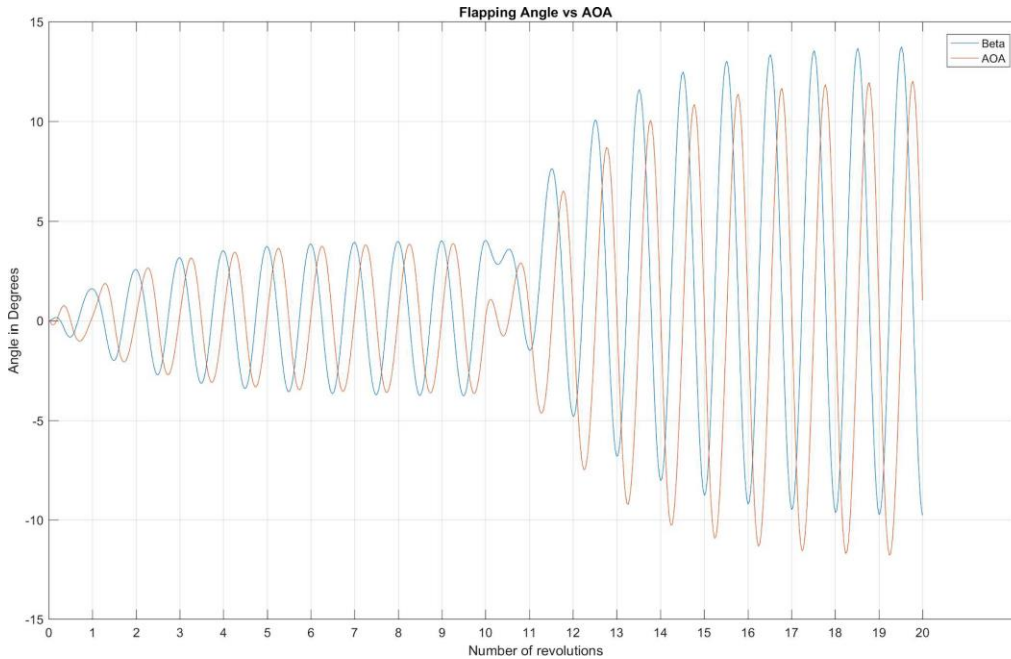


Figure 7.5 The change in flapping angle and AOA as flight conditions change

As can be seen in the above figure (7.5), the revolution at which the control inputs are changed there is a clear disturbance in the trend as the blade adapts to the new conditions. Just short of the 180-degree mark in the rotation, the AOA rapidly increases before decreasing dramatically. It can also be noted that the point in the rotation that the maxima and minima of the AOA occurs in different phases. For example, peak AOA prior to the input change takes place around the 90-degree position. By contrast, after the control change, the peak of the AOA occurs closer to the 270-degree position.

While not strictly necessary for the purposes of this study, the above analyses should provide some insight into the motion and vehicular dynamics of the helicopter rotor blades helping to solidify an understanding of typical reactions and responses that should be expected from a helicopter.

Chapter 8 Evaluating The Coaxial-Pusher Configuration

8.0 Taking Advantage of Having a Coaxial Rotor

So far in this study, the rotor flapping dynamics have been evaluated on an individual basis in both conventional helicopter configurations as well as with a coaxial pusher configuration in mind. However, little consideration has been taken into accounting for optimization. Thus far, the modelling has been approached from the vantage point of simply adding a pusher-propeller to a helicopter allowing it to propel itself forward without requiring a tilt in the rotor disk. This was a necessary approach because the insight into flapping dynamics in that configuration aids in understanding the approach to optimizing a design. Moving forward, a focus on how the new family of coaxial helicopter is most likely designed will be evaluated.

The technology that the S-97 and SB>1 are based on a technology demonstrator known as the X2. Unconfirmed sources on the portal to information, the internet, have suggested that the X2 design achieves its speed goals in several ways that are fundamentally simple. The design characteristic that is the most impactful involves leveraging the ability to share the symmetric loading across both sets of rotor blades. As has been observed in the analyses in the previous sections, it has been seen that in order to compensate for the dissymmetry of lift caused by the variation in velocity about the disk, the blade flaps which results in an increase of the angle of attack on the retreating side. This increase of angle of attack directly translates to an increase in lift so the lifting force across the disk is balanced. However, this increase in angle of attack also increases drag. The most profound problem that this creates is that the increase in drag must be overcome by the engine of the aircraft. The effects are probably a non-issue in ideal operating conditions. However, when considering high-speed flight at high altitude with hot temperatures, then the drag penalty becomes far more severe. One of the engineering techniques that is used to overcome this problem is to create a system that allows the retreating blade to experience a lower angle of attack. The obvious advantage to the coaxial design is that the two rotor disks maintain the symmetry of lift.

Recall how a helicopter control system works: the collective is the control input that adjusts the angle of the all of the blades simultaneously. The cyclic is the control input that provides directional control. It does this by tilting the swashplate in the direction of travel so as to cause the rotor blades to change pitch, periodically or cyclically, as they rotate about the shaft. Also recall the 90 degree offset of applied force and vehicle response. In order to induce the helicopter to propel itself forward, a force is applied at the 270 degree radial and the response occurs 90 degrees later at the 0/360 degree radial, rotating the helicopter forward until equilibrium is established. This remains the same for a helicopter with a coaxial rotor system. The two rotor disks are counter-rotating, so for the sake of simplicity, rotor disk number 1 will be defined as having a rotational coordinate system that is conventional with zero degrees pointing toward the back of the aircraft and a counter-clockwise rotation. Rotor disk number 2 will be inverted in

such a way that 0 and 180 degrees match disk number 1, but is rotating clockwise, so that the 270 degree radial is located on the starboard (right) side and the 90 degree radial on the port (left) side. Figure 8.1 illustrates this point. The rotating reference frames have been defined this way so that regardless of which disk is being referred to, 0-180 degrees is always the advancing side and 180-360 degrees is always the retreating side.

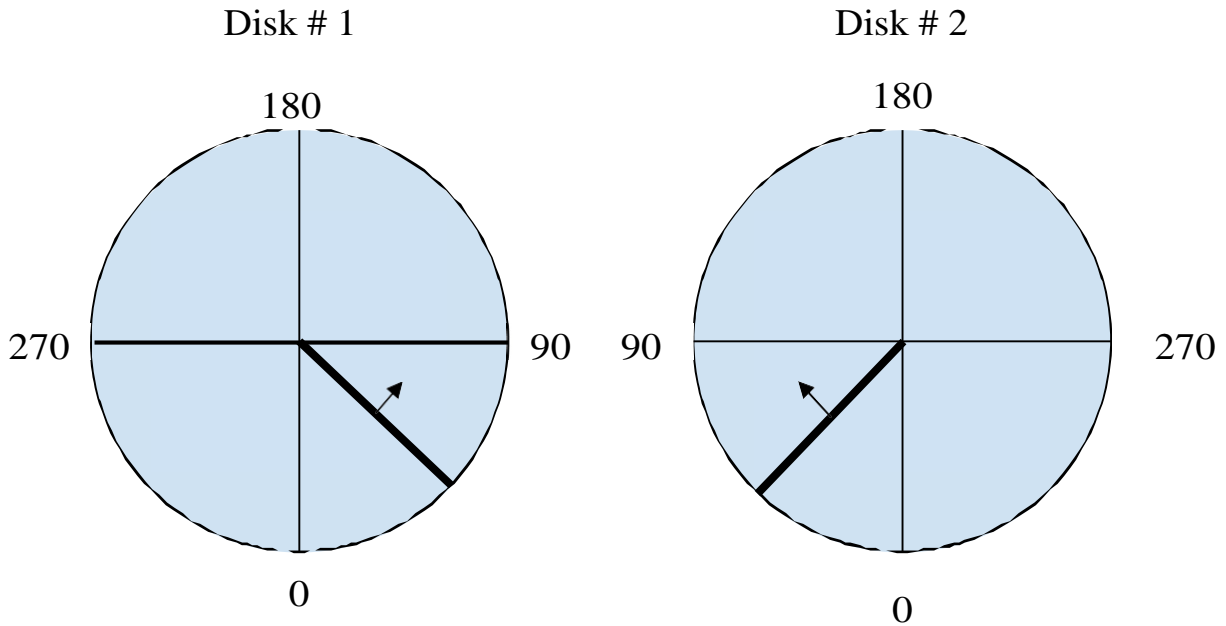


Figure 8.1 Radial reference frames to disk one and disk two for a coaxial system

Figure 8.2 demonstrates how a force applied to the respective disks 270 degree radial will result in the same rotation response. An implication of this is that a lesser degree of actual control output will induce that vehicle response on a coaxial system versus a conventional system. If the two disks were to be examined on the airframe itself from above, then the two images from the figures would be superimposed to create a disk planform area. The illustration demonstrates that controlling a coaxial helicopter requires that the applied forces on the respective disks be applied opposite each other when viewed on the superimposed planform.

The previous explanations show how a standard coaxial helicopter is controlled. However, the X2 concept most likely utilizes a separate control scheme in order to achieve its designed intent. Recall that the one of the design goals was to minimize the angle of attack, and thus the drag, on the retreating blade. This can be achieved with a cyclical-only control input for generating lift.

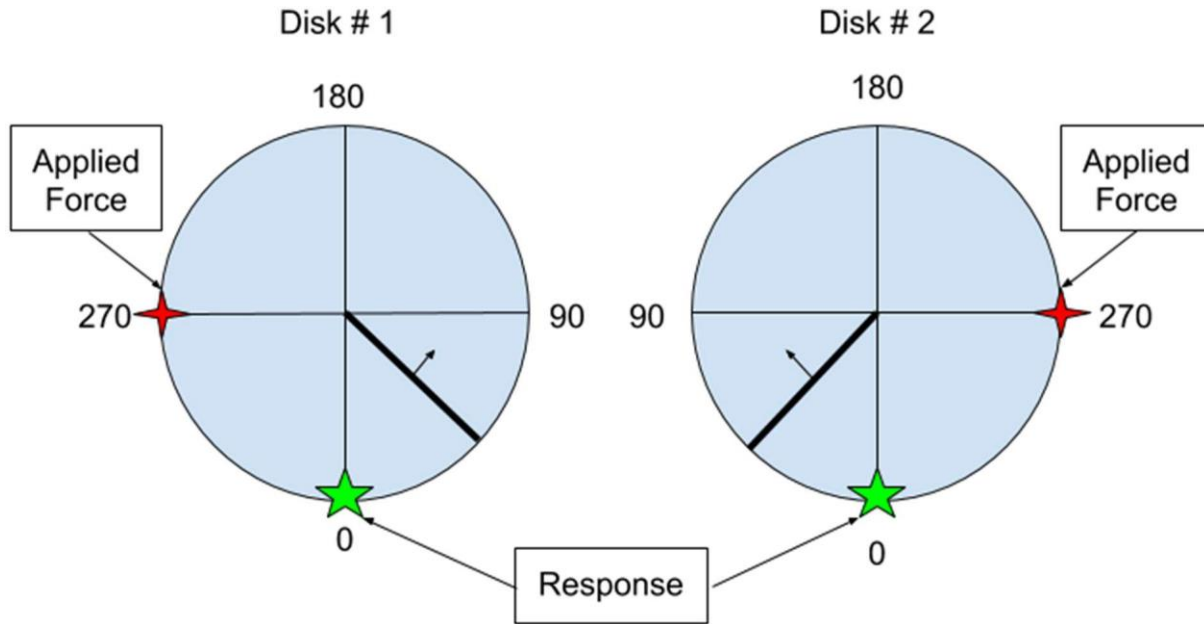


Figure 8.2. Illustration of how a lift applied to respective 270-degree radials result in same response

A cyclical-only control scheme for lift generation has unconventional implications for how the rotorcraft will be controlled. Again, on a standard helicopter, the AOA needs to be the highest on the retreating blade to compensate for the symmetry of lift. However, if we do not care about the retreating side, then the focus will be on the advancing side. It was critical for the single rotor helicopter that the cyclic control input induce the lift at 270 degrees so that the aircraft could be precessed forward. However, in the case of the coaxial-pusher that is to remain straight and level, the cyclic inputs need to be applied in such a way that increases angle of attack on the advancing side, decreases angle of attack on the retreating side, while not pitching/rolling the aircraft in any way.

Figure 8.3 demonstrates how this can be done in a fairly simple way. In order to achieve the aforementioned criteria, the applied forces on each of the disks must be applied in line with each other. In other words, in order to generate additional lift and increase the blade incidence, the applied force must be applied to the 0-degree radial on both disk 1 and disk 2. The response of disk one will be to roll the aircraft to the port (left) side about the 0-180 degree axis. The response of disk two will be to roll the aircraft to the starboard (right) side. These two counteracting responses will cancel each other out allowing for precise control of where to maximize the angle of attack along the disks without exciting any pitching/rolling responses.

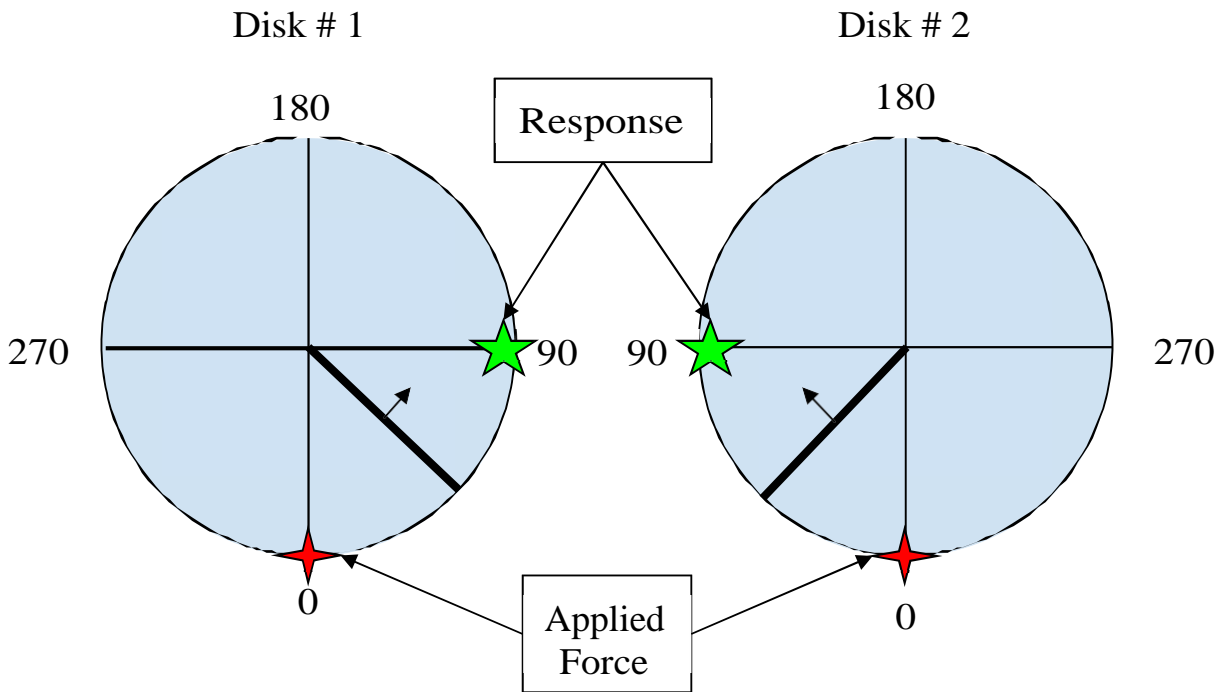


Figure 8.3. Illustration of counteracting dynamic responses

Before moving on to the analysis, there are a couple of items worth noting. First, if a pilot in a standard helicopter were to induce a left roll, it would require a left cyclic control input, and a right roll requires a right cyclic input. This means that in order to achieve the desired effect, the control equivalent would be a simultaneous left and right control input.

From the perspective of the swashplates, this means that both swashplates are pitched opposite each other, which is counter to how a standard coaxial helicopter operates. Standard coaxials require that both swashplates pitch in the same orientation to achieve the desired condition. Since that is not the case in the pusher configuration, the degree of complexity is much higher.

The fly-by-wire software used to control this system also needs to be sophisticated enough to handle the various flight conditions. In high speed flight, this opposing swashplate control is required and the aircraft is flown more like a fixed-wing aircraft. However, in lower speed flight regimes, the helicopter is flown and controlled just like a standard coaxial helicopter, and the connection between the control response and the control input needs to adapt and respond accordingly.

The explanation above assumes that there is a 90-degree phase offset, which corresponds to a hinged blade. This would be partially impractical and partially dangerous in reality and a

hingeless blade would be utilized. This will alter the cyclic input required to achieve the desired condition and will add a layer of complexity to the analysis.

Finally, the following analysis shows a single graph representing single blades of one of the disks. The reader is prompted to bear in mind that, for the purposes of this analysis, the dynamics response is simply a mirror image of the results shown here.

8.1 Analysis

Figure 8.4 displays the relationship between the aerodynamic coefficients and the angle of attack for the SC1094R8 rotorcraft airfoil. This is the airfoil that is used by the UH-60 Blackhawk, the aircraft that the SB>1 is replacing, which is why it was chosen to perform the analysis. It will be useful in showcasing the critical angles of attack as well as the corresponding coefficients of drag when necessary.

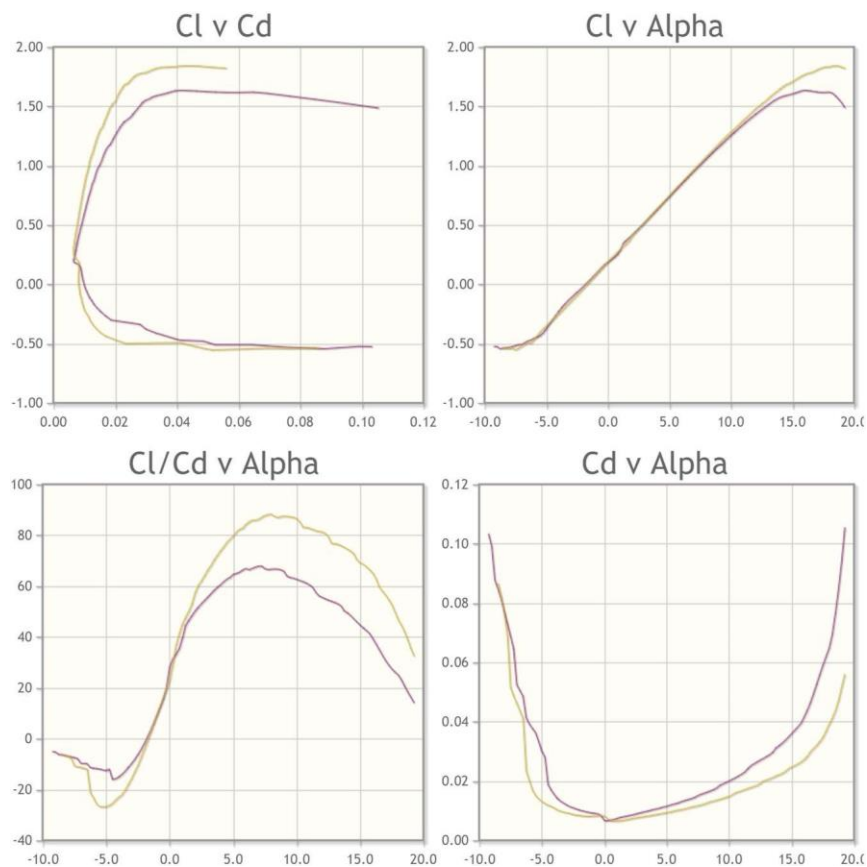


Figure 8.4 Lift and Drag Coefficients vs AOA [1]

Figure 8.5 shows the flapping angle and effective angle of attack for this analysis. Flight conditions take place at sea level at the cruise velocity of 78 meters per second. As previously

discussed, the collective and cyclic inputs are set to maximize the AOA on the advancing side without inducing a pitching moment on the airframe. In this condition, $\delta_0 = 8$ degrees, $\delta_{17} = 8$ degrees, and $\delta_{17} = 10$ degrees. These control inputs represent a flight condition that provides the maximum angle of attack, per figure 8.4, while maintaining low drag on the retreating blade.

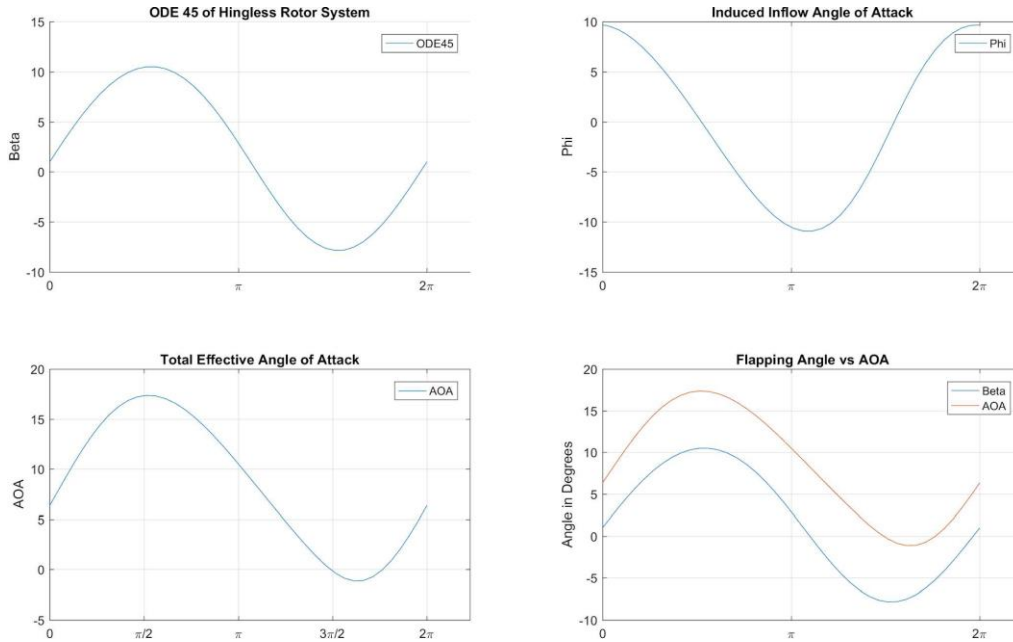


Figure 8.5. Velocity:78 m/s, Collective: 8 degrees, Equivalent cyclic roll: 8 degrees, cyclic pitch: 10 degrees, max AOA: 17 degrees, min. AOA: -1 degree

Note on the CL vs Alpha graph in figure 8.4 that the zero-lift angle of attack is approximately -2 degrees. This angle of attack corresponds to a low drag coefficient as well.

Figure 8.6 represents the same flight condition, that is maximum AOA with minimum drag, for a forward velocity of 126 meters per second. In this case, it was achieved by setting the control inputs to $\delta_0 = 8$ degrees, $\delta_{17} = 8$ degrees, and $\delta_{17} = 10$ degrees. In this instance, the minimum angle of attack lies on the zero-lift line, which again corresponds to maximum lift and minimum drag.

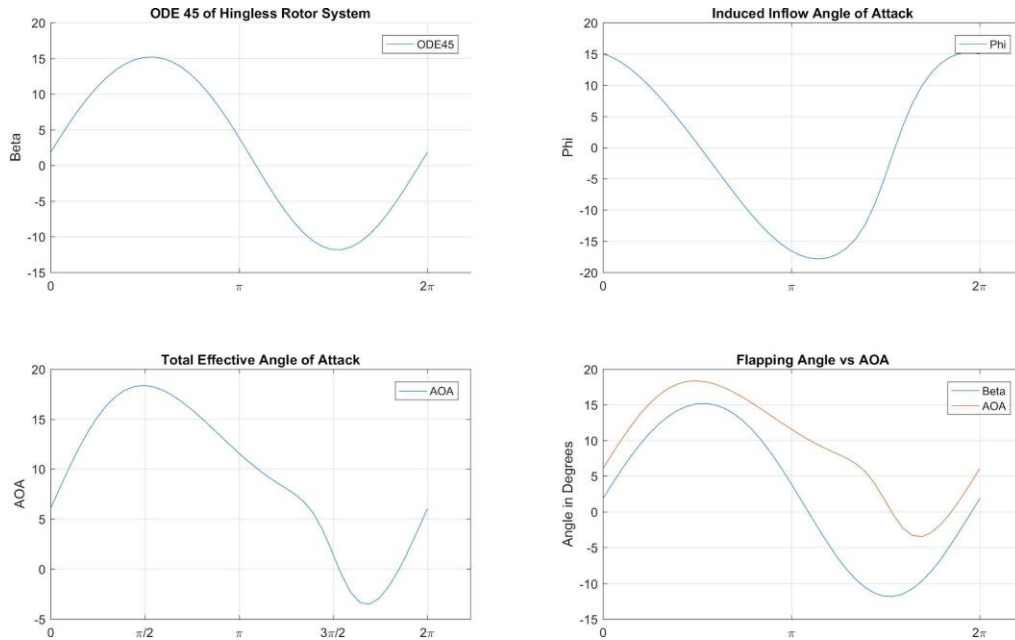


Figure 8.6. Velocity: 126 m/s, Collective: 8 degrees, Equivalent cyclic roll: 13 degrees, cyclic pitch: 11 degrees, max AOA: 18 degrees, min. AOA: -3 degree

It appears from these data that a helicopter design of this nature may completely eliminate the possibility of inducing retreating blade stall while in its straight and level pusher-prop flight regime. The ramifications of this potential are simple, yet profound. This implies that the so called “speed limit” for rotary-wing craft would no longer be driven, in part, by the potential to stall the retreating blade. Rather, it would be dictated solely by drag and/or Mach effects. It is rumored that the X2 technology includes slowing down the rotor RPM at high speeds to help mitigate the problem of Mach divergence. A separate analysis would need to address whether the rotor tips might reach transonic speeds.

Chapter 9 Evaluating Lift

9.0 Analyzing the lift through rotation

The final phase of the study will involve the investigation into the lift generated by the coaxial rotor blades as they are utilized in the pusher-propeller configuration. One of the main differences in calculating lift for the rotor system versus a fixed wing aircraft is the dynamic nature of the rotating system. It is almost as though the rotating system is in a constant state of transient behavior where the steady-state is seen only after the period has been completed. It is important to consider this when evaluating lift. Evaluating steady-state lift on a fixed wing

aircraft can be completed without any consideration for time. Any snapshot in time will yield the same result. However, in a rotary-wing system the position and relative airspeed is constantly changing and is dependent on time. By extension the time dependency can be viewed as being rotation angle dependent.

This should make intuitive sense because lift is only generated by the blades in the space that they occupy in time. If a snapshot is taken so that a four bladed systems blades are located in the 0, 90, 180, and 270-degree locations, the lift generated by the individual blades will look different from the snapshot that shows them located in the 45, 135, 225, and 315-degree positions. While it has not been proven in this analysis, a standard helicopter design should result in a lift distribution that is balanced throughout the entire rotation. However, the distribution in the pusher configuration will be different. The purpose of the analysis in chapter 8 is that angle of attack is nearly eliminated on the retreating side of the disk. This should translate to a dramatic reduction, if not elimination, of lift Up until this point, it has been adequate to evaluate the flapping dynamics of a single blade. When evaluating the total lift that is generated, however, it is no longer practical or realistic to evaluate a single blade. Rather, the blades should be evaluated simultaneously relative to each other.

Before examining the state of all four blades simultaneously, a cursory investigation into a single blade will be made. Figure 9.1 shows the lift distribution of a single blade at a segment of the blade located at 75 percent of the span of the blade. The flight conditions mirror those of the cruise condition found in chapter 8 which was at sea level and at 78 m/s.

Per the design intent the lift distribution shows maximum amount of lift at the 90-degree position with all of the significant lift being generated on the advancing side. Once the rotation has passed through the 180-degree position, the lift generation is below an appreciable amount.

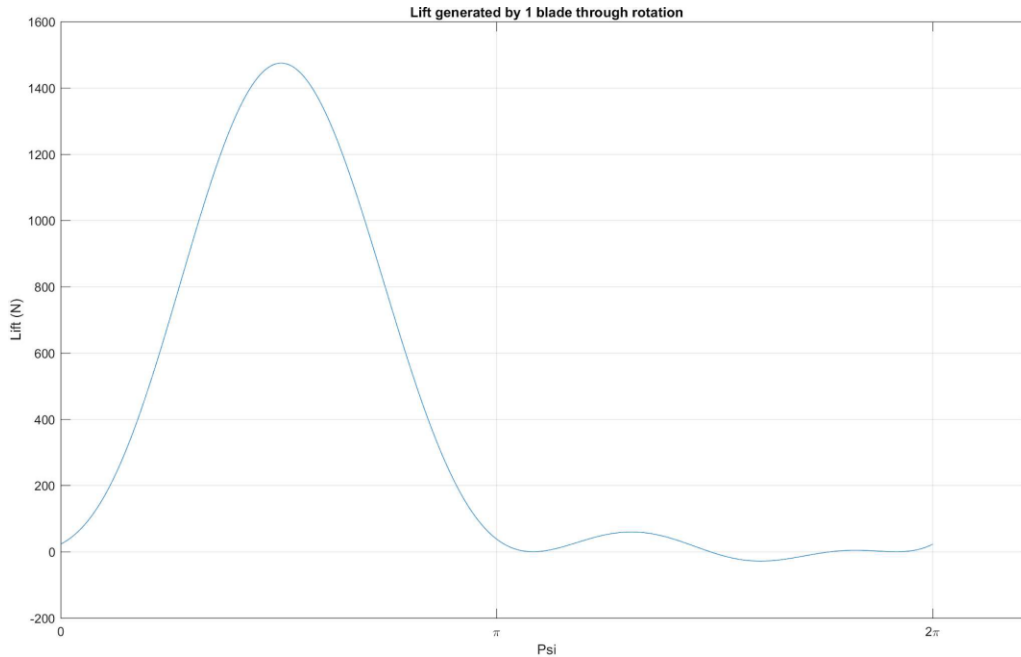


Figure 9.1 Lift distribution of a single blade about the rotation

Figure 9.2 shows lift distribution for all four blades through the rotation. Before proceeding to the analysis, there is something to be said about how the calculations were performed and how the graph should be read. Using conventional form, the starting location for blade number one is located at a radial azimuth of zero degrees. The reference of the horizontal axis on figure 9.2 applies to blade 1 only. The other three blades are phased relative to blade 1 in 90-degree increments, as is consistent with a four bladed rotor system. For example, while blade 1 is at 0 degrees, blade 2 is at 90 degrees, blade three at 180 degrees, and blade four at 270 degrees. Each blade has been calculated and phased appropriately so that the graph need only be read relative to blade 1. The figure shows a plot of the lift generated by each individual blade in its position relative to the first blade. Examining the zero degree mark, blade 1 is generating virtually no lift because is located at the 0 degree position. Blade 2 is shown to be generating lift at the peak of its cycle because its position relative to blade 1 is at 90 degrees which is the maximum lift generating position for this flight regime. Blades 3 and 4 are generating almost no lift because their positions, relative to blade 1, are at 180 and 270 degrees respectively and the system is designed not to generate lift in this region of the disk.

Now examine the position where along the graph where 90 degrees would be found. Again, this is the blade 1 position and the lift is at the peak of the cycle, per the design. While blade 1 is at 90 degrees, blade 2 is at 180 degrees, which is why its lift generation is approaching zero lift.

Simply put, the horizontal axis showing 0 to 2π references blade 1 only. The other lines depict the lift generated by the other blades in their own positions relative to the position of blade 1 on the figure.

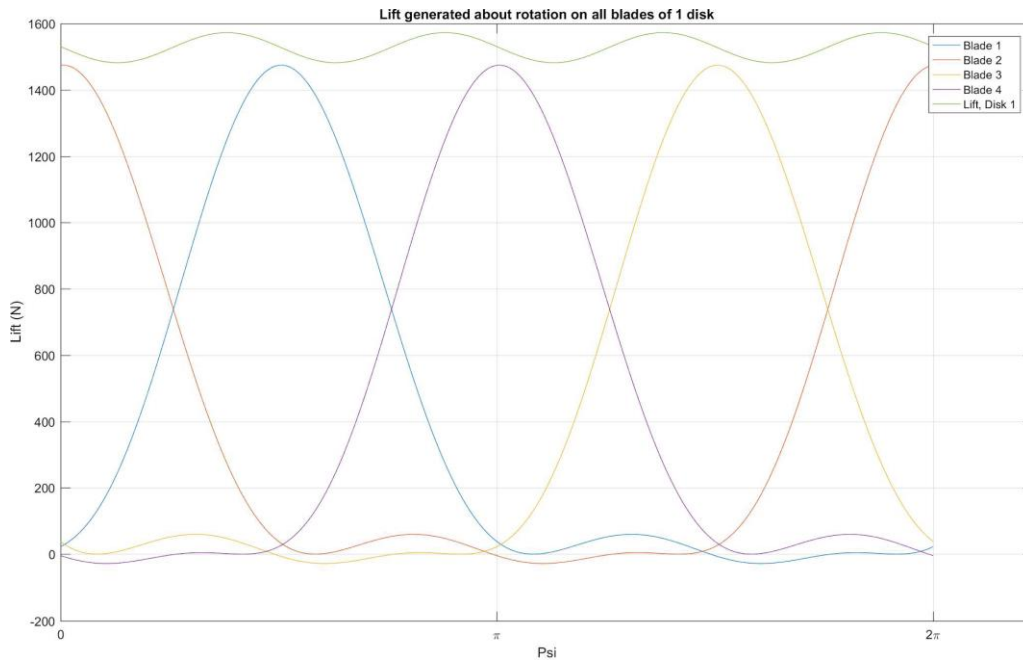


Figure 9.2 Lift distribution along a single disk

The results of figure 9.2 should come as no surprise following the analysis of figure 9.1. Tracking blade 1, it obviously mirrors the plot of figure 9.1 because it is the same. Blades 2-4 reflect the same with a phasing that is separated by 90 degrees between each blade. At the very top of the graph is a line that represents total lift that is generated by all of the blades for that azimuth position. It is cyclical in nature.

The reader is prompted to recall that figure 9.2 simply represents one of the two rotor disks. Disk two is rotating counter to disk one. Graphically, this would appear to be the flipped image of what is seen in figure 9.2. Figure 9.3 shows the lift distribution of disk 2 if it were superimposed over the disk 1 distribution as shown in figure 9.2.

To pick out the lift of each individual blade requires careful scrutiny, however, a couple of observations can be made with a cursory examination. First, it can be seen that the disk 2 lines complement the disk 1 lines in a way that should be expected in a mirrored system. Second, it should be noted that the two lines at the 1500 N position that represent the lift for the two disks are phased so that they mirror each other in a convenient way. Because these two lines represent the lift that is generated by both disks, they must be added together. The top most line of the graph represents the addition of the two lines and thus, represent the total lift that is generated for

each position about the rotation. While it is not perfectly so, it can be seen that the lift distribution is stable and very nearly constant about the rotation.

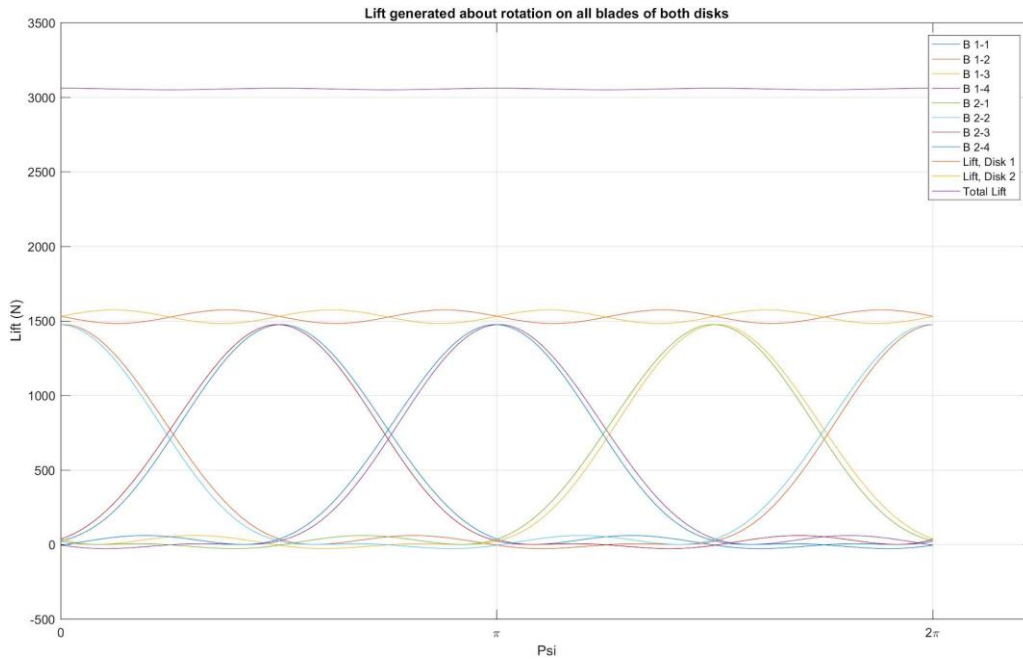


Figure 9.3 Lift distribution through the rotation of both disk 1 and disk 2

9.1 Evaluating the lift distribution about the rotation along the span

Now that the lift for a single section of the blade span for all four blades has been demonstrated, an evaluation of the lift generated by larger sections of the blade span can be conducted. For the purposes of this analysis, the span will be evaluated from the 40 percent position to the tip of the blade. The reason for this is two-fold: first, this accounts for any blade-cutout that might be designed into the system. Second, this will also help to avoid the reverse-flow region of the rotor disk which can cause anomalies in the model that cause the simulation to break down. The conditions for the simulation include a forward velocity of 78 m/s with an air density at sea level.

Figure 9.4 shows an evaluation that observes five sections of each blade. In assessments such as this one, it is best to make many small observations rather than few large ones in order to ensure that accuracy is of a higher fidelity. However, a graph with a small step size is convoluted and difficult to understand. The simulation will be conducted with the five steps first to determine the behavior and trend before increasing the fidelity.

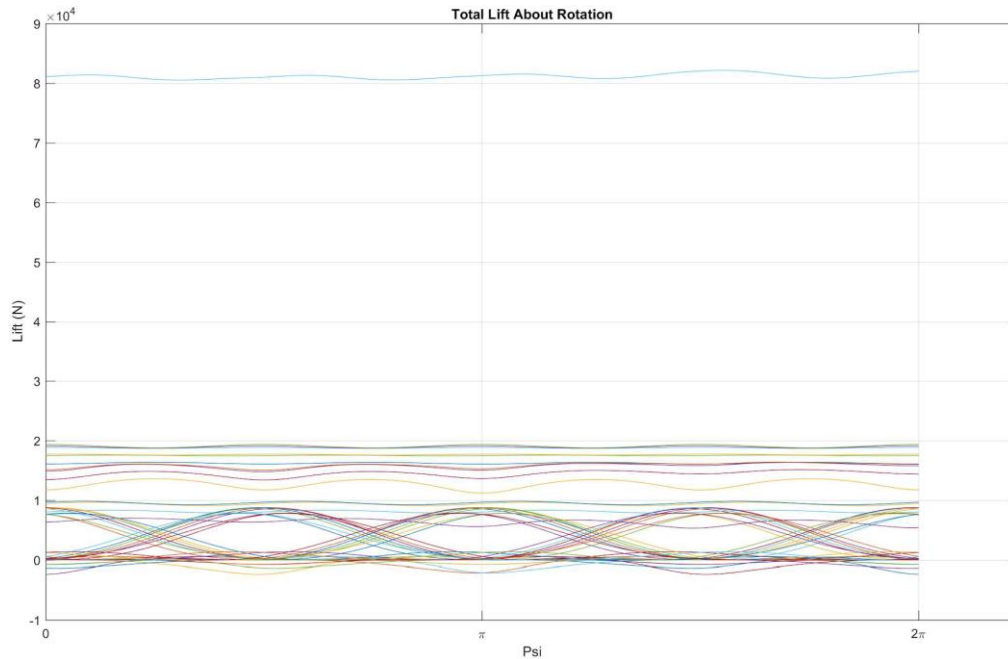


Figure 9.4 Lift distribution of all eight blades on both disks utilizing 5 segments

Figure 9.4 shows the lift distribution for all eight blades on both disks as they appear through the rotation relative to the planform area as dictated by disk 1. Finally, the top of the graph shows the total lift generation by both disks. It shows that the lift generated is 81,000 N, or 18,200 lbf. This is, of course, a rough estimation due to the large step size.

Figure 9.5 shows the evaluation using a smaller step size that splits the blade into 30 sections. It can be seen that the numerous lines that show the lift of the individual blades are indistinguishable from each other. However, the important data point, the total lift, is still visible. This analysis should be deemed as having a greater level of accuracy.

The lift generated, as shown in figure 9.5, is 75,000 N, or 16,860 lbf. This highlights the significance of utilizing smaller step sizes when performing an analysis of this nature. The difference in lift between the two cases is 1340 lbf, which is a significant amount of weight when considering potential use cases for the aircraft.

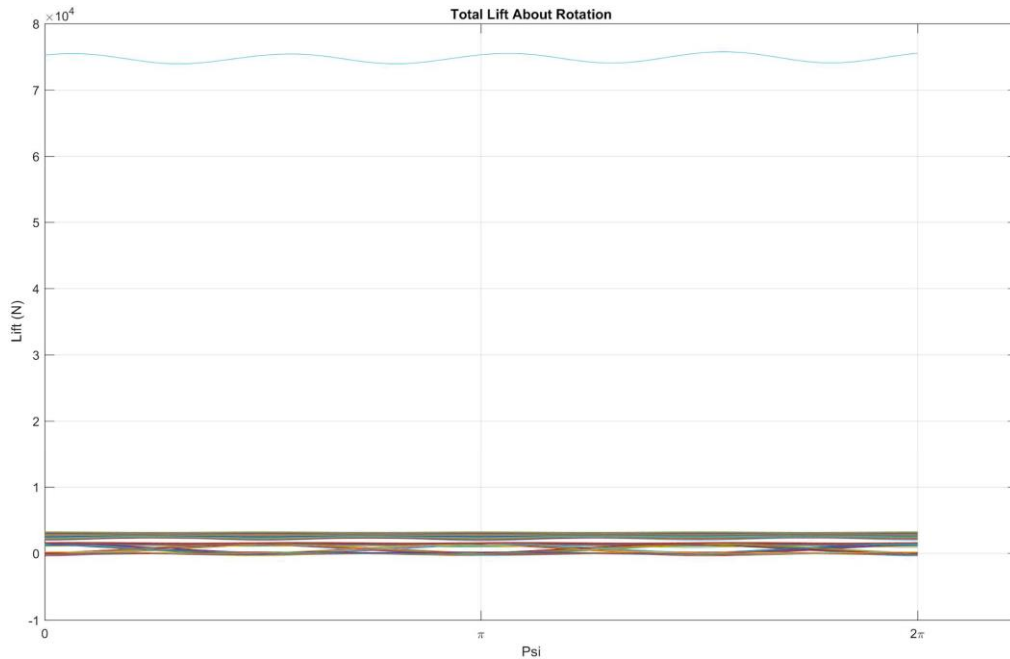


Figure 9.5 Lift distribution of all eight blades on both disks utilizing 30 blade span segments

9.2 Evaluating the lift distribution while hot and high

A critical design criterion in the modern era of helicopter design is a rotorcraft's ability to operate in high and hot conditions. The aircraft that stem from the X2 design, such as the S-97 and the SB>1, are intended to potentially see service in geographical locations such as Afghanistan. One of the challenges with operating in Afghanistan is that it is both hot and contains mountainous terrain. The “high and hot” conditions are the least ideal regime for a helicopter to fly in. Some helicopters, such as the UH-60 Blackhawk, are incapable of reaching certain destinations simply because they are too high. One of the design criteria for the X2 derivatives are that they can operate in high and hot conditions.

Figure 9.6. Shows the lift distribution under the same flight conditions as the previous assessment with the exception of the air density. The air density chosen for the evaluation is consistent with density found at 10,000 feet and 95 degrees Fahrenheit.

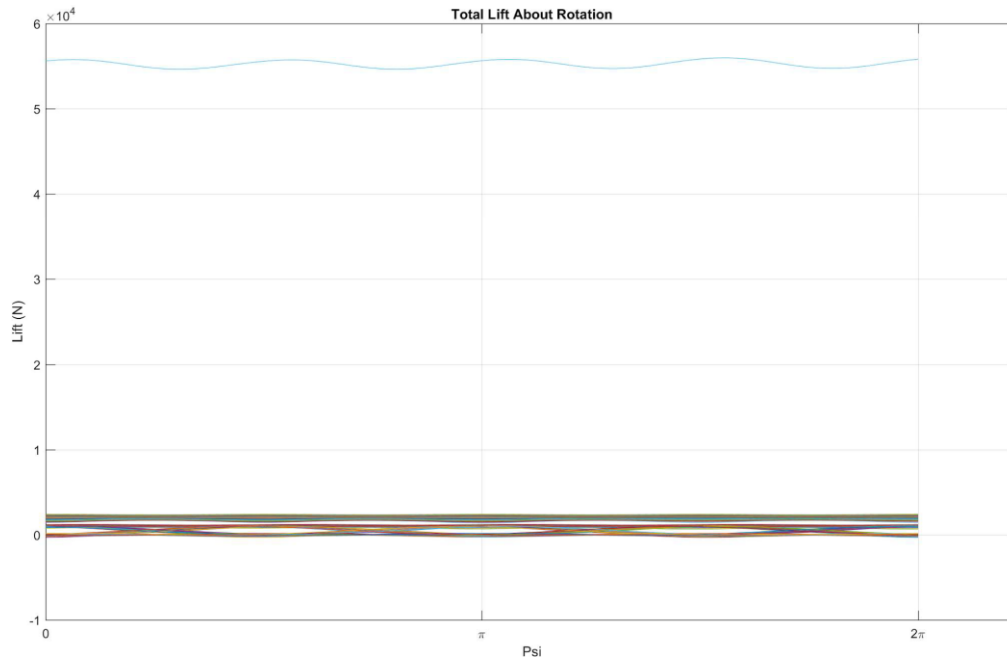


Figure 9.6. Lift about rotation in cruise at 10,000 ft and 95 degrees Fahrenheit.

As shown in figure 9.6, the max lift capable in the cruise condition at 10,000 feet and 95 degrees Fahrenheit is 55,000 N or 12,364 lbs. This is a significant loss of capability as it is 4,496 lbf less than what can be achieved at sea level.

Chapter 10 Conclusion and Future Work

10.0 Conclusion

The purpose of this project was to explore the occurrence of retreating blade stall in coaxial helicopters, such as the X2 and its derivatives that are propelled forward with a pusher-propeller in straight and level flight. Modelling of the flapping dynamics of helicopter rotor systems was necessary to determine the resultant aerodynamics in order to pinpoint the conditions and occurrences of retreating blade stall. The model required the use of Blade Element Theory in conjunction with the blade flapping equations of motion to determine effective angles of attack that the rotor blades experience. The analysis followed a ground up approach where each element of the aerodynamics and vehicle dynamics was developed from fundamentals of helicopter theory. A Matlab script was then written to perform the necessary analysis and the results were compared and confirmed against benchmark data from previously published work. Analysis of blade flapping dynamics for a standard helicopter configuration was conducted at several flight conditions and the conditions for inducing blade stall were found.

The analysis was then conducted with the coaxial/pusher-prop configuration. Due to the straight and level flight regime and the coaxial configuration of the X2 design, manipulation of the rotor flapping dynamics could be executed in ways that are inconsistent with standard helicopter design. The coaxial design allows for a maximization of lift on the advancing side of the rotor disk while minimizing the lift on the retreating side. This results in an asymmetric disk loading that is compensated for and balanced by the counter-rotating second disk. The ramifications of this are simple: generating near-zero lift on the retreating side is a result of a near-zero angle of attack. Because the system is designed to have no lift or high angles of attack on the retreating side of the disk, then retreating blade stall is eliminated in this flight regime. Retreating blade stall is partially responsible for the speed limit of helicopters in forward flight. Eliminating retreating blade stall also eliminates one more factor in the limit in forward velocity.

Finally, an assessment of the lift capability of the aircraft of the X2 configuration was made in sea level conditions as well as at 10,000ft, 95 degree Fahrenheit air density.

The conclusion of this study is that the X2 design provides the capability of allowing flight velocities that are much higher than traditional helicopter designs as well as providing a higher degree of safety with the elimination of retreating blade stall.

10.1 Future Work

Many assumptions and simplifications of this analysis were made. E.g. tip vortices, wake disturbances, and compressibility effects were neglected. To increase the fidelity of the study, future work on this subject will take into account these aerodynamic factors. Since retreating blade stall is no longer a contributing factor to the velocity limitations of helicopters in this configuration, Mach effects and drag are suspected to play a prominent role in the forward speed limit. Future work on this design will include an in depth analysis of the Mach effects and drag.

Another limitation to this study was the assumption that the blades behaved rigidly and either hinged or bent at the root of the blade. It intuitively follows that a flexible blade that is attached rigidly without a hinge will flap due to its own bending. The further from the root, the greater the bending angle. While this study assumed a constant flapping angle for the whole blade, in reality, this angle will change with the span of the blade. Future work will take into account the modeling of the blade bending.

References:

- [1] Han, W., Liu, J., Liu, C., Chen, L., Su, X., and Zhao, P., “Flap motion of helicopter rotors with novel, dynamic stall model,” *Open Physics*, vol. 14, Jan. 2016.
- [2] Kim, H. W., and Brown, R. E., “Modelling the Aerodynamics of Coaxial Helicopters – from an Isolated Rotor to a Complete Aircraft,” *EKC2008 Proceedings of the EU-Korea Conference on Science and Technology Springer Proceedings in Physics*, 2008, pp. 45–59.
- [3] Majhi, J. R., and Ganguli, R., “Helicopter blade flapping with and without small angle assumption in the presence of dynamic stall,” *Applied Mathematical Modelling*, vol. 34, 2010, pp. 3726–3740.
- [4] Kumar, M. R., and Venkatesan, C., “Effects of rotor blade-tip geometry on helicopter trim and control response,” *The Aeronautical Journal*, vol. 121, Sep. 2017, pp. 637–659.
- [5] Rong, W., and PinQi, X. I. A., “Control of dynamic stall of helicopter rotor blades,” *Science China Technological Sciences*, vol. 56, Jan. 2013, pp. 171–180.
- [6] Barbely, N. L., Komerath, N. M., and Novak, L. A., “A study of coaxial rotor performance and flow field characteristics,” *Defense Technical Information Center*, Jan. 2016, pp. 1–15.
- [7] Merz, C. B., Wolf, C. C., Richter, K., Kaufmann, K., Mielke, A., and Raffel, M., “Spanwise Differences in Static and Dynamic Stall on a Pitching Rotor Blade Tip Model,” *Journal of the American Helicopter Society*, vol. 62, Jan. 2017, pp. 1–11.

- [8] Fernandes, S. D., “Performance analysis of a coaxial helicopter in hover and forward flight,” Embry-Riddle Aeronautical University, May 2017.
- [9] Fernandes, S. D., “Performance analysis of a coaxial helicopter in hover and forward flight,” Embry-Riddle Aeronautical University, May 2017.
- [10] Go, J.-I., Kim, D.-H., and Park, J.-S., “Performance and Vibration Analyses of Lift-Offset Helicopters,” *International Journal of Aerospace Engineering*, vol. 2017, Jun. 2017, pp. 1–13.
- [11] Lütke, B., Nuhn, J., Govers, Y., and Schmidt, M., “Design of a rotor blade tip for the investigation of dynamic stall in the transonic wind-tunnel Göttingen,” *The Aeronautical Journal*, vol. 120, Apr. 2016, pp. 1509–1533.
- [12] Lee, S., Cho, L., and Cho, J., “Unsteady Aerodynamic Analysis and Wake Simulation of Helicopter Rotors using the Time-Domain Panel Method,” *Transactions Of The Japan Society For Aeronautical And Space Sciences*, vol. 55, 2012, pp. 21–29.
- [13] Johnson, W., *Helicopter theory*, Dover Publications Inc., 1994.
- [14] Padfield, G. D., *Helicopter flight dynamics: the theory and application of flying qualities and simulation modeling*, Reston, VA: American Inst. of Aeronautics and Astronautics, 2007.
- [15] Saunders, G. H., *Dynamics of helicopter flight*, New York: John Wiley & Sons, 1975.
- [16] Cantrell, P., “All Star Helicopters.” Retrieved from
<http://www.copters.com/aero/retreating.html>

- [17] NASA Available: <https://www.grc.nasa.gov/www/k-12/airplane/incline.html>.
- [18] McCrosky, W. J., "The Phenomenon of Dynamic Stall," NASA Technical Memorandum 81264, Mar. 1981.
- [19] "Centrifugal Force," Helicopter Aviation Available: http://www.copters.com/aero/centrifugal_force.html.
- [20] Majhi, J. R., and Ganguli, R., "Helicopter blade flapping with and without small angle assumption in the presence of dynamic stall," Applied Mathematical Modelling, vol. 34, 2010, pp. 3726–3740.
- [21] "SB>1 DEFIANT™ JMR Technology Demonstrator," Lockheed Martin Available: <https://www.lockheedmartin.com/en-us/products/sb1-defiant-technology-demonstrator.html>.
- [22] "S-97 RAIDER® Demonstrator," Lockheed Martin Available: <https://www.lockheedmartin.com/en-us/products/s-97-raider-helicopter.html>.
- [23] Aitken, A., "Helicopter Rotorhead Design," Redback Aviation Available: <http://www.redbackaviation.com/helicopter-rotorhead-design/>.

Appendix A - Blade Element Theory Matlab Program

%Blade Element Theory - Aaron Ford

```
clear, clc
%Hover Conditions
%%
%Rotational Velocity
Vt=204.826;           %tip Velocity m/sec
R=3.835;             %Radius of Blade m
Omega=Vt/R;         %Rotational Velocity 1/sec
b=2;                %Number of Blades
rho=1.225;
ar=0.1;             %Cla, coefficient of lift slope
cr=0.18288;        %chord of rotor blade
cd=0.1;            %coeff. of drag
Ab = pi*R^2;
arbar=ar/R;
crbar=cr/R;
%rbar=r/R;
%AOA at radius r - alpha(r)
%{
tr = Pitch anfle of the Blade
vc = Climb Velocity
vr = Velocity at Radius r
%}
theta=5;
%tr=tr*pi/180;
Vc=0;
i=200;
R=10;
vr=zeros(1,i);
%r=zeroes(1, i+1);
%%
%Induced Velocity eqn 3.15
radius=R/i:R/i:R;
for r=1:length(radius)
vr(r)=Vt*...
(-1*...
(((ar*b*cr)/(16*pi*R))+...

```

```

(Vc/(2*Vt)))+....
sqrt((((ar*b*cr)/(16*pi*R))+(Vc/(2*Vt)))^2+....
((ar*b*cr*radius(r)*theta)/(8*pi*R))-....
((ar*b*cr*Vc)/(8*pi*R*Vt))));
end

%Radius of blade span
figure,
plot(radius, vr);
xlabel('Blade Length (m)');
ylabel('Induced Velocity (m/s)');
title('Induced Velocity Along Span of Blade');
%Vr_bar

x=0;
j=200;
%k=10000;
R=10;
r=1/j:1/j:1;
rbar=r/R;

%i=10;
%vr=zeros(1,i);

%Angle of Attack Along Blade Span - Eqn 3.1a(assumes vc and vr
are small)
alpha=zeros(1,i);
for r=1:length(vr)
%vr(rbar)=Omega*r;

alpha(r)=theta-(Vc+vr(r))/(Omega*radius(r));
%alpha(r)=(theta-atan((Vc+vr(r))/(Omega*r))*(180/pi));
end

figure,
subplot(3,1,1)
plot(radius, alpha);
title('AOA Along Blade Span');
xlabel('Span (m)')
ylabel('AOA (Degrees)');

```

```

%Lift along blade span - Eqn 3.3
L=zeros(1,i);
for r=1:length(vr)
L(r)=0.5*ar*rho*(theta-
((Vc+vr(r))/(Omega*radius(r))))*cr*(Omega*radius(r))^2;
end

subplot(3,1,2)
plot(radius, L);
title('Lift Along Blade Span');
xlabel('Span (m)');
ylabel('Lift (N)');

%Profile Drag - Eqn 3.4
D=zeros(1,i);
for r=1:length(radius)
D(r)=0.5*cd*rho*cr*(Omega*radius(r))^2;
end

subplot(3,1,3)
plot(radius, D);
title('Drag Along Blade Span');
xlabel('Span (m)');
ylabel('Drag (N)');
%sgtitle('AOA, Lift, Drag')

%Elementary Torque - Eqn 3.7
Q=zeros(1,i);
phi_r=zeros(1,i);
for r=1:length(radius)
    phi_r(r)=atan((Vc+vr(r))/(Omega*radius(r)));
    Q(r)=(L(r)*sin(phi_r(r))+D(r)*cos(phi_r(r)))*radius(r);
end

figure,
subplot(3,1,1)
plot(radius, Q);
title('Torque Along Blade Span');
xlabel('Span (m)');
ylabel('Torque (Nm)');

```

```

% Thrust - Eqn 3.8
T=zeros(360,i);
for o=1:360
for r=1:length(radius)
T(o,r)=L(r)-D(r)*((Vc+vr(r))/(Omega*radius(r)));
end
end

% figure('color', 'white')
% cl = round(min(T(:))-1):0.4:round(max(T(:))+1);
% polarplot3d(T,'plottype','contour','polargrid',{6
4},'contourlines',cl, 'radialrange',R);
% set(gca,'dataaspectratio',[1 1 1],'view',[90 90]);
% colorbar

subplot(3,1,2)
plot(radius, T);
title('Thrust Along Blade Span');
xlabel('Span (m)');
ylabel('Thrust (N)');

% Power - Eqn 3.10
P=zeros(1,i);
for r=1:length(radius)
P(r)=Q(r)*Omega;
end

subplot(3,1,3)
plot(radius, P);
title('Power Required Along Blade Span');
xlabel('Span (m)');
ylabel('Power (W)');

```

Appendix B - Hinged Flapping Matlab Program

```

%% Hinged Flapping functions
%% Current Project File
% Aaron Ford

```

```

% AE295 Project

% Clean House
    clear, clc, close all

% Number of Revolutions
    num_rev = 1;
    rev = num_rev*2*pi();

% System Variables and Flight Conditions
    alphaS = 4;
    R = 8.18;
    c = 0.5273; % meters
    CL = 1.2;
    CD = 0;
    Vinf = 78; % m/s, Cruise Speed
    %Vinf = 99; % m/s, Max Speed
    %Vinf = 128.6; % Max speed for SB>1
    rho = 1.225;
    Ib = 20726;
    %Ib = 85.5;
    Cla = 0.1*(180/pi);
    r = 0.75*R;
    OMEGA=27;
    delta_r = 0.02;

% Inertia Calculations
    m = 113.6; % kg, mass of blade
    Ibf = m*delta_r*r^2; % MOI for blade Element

% Control Input
    theta0 = 8; % Collective
    thetalc = 0; % Cyclic Roll
    thetals = -4; % Cyclic Pitch

    theta0 = theta0*(pi/180); % Collective
    thetalc = thetalc*(pi/180); % Cyclic Roll
    thetals = thetals*(pi/180); % Cyclic Pitch

%% ODE 45 Calculation and Plots

% Initial Conditions to get ODE started.
    B0 = [0, 0];

% For loop iterates to re-insert initial conditions to smooth
out
% evaluation.

```

```

    for k = 1:20
        [psi0de, B0de] = ode45(@(psi0de, B0de)flap0de451(psi0de,
B0de, Vinf, theta0,thetalc,thetals, Ib, alphaS),[0, rev], B0);

        %plot(psi0de,B0de(:,1))
        %hold on
        %pause
        B0 = [B0de(end,1),B0de(end,2)];
    end
B0de = B0de*(180/pi);
% Plot for Fourier vs ODE 45
    %figure,
    subplot(2,2,1)
%    plot(psi0de,Bf)
    hold on
    plot(psi0de,B0de(:,1))
%    hold on
%    plot(360,0, '*')

    xticks([0 pi 2*pi])
    xticklabels({'0', '\pi', '2\pi'})
    ylabel('Beta')
    %title('(a) Hinged Blade Flapping')
    title('Hinged Blade Flapping')
    legend('ODE45')
    grid on

%% Calculate Phi and AOA

    mu = (Vinf*cos(alphaS))/(OMEGA*R);
    gamma = (rho*Cl*a*c*R^4)/Ib;
    lambda = (Vinf*sin(alphaS) + gamma)/(OMEGA*R);

% Preallocate for speed
    Ut = zeros(length(psi0de),1);
    Up = zeros(length(psi0de),1);
    phi = zeros(length(psi0de),1);
    theta = zeros(length(psi0de),1);
    AOA = zeros(length(psi0de),1);

    for j = 1:length(psi0de)

% Calculate Phi
        Ut(j) = (r + mu*sin(psi0de(j)));
        Up(j) = (lambda + r*B0de(j,2)+B0de(j,1)*mu*cos(psi0de(j)));
        phi(j) = (Up(j)./Ut(j));

```

```

    %phi = phi*(180/pi);
% Calculate AOA

    theta(j) = theta0 + thetalc*cos(psi0de(j)) +
thetals*sin(psi0de(j));
    theta = theta*(180/pi);
    AOA(j) = theta(j) - phi(j);

end
U = [Up Ut];
% Plot Phi and AOA vs Psi

%figure,
subplot(2,2,2)
plot(psi0de, phi)
title('(b) Induced Inflow Angle of Attack')
xlabel('Psi')
xticks([0 pi 2*pi])
xticklabels({'0', '\pi', '2\pi'})
ylabel('Phi')
legend('Phi')
grid on

%figure,
subplot(2,2,3)
plot(psi0de, AOA)
title('(c) Total Effective Angle of Attack')
title('Hinged Total Effective Angle of Attack')
xticks([0 pi 2*pi])
xticklabels({'0', '\pi', '2\pi'})
ylabel('AOA')
legend('AOA')
grid on

% Plot Beta vs AOA
%figure,
subplot(2,2,4)
plot(psi0de, B0de(:,1))
hold on
plot(psi0de, AOA)
title('(d) Flapping Angle vs AOA')
xticks([0 pi 2*pi])
xticklabels({'0', '\pi', '2\pi'})
ylabel('Angle in Degrees')
legend('Beta', 'AOA')
grid on

```

```

% Benchmark Figures
figure,
subplot(2,1,1)
hold on
plot(psi0de, B0de(:,1))
xticks([0 pi 2*pi])
xticklabels({'0', '\pi', '2\pi'})
ylabel('Beta')

title('Hinged Blade Flapping')
legend('ODE45')
grid on

subplot(2,1,2)
plot(psi0de, AOA)
%title('(c) Total Effective Angle of Attack')
title('Hinged Total Effective Angle of Attack')
xticks([0 pi 2*pi])
xticklabels({'0', '\pi', '2\pi'})
ylabel('AOA')
legend('AOA')
grid on

HBenchB = [psi0de B0de(:,1)];
HBenchA = [psi0de AOA];

save('HBenchB.mat', 'HBenchB');
save('HBenchA.mat', 'HBenchA');

%% Functions
function dum = flap0de451(psi, B, Vinf, theta0, theta1c, theta1s,
Ib, alphaS)

alphaS = alphaS*(pi/180);
c = 0.5273;
Cla = 0.1*(180/pi);
rho = 1.225;
R = 8.18;
OMEGA = 27;
delta_r = 0.02;
mu = (Vinf*cos(alphaS))/(OMEGA*R);
gamma = (rho*Cla*c*R^4)/Ib;
lambda = (Vinf*sin(alphaS) + gamma)/(OMEGA*R);
r = 0.75;
Ut = (r + mu*sin(psi));
Up = (lambda + r*B(2)+B(1)*mu*cos(psi));

theta = theta0 + theta1c*cos(psi) + theta1s*sin(psi);

```

```

%Cla = 0.1;
L = 0.5*((Ut^2)*theta - ((Up)).*(Ut));

Mf = gamma*L*r;

%dim = R/(OMEGA^2);
%dim = 1;
%Bddot = -((cos(B(1)))*sin(B(1))) + (Mf/Ib)*dim*delta_r;
Bddot = -(B(1)) + Mf;
dum = [B(2), Bddot];
dum = dum(:);
End

```

Appendix C - Hingeless Blade Flapping MatLab Program

```

%% Hingeless Flapping ODE
%% Current Project File
% Aaron Ford
% AE295 Project

% Clean House
clear, clc, close all

% Number of Revolutions
num_rev = 1;
% Percent of Blade cutout
pct = 0.5;
% Number of steps
nSteps = 30;
% Critical Angle of Attack
AlphaCrit = 0;
% Forward Flight Velocity
Vinf = 78; % m/s, Cruise Speed
%Vinf = 99; % m/s, Max Speed
%Vinf = 128.6;

% Control Input
theta0 = 10; % Collective
thetalc = 0; % Cyclic Roll
thetals = 0; % Cyclic Pitch

% System Variables and Flight Conditions

```

```

rev = num_rev*2*pi();
alphaS = 0;
R = 8.18;
c = 0.5273; % meters

rho = 1.225;
Ib = 20726;
Cla = 0.1;
%r = 0.75*R;
r = 0.75;
OMEGA=27;
delta_r = 0.02;

% Deg2Rad
theta0 = theta0*(pi/180); % Collective
thetalc = thetalc*(pi/180); % Cyclic Roll
thetals = thetals*(pi/180); % Cyclic Pitch
%thetaTW = thetaTW*(pi/180); % Blade Twist
Cla = Cla*(180/pi);

mu = (Vinf*cos(alphaS))/(OMEGA*R);
gamma = (rho*Cla*c*R^4)/Ib;
lambda = (Vinf*sin(alphaS) + gamma)/(OMEGA*R);

%% ODE 45 Calculation and Plots

% Initial Conditions to get ODE started.
B0 = [0.727459607119437,-1.57925956832798];

% For loop iterates to re-insert initial conditions to smooth
out
% evaluation.

for k = 1:20
    [psi0de, B0de] = ode45(@(psi0de, B0de)flap0de451(psi0de,
B0de, Vinf, theta0,thetalc,thetals, Ib, r, alphaS),[0, rev],
B0);

```

```

    B0 = [B0de(end,1),B0de(end,2)];
    end
B0de = B0de*(180/pi);

% Plot for Fourier vs ODE 45

    subplot(2,2,1)
    hold on
    plot(psi0de,B0de(:,1))
    xticks([0 pi 2*pi])
    xticklabels({'0', '\pi', '2\pi'})
    ylabel('Beta')
    title('ODE 45 of Hingless Rotor System')
    legend('ODE45')
    grid on

%% Calculate Phi and AOA

% Preallocate for speed
    Ut = zeros(length(psi0de),1);
    Up = zeros(length(psi0de),1);
    phi = zeros(length(psi0de),1);
    theta = zeros(length(psi0de),1);
    AOA = zeros(length(psi0de),1);

    for j = 1:length(psi0de)

% Calculate Phi
        Ut(j) = (r + mu*sin(psi0de(j)));
        Up(j) = (lambda + r*B0de(j,2)+B0de(j,1)*mu*cos(psi0de(j)));
        phi(j) = (Up(j)./Ut(j));
        %phi = phi*(180/pi);
% Calculate AOA

        theta(j) = theta0 + thetalc*cos(psi0de(j)) +
thetals*sin(psi0de(j));
        theta = theta*(180/pi);
        AOA(j) = theta(j) - phi(j);

```

```

    end
    U = [Up Ut];
% Plot Phi and AOA vs Psi

%figure,
subplot(2,2,2)
plot(psi0de, phi)
title('Induced Inflow Angle of Attack')
xlabel('Psi')
xticks([0 pi 2*pi])
xticklabels({'0', '\pi', '2\pi'})
ylabel('Phi')
legend('Phi')
grid on

%figure,
subplot(2,2,3)
plot(psi0de, AOA)
title('Total Effective Angle of Attack')
xticks([0 pi/2 pi 3*pi/2 2*pi])
xticklabels({'0', '\pi/2', '\pi', '3\pi/2', '2\pi'})
ylabel('AOA')
legend('AOA')
grid on

% Plot Beta vs AOA
%figure,
subplot(2,2,4)
plot(psi0de, B0de(:,1))
hold on
plot(psi0de, AOA)
title('Flapping Angle vs AOA')
xticks([0 pi 2*pi])
xticklabels({'0', '\pi', '2\pi'})
ylabel('Angle in Degrees')
legend('Beta', 'AOA')
grid on

%% Functions

```

```
function dum = flap0de451(psi, B, Vinf, theta0, theta1c, theta1s,
Ib, r, alphaS)
```

```

%alphaS = 15;
alphaS = alphaS*(pi/180);
c = 0.5273;
Cla = 0.1*(180/pi);
rho = 1.225;
R = 8.18;
OMEGA = 27;
mu = (Vinf*cos(alphaS))/(OMEGA*R);
gamma = (rho*Cla*c*R^4)/Ib;
lambda = (Vinf*sin(alphaS) + gamma)/(OMEGA*R);
e = 0.10;
nu = (r-e)/(1-e);
v = 1.15;
% Arbitrarily Chosen Flapping Freq
%v = 1.2;

Ut = (r + mu*sin(psi));
Up = (lambda + r*B(2)+B(1)*mu*cos(psi));

theta = theta0 + theta1c*cos(psi) + theta1s*sin(psi);

L = 0.5*((Ut^2)*theta - ((Up)).*(Ut));

Mf = gamma*L*nu;

Bddot = -(B(1))*v^2 + Mf;

dum = [B(2), Bddot];

dum = dum(:);

```

```
end
```

Appendix D - Hingeless AOA Distribution Matlab Program

```

%% Fourier and ODE 45 the Flapping functions
%% Current Project File
% Aaron Ford

```

```

% AE295 Project
% Clean House
    clear, clc, close all

% Number of Revolutions
    num_rev = 1;
% Percent of Blade cutout
    pct = 0.5;
% Number of steps
    nSteps = 30;
% Critical Angle of Attack
    AlphaCrit = 15;
% Forward Flight Velocity
    Vinf = 78; % m/s, Cruise Speed
    %Vinf = 99; % m/s, Max Speed
    %Vinf = 155;

% System Variables and Flight Conditions
    rev = num_rev*2*pi();
    alphaS = 0;
    R = 8.18;
    c = 0.5273; % meters

    rho = 1.225;
    Ib = 20726;
    Cla = 0.1;
    r = 0.75;%*R;
    OMEGA=27;
    delta_r = 0.02;

    mu = (Vinf*cos(alphaS))/(OMEGA*R);
    gamma = (rho*Cla*c*R^4)/Ib;
    lambda = (Vinf*sin(alphaS) + gamma)/(OMEGA*R);
% Control Input
    theta0 = 8; % Collective
    thetalc = 0; % Cyclic Roll
    thetals = 0; % Cyclic Pitch

% Deg2Rad

```

```

theta0 = theta0*(pi/180);      % Collective
thetalc = thetalc*(pi/180);   % Cyclic Roll
thetals = thetals*(pi/180);   % Cyclic Pitch

Cla = Cla*(180/pi);

%% ODE 45 Calculation and Plots

% Initial Conditions to get ODE started.
B0 = [0, 0];
% opts = odeset('RelTol',1e-12,'AbsTol',1e-
12,'InitialStep',1e-4,...
%           'MaxStep',1e-3,'Refine',5,'Events',@eventX0);
opts = odeset('MaxStep',1e-1);

% For loop iterates to re-insert initial conditions to smooth
out
% evaluation.
for k = 1:20
    [psi0de, B0de] = ode45(@(psi0de, B0de)flap0de451(psi0de,
B0de, Vinf, theta0,thetalc,thetals, Ib,r),[0, rev], B0, opts);

    %plot(psi0de,B0de(:,1))
    %hold on
    %pause
    B0 = [B0de(end,1),B0de(end,2)];
end
B0de = B0de*(180/pi);
% Plot for Fourier vs ODE 45
%figure,

%% Calculate Phi and AOA

% Preallocate for speed
Ut = zeros(length(psi0de),1);
Up = zeros(length(psi0de),1);
U = zeros(length(psi0de),1);
phi = zeros(length(psi0de),1);
theta = zeros(length(psi0de),1);

```

```

AOA = zeros(length(psi0de),1);

rBar = [0.2 0.3 0.4 0.5 0.6 0.75 0.8 0.9];

k = nSteps*(pct);
figure,
for n = k:nSteps

    r = n/nSteps;
    for j =1:length(psi0de)

% Calculate Phi
        Ut(j) = (r + mu*sin(psi0de(j)));
        Up(j) = (lambda + r*B0de(j,2)+B0de(j,1)*mu*cos(psi0de(j)));
        U(j) = sqrt(Ut(j)^2 + Up(j)^2);
        phi(j) = (Up(j)./Ut(j));
        %phi = phi*(180/pi);
% Calculate AOA

        theta(j) = theta0 + thetalc*cos(psi0de(j)) +
thetals*sin(psi0de(j));
        theta = theta*(180/pi);
        AOA(j,n) = theta(j) - phi(j);

    end

% Plot Phi and AOA vs Psi

    %figure,
    plot(psi0de, AOA)
    title('Total Effective Angle of Attack Along Span')
    xticks([0 pi 2*pi])
    xticklabels({'0', '\pi', '2\pi'})
    ylabel('AOA')
    grid on
    hold on
end

%% Functions
function dum = flap0de451(psi, B, Vinf, theta0,thetalc,thetals,
Ib, r)

```

```

alphaS = 0;
alphaS = alphaS*(pi/180);
c = 0.5273;
Cla = 0.1*(180/pi);
rho = 1.225;
R = 8.18;
OMEGA = 27;
mu = (Vinf*cos(alphaS))/(OMEGA*R);
gamma = (rho*Cla*c*R^4)/Ib;
lambda = (Vinf*sin(alphaS) + gamma)/(OMEGA*R);
e = 0.10;
nu = (r-e)/(1-e);
v = 1.15;

Ut = (r + mu*sin(psi));
Up = (lambda + r*B(2)+B(1)*mu*cos(psi));

theta = theta0 + theta1c*cos(psi) + theta1s*sin(psi);

L = 0.5*((Ut^2)*theta - ((Up)).*(Ut));

Mf = gamma*L*nu;

Bddot = -(B(1))*v^2 + Mf;

dum = [B(2), Bddot];

dum = dum(:);
end

```

Appendix E - Hingeless Lift Distribution Matlab Program

```

%% Hingeless Lift Distribution
%% Current Project File
% Aaron Ford
% AE295 Project

```

```

% Clean House
    clear, clc, close all

% Number of Revolutions
    num_rev = 1;
% Percent of Blade cutout
    pct = 0.6;
% Number of steps
    nSteps = 30;
% Critical Angle of Attack
    AlphaCrit = 0;
% Forward Flight Velocity
    %Vinf = 78; % m/s, Cruise Speed
    %Vinf = 99; % m/s, Max Speed
    Vinf = 126;

% Control Input
    theta0 = 8; % Collective
    thetalc = 13; % Cyclic Roll
    thetals = 11; % Cyclic Pitch

% System Variables and Flight Conditions
    rev = num_rev*2*pi();
    alphaS = 0;
    R = 8.18;
    c = 0.5273; % meters

    rho = 1.225;
    %Density at 10,000' and 95f
    %rho = 0.9053;
    Ib = 20726;
    Cla = 0.1;
    %r = 0.75*R;
    r = 0.75;
    OMEGA=27;
    delta_r = R/nSteps;

% Deg2Rad
    theta0 = theta0*(pi/180); % Collective

```

```

    thetalc = thetalc*(pi/180);    % Cyclic Roll
    thetals = thetals*(pi/180);    % Cyclic Pitch
    %thetaTW = thetaTW*(pi/180);    % Blade Twist
    Cla = Cla*(180/pi);

    mu = (Vinf*cos(alphaS))/(OMEGA*R);
    gamma = (rho*Cla*c*R^4)/Ib;
    lambda = (Vinf*sin(alphaS) + gamma)/(OMEGA*R);

    opts = odeset('RelTol', 1e-3, 'AbsTol', 1e-
3, 'InitialStep', 1e-2, 'MaxStep', 1e-2, 'Refine', 5);

    kk = round(nSteps*(pct));
    row = nSteps - kk;
    Lift = zeros(3146,row);
figure,
for n = kk:nSteps

    r = n/nSteps;

%% Blade 1

% Initial Conditions to get ODE started.
    B0 = [0,0];

% For loop iterates to re-insert initial conditions to smooth
out
% evaluation.

    for k = 1:20
        [psi0de, B0de] = ode45(@(psi0de, B0de)flap0de451(psi0de,
B0de,Vinf, theta0,thetalc,thetals, Ib, r, alphaS),[0, rev],
B0,opts);

        B0 = [B0de(end,1),B0de(end,2)];
    end
B0de = B0de*(180/pi);

```

```

% Preallocate for speed
    Ut = zeros(length(psi0de),1);
    Up = zeros(length(psi0de),1);
    phi = zeros(length(psi0de),1);
    theta = zeros(length(psi0de),1);
    AOA = zeros(length(psi0de),1);

    for j = 1:length(psi0de)

% Calculate Phi
        Ut(j) = (r + mu*sin(psi0de(j)));
        Up(j) = (lambda + r*B0de(j,2)+B0de(j,1)*mu*cos(psi0de(j)));
        phi(j) = (Up(j)./Ut(j));
        %phi = phi*(180/pi);
% Calculate AOA

        theta(j) = theta0 + thetalc*cos(psi0de(j)) +
        thetals*sin(psi0de(j));
        theta = theta*(180/pi);
        AOA(j) = theta(j) - phi(j);

    end
    U = [Up Ut];
% Plot Phi and AOA vs Psi

V = zeros(j,1);
L1 = zeros(j,1);

for mm = 1:j

    V(mm) = OMEGA*r + Vinf*sin(psi0de(mm));
    L1(mm) = 0.5*rho*V(mm)^2*c*Cla*AOA(mm)*(pi/180)*delta_r;
    %L(mm) = 0.5*((Ut(mm)^2)*(pi/180)*theta(mm) -
    ((Up(mm))).*(Ut(mm)));

end
%%

```

```

%figure,
plot(psi0de,L1)
hold on
xticks([0 pi 2*pi])
xticklabels({'0', '\pi', '2\pi'})
xlabel('Psi')
ylabel('Lift')
grid on

%% Blade 2

% Initial Conditions to get ODE started.
B0 = [0,0];

% For loop iterates to re-insert initial conditions to smooth
out
% evaluation.

    for k = 1:20
        [psi0de, B0de] = ode45(@(psi0de, B0de)flap0de452(psi0de,
B0de,Vinf, theta0,thetalc,thetals, Ib, r, alphaS),[0, rev],
B0,opts);

        B0 = [B0de(end,1),B0de(end,2)];
    end
B0de = B0de*(180/pi);

% Preallocate for speed
Ut = zeros(length(psi0de),1);
Up = zeros(length(psi0de),1);
phi = zeros(length(psi0de),1);
theta = zeros(length(psi0de),1);
AOA = zeros(length(psi0de),1);

    for j = 1:length(psi0de)

% Calculate Phi
Ut(j) = (r + mu*sin(psi0de(j) + pi/2));

```

```

    Up(j) = (lambda + r*B0de(j,2)+B0de(j,1)*mu*cos(psi0de(j) +
pi/2));
    phi(j) = (Up(j)./Ut(j));
    %phi = phi*(180/pi);
% Calculate AOA

    theta(j) = theta0 + thetalc*cos(psi0de(j) + pi/2) +
thetals*sin(psi0de(j) + pi/2);
    theta = theta*(180/pi);
    AOA(j) = theta(j) - phi(j);

end
    U = [Up Ut];
% Plot Phi and AOA vs Psi

V = zeros(j,1);
L2 = zeros(j,1);

for mm = 1:j

    V(mm) = OMEGA*r + Vinf*sin(psi0de(mm) + pi/2);
    L2(mm) = 0.5*rho*V(mm)^2*c*Cla*AOA(mm)*(pi/180)*delta_r;
    %L(mm) = 0.5*((Ut(mm)^2)*(pi/180)*theta(mm) -
((Up(mm))).*(Ut(mm))));

end
%%

    plot(psi0de,L2)
    hold on

%% Blade 3

% Initial Conditions to get ODE started.
    B0 = [0,0];

```

```

% For loop iterates to re-insert initial conditions to smooth
out
% evaluation.

    for k = 1:20
        [psi0de, B0de] = ode45(@(psi0de, B0de)flap0de453(psi0de,
B0de,Vinf, theta0,thetalc,thetals, Ib, r, alphaS),[0, rev],
B0,opts);

        B0 = [B0de(end,1),B0de(end,2)];
    end
B0de = B0de*(180/pi);

% Preallocate for speed
    Ut = zeros(length(psi0de),1);
    Up = zeros(length(psi0de),1);
    phi = zeros(length(psi0de),1);
    theta = zeros(length(psi0de),1);
    AOA = zeros(length(psi0de),1);

    for j = 1:length(psi0de)

% Calculate Phi
        Ut(j) = (r + mu*sin(psi0de(j) + pi));
        Up(j) = (lambda + r*B0de(j,2)+B0de(j,1)*mu*cos(psi0de(j) +
pi));
        phi(j) = (Up(j)./Ut(j));
        %phi = phi*(180/pi);
% Calculate AOA

        theta(j) = theta0 + thetalc*cos(psi0de(j) + pi) +
thetals*sin(psi0de(j) + pi);
        theta = theta*(180/pi);
        AOA(j) = theta(j) - phi(j);

    end
    U = [Up Ut];
% Plot Phi and AOA vs Psi

V = zeros(j,1);

```

```

L3 = zeros(j,1);

for mm = 1:j

    V(mm) = OMEGA*r + Vinf*sin(psi0de(mm) + pi);
    L3(mm) = 0.5*rho*V(mm)^2*c*Cla*AOA(mm)*(pi/180)*delta_r;
    %L(mm) = 0.5*((Ut(mm)^2)*(pi/180)*theta(mm) -
    ((Up(mm))).*(Ut(mm))));

end

%%
    plot(psi0de,L3)
    hold on

%% Blade 4

% Initial Conditions to get ODE started.
    B0 = [0,0];

% For loop iterates to re-insert initial conditions to smooth
out
% evaluation.

    for k = 1:20
        [psi0de, B0de] = ode45(@(psi0de, B0de)flap0de454(psi0de,
B0de,Vinf, theta0,thetalc,thetals, Ib, r, alphaS),[0, rev],
B0,opts);

        B0 = [B0de(end,1),B0de(end,2)];
    end
B0de = B0de*(180/pi);

% Preallocate for speed
    Ut = zeros(length(psi0de),1);
    Up = zeros(length(psi0de),1);
    phi = zeros(length(psi0de),1);
    theta = zeros(length(psi0de),1);

```

```

AOA = zeros(length(psi0de),1);

for j = 1:length(psi0de)

% Calculate Phi
    Ut(j) = (r + mu*sin(psi0de(j) + (3*pi/2)));
    Up(j) = (lambda + r*B0de(j,2)+B0de(j,1)*mu*cos(psi0de(j) +
(3*pi/2)));
    phi(j) = (Up(j)./Ut(j));
    %phi = phi*(180/pi);
% Calculate AOA

    theta(j) = theta0 + thetalc*cos(psi0de(j) + (3*pi/2)) +
thetals*sin(psi0de(j) + (3*pi/2));
    theta = theta*(180/pi);
    AOA(j) = theta(j) - phi(j);

end
    U = [Up Ut];
% Plot Phi and AOA vs Psi

V = zeros(j,1);
L4 = zeros(j,1);

for mm = 1:j

    V(mm) = OMEGA*r + Vinf*sin(psi0de(mm) + (3*pi/2));
    L4(mm) = 0.5*rho*V(mm)^2*c*Cla*AOA(mm)*(pi/180)*delta_r;
    %L(mm) = 0.5*((Ut(mm)^2)*(pi/180)*theta(mm) -
((Up(mm))).*(Ut(mm))));

end

%%
    plot(psi0de,L4)
    hold on

```

```

L = [L1,L2,L3,L4];

%Lift = zeros(3146,row);
for nn = 1:j
Lift(nn,n) = sum(L(nn,:));
end
%plot(psi0de, Lift)
hold on
%legend('Blade 1','Blade 2','Blade 3','Blade 4','Total Lift')

L5 = flip(L1);
L6 = flip(L2);
L7 = flip(L3);
L8 = flip(L4);

LL = [L5,L6,L7,L8];
Lift2 = zeros(j,1);
for nn = 1:j
Lift2(nn) = sum(LL(nn,:));
end
Lift1and2 = Lift+Lift2;

    plot(psi0de,L5)
    hold on
    plot(psi0de,L6)
    hold on
    plot(psi0de,L7)
    hold on
    plot(psi0de,L8)
    hold on
    %plot(psi0de, Lift2)
    hold on
    plot(psi0de, Lift1and2)

end

Lift_Total_psi = zeros(j,1);

```

```

for nnn = 1:j
    Lift_Total_psi(nnn) = sum(Lift1and2(nnn,:));
end
plot(psi0de,Lift_Total_psi)
xticks([0 pi 2*pi])
xticklabels({'0', '\pi', '2\pi'})
xlabel('Psi')
ylabel('Lift (N)')
title('Total Lift About Rotation')
grid on

%% Functions
function dum = flap0de451(psi, B, Vinf, theta0,theta1c,theta1s,
Ib, r, alphaS)

    alphaS = alphaS*(pi/180);
    c = 0.5273;
    Cla = 0.1*(180/pi);
    rho = 1.225;
    R = 8.18;
    OMEGA = 27;
    mu = (Vinf*cos(alphaS))/(OMEGA*R);
    gamma = (rho*Cla*c*R^4)/Ib;
    lambda = (Vinf*sin(alphaS) + gamma)/(OMEGA*R);
    e = 0.10;
    nu = (r-e)/(1-e);
    v = 1.15;

    Ut = (r + mu*sin(psi));
    Up = (lambda + r*B(2)+B(1)*mu*cos(psi));

    theta = theta0 + theta1c*cos(psi) + theta1s*sin(psi);

    L = 0.5*((Ut^2)*theta - ((Up)).*(Ut));

    Mf = gamma*L*nu;

    Bddot = -(B(1))*v^2 + Mf;

    dum = [B(2), Bddot];

```

```

    dum = dum(:);
end
function dum = flap0de452(psi, B, Vinf, theta0,thetalc,thetals,
Ib, r, alphaS)

    alphaS = alphaS*(pi/180);
    c = 0.5273;
    Cla = 0.1*(180/pi);
    rho = 1.225;
    R = 8.18;
    OMEGA = 27;
    mu = (Vinf*cos(alphaS))/(OMEGA*R);
    gamma = (rho*Cla*c*R^4)/Ib;
    lambda = (Vinf*sin(alphaS) + gamma)/(OMEGA*R);
    e = 0.10;
    nu = (r-e)/(1-e);
    v = 1.15;

    Ut = (r + mu*sin(psi + pi/2));
    Up = (lambda + r*B(2)+B(1)*mu*cos(psi + pi/2));

    theta = theta0 + thetalc*cos(psi + pi/2) + thetals*sin(psi
+ pi/2);

    L = 0.5*((Ut^2)*theta - ((Up)).*(Ut));

    Mf = gamma*L*nu;

    Bddot = -(B(1))*v^2 + Mf;

    dum = [B(2), Bddot];

    dum = dum(:);
end
function dum = flap0de453(psi, B, Vinf, theta0,thetalc,thetals,
Ib, r, alphaS)

    alphaS = alphaS*(pi/180);
    c = 0.5273;
    Cla = 0.1*(180/pi);

```

```

rho = 1.225;
R = 8.18;
OMEGA = 27;
mu = (Vinf*cos(alphaS))/(OMEGA*R);
gamma = (rho*Cla*c*R^4)/Ib;
lambda = (Vinf*sin(alphaS) + gamma)/(OMEGA*R);
e = 0.10;
nu = (r-e)/(1-e);
v = 1.15;

Ut = (r + mu*sin(psi + pi));
Up = (lambda + r*B(2)+B(1)*mu*cos(psi + pi));

theta = theta0 + thetalc*cos(psi + pi) + thetals*sin(psi +
pi);

L = 0.5*((Ut^2)*theta - ((Up)).*(Ut));

Mf = gamma*L*nu;

Bddot = -(B(1))*v^2 + Mf;

dum = [B(2), Bddot];

dum = dum(:);
end
function dum = flap0de454(psi, B, Vinf, theta0,thetalc,thetals,
Ib, r, alphaS)

alphaS = alphaS*(pi/180);
c = 0.5273;
Cla = 0.1*(180/pi);
rho = 1.225;
R = 8.18;
OMEGA = 27;
mu = (Vinf*cos(alphaS))/(OMEGA*R);
gamma = (rho*Cla*c*R^4)/Ib;
lambda = (Vinf*sin(alphaS) + gamma)/(OMEGA*R);
e = 0.10;
nu = (r-e)/(1-e);
v = 1.15;

```

```

    Ut = (r + mu*sin(psi + 3*pi/2));
    Up = (lambda + r*B(2)+B(1)*mu*cos(psi + 3*pi/2));

    theta = theta0 + theta1c*cos(psi + 3*pi/2) +
theta1s*sin(psi + 3*pi/2);

    L = 0.5*((Ut^2)*theta - ((Up)).*(Ut));

    Mf = gamma*L*nu;

    Bddot = -(B(1))*v^2 + Mf;

    dum = [B(2), Bddot];

    dum = dum(:);
end

```